

Recent Advances in Fluorescent Theranostics for Alzheimer's Disease: A Comprehensive Survey on Design, Synthesis, and Properties

Telmo N. Francisco, Daniela Malafaia, Lúcia Melo, Artur M. S. Silva, and Hélio M. T. Albuquerque*



Cite This: *ACS Omega* 2024, 9, 13556–13591



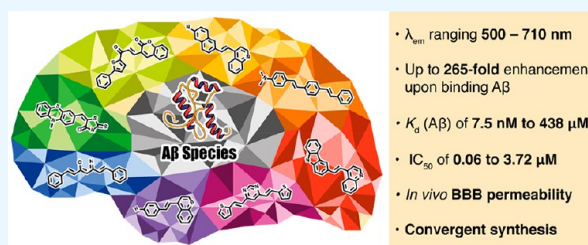
Read Online

ACCESS |

Metrics & More

Article Recommendations

ABSTRACT: Alzheimer's disease (AD) is the most common form of neurodegenerative dementia that is rapidly becoming a major health problem, especially in developed countries because of their increasing life expectancy. Two main problems are often associated with the disease: (i) the absence of a widely accessible “gold-standard” for early diagnosis and (ii) lack of effective therapies with disease-modifying effects. The recent success of the monoclonal antibody lecanemab played an important role not only in clarifying a possible druggable pathway but also in spelling the revival of small molecule drug discovery. Unlike bulky biologics, small molecules are structurally less complex, generally cheaper, and compatible with at-home oral consumption, making it feasible for people to start their drug regimen early and stay on it longer. In this sense, small-molecule near-infrared fluorescent theranostics have been gaining more and more attention from the scientific community, as they have the potential to simultaneously provide diagnostic outputs and deliver therapeutic action, paving the way toward personalized medicine in AD patients. They also have the potential to shift the diagnostic “status-quo” from expensive and limited-access PET radiotracers toward inexpensive and handy imaging tools widely available for primary patient screening and preclinical animal studies. Herein, we review the most recent advances in the field of fluorescent theranostics for Alzheimer's disease, detailing their design strategies, synthetic approaches and imaging and therapeutic properties *in vitro* and *in vivo*. With this Review, we intend to provide a milestone in the acquired knowledge in the field of AD theranostics, encouraging the future development of properly designed theranostic compounds with improved chances to reach clinical applications.



INTRODUCTION

Neurological disorders are a heterogeneous group of diseases characterized by the progressive degeneration of the structure and function of the central nervous system and the peripheral nervous system.¹ Alzheimer's disease (AD) is one of the most common neurological disorders, being clinically classified as a syndrome of progressive dementia where patients may also find signs absent and inconspicuous.² This disease mainly affects populations at older ages, and it tends to be more prevalent among women.^{3,4} Positive family history, a head trauma with a concussion, birth order, and mother's age at birth have shown to be potentially pathogenic causes for the appearance of AD. Memory loss of recent events is one of the first symptoms to manifest in AD patients, and eventually it will slowly progress to dementia, with impairment spreading to language and visuospatial deficits. Other symptoms that may appear in these patients are disorientation, poor judgment, poor concentration, aphasia, and apraxia.⁵ The patients tend to become rigid, mute, incontinent, and bedridden as the disease reaches its final stage. Due to all these symptoms, they may need help for simple tasks, such as eating, dressing, or carrying out toilet functions, which

can lead to death by malnutrition, secondary infectious, pulmonary emboli, or heart disease.⁶ AD is a foremost public health issue affecting nearly 50 million people worldwide, and that number is projected to increase to 150 million by 2050.⁷ For the developed countries, this is particularly troubling due to the continuously aging population, which will ultimately increase the economic and healthcare burden to deal with.^{1,5} On the other hand, low-income and middle-income countries (LMICs), which are overstretched and have under-resourced public health systems, low staff morale, poor training, and limited expertise in mental health, result in poor care for older people; in particular, those with dementia are the most affected as they lack of access to the correct treatment for AD.⁸ These challenges are

Received: December 27, 2023

Revised: February 6, 2024

Accepted: February 13, 2024

Published: March 11, 2024



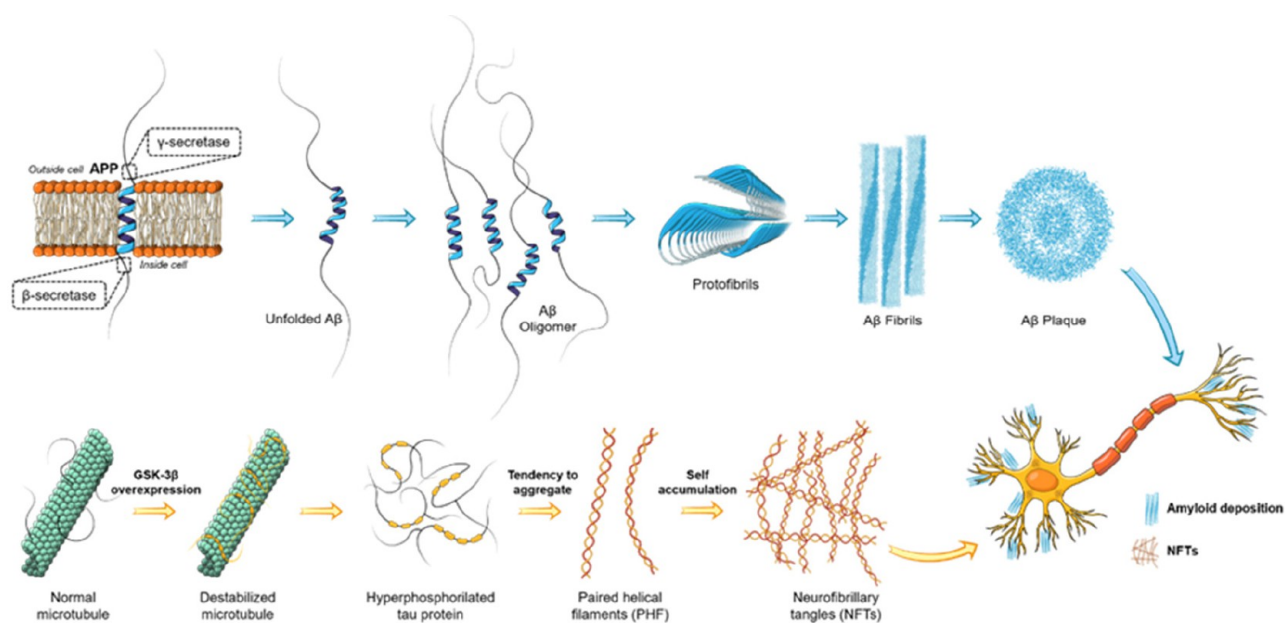


Figure 1. Schematic depiction of $A\beta$ and tau cascades associated with AD.

exacerbated by the lack of effective treatments and by the fact that there is no widely available gold standard for diagnosis.

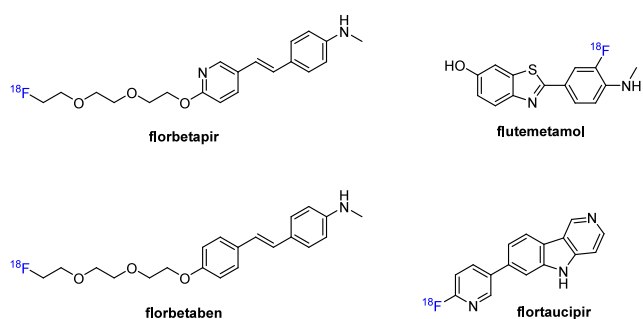


Figure 2. Chemical structures of PET tracers approved for AD diagnosis.

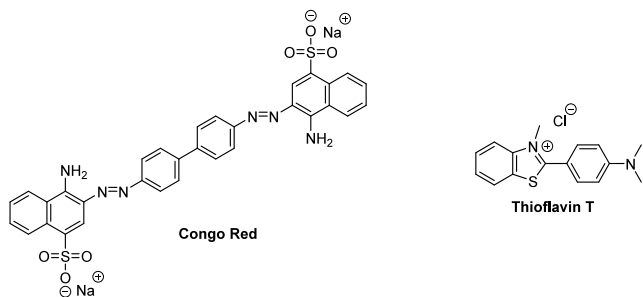
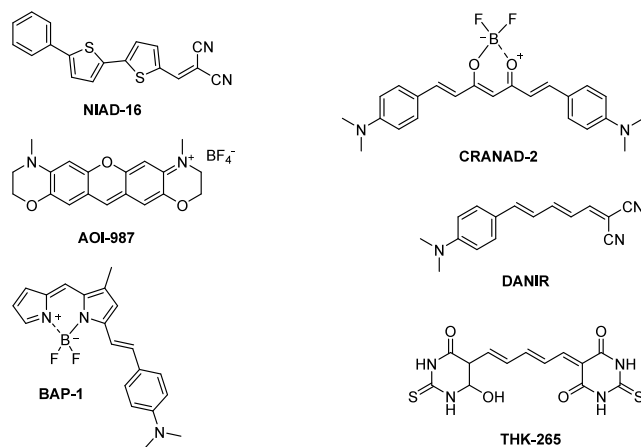


Figure 3. Structures of Congo Red and thioflavin T as histological dyes of amyloid fibrils.

Despite the multifactorial nature of the pathological mechanisms of AD, both β -amyloidopathy and tauopathies are considered the major contributing hallmarks for this neurodegenerative disease. The mainstream concept underlying AD research, and yet rather disputed over the years, is clearly the self-aggregation of amyloid- β ($A\beta$) peptides, mainly composed of $A\beta_{1-40}$ and $A\beta_{1-42}$, by the formation of soluble misfolded $A\beta$ forms (dimers and oligomers, the main neurotoxic species),

$A\beta$ -targeting NIRF probes



Tau-targeting NIRF probes

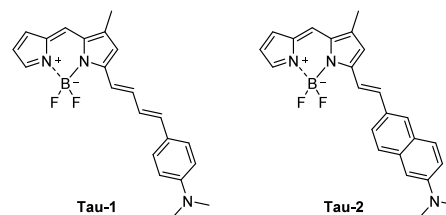


Figure 4. Examples of NIRF probes capable of labelling $A\beta$ plaques and NFTs.

which ultimately evolve into insoluble fibrils with β -sheet-rich structures (senile plaques) (Figure 1).^{9,10} Beyond $A\beta$ aggregation, the abnormal self-aggregation of tau proteins into paired helical filaments, *i.e.*, neurofibrillary tangles (NFTs), is also described as the major tauopathy associated with AD (Figure 1).^{9,10} In fact, back in 2018, the Alzheimer's Association and the National Institute on Aging classified as AD biomarkers the $A\beta$ deposits, tau pathology, and corresponding neuro-

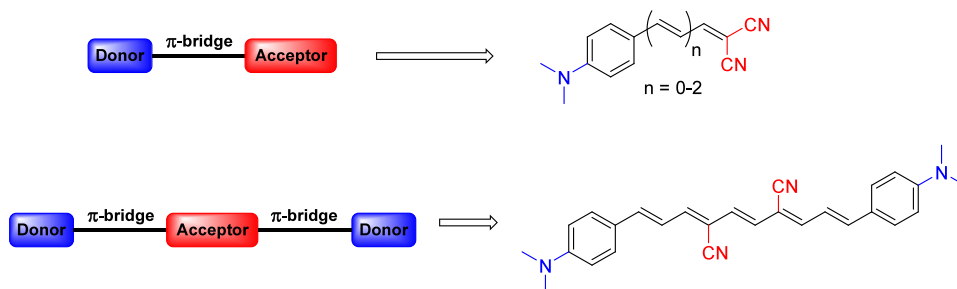


Figure 5. Depiction of common D- π -A and D- π -A- π -D architectures and representative examples.

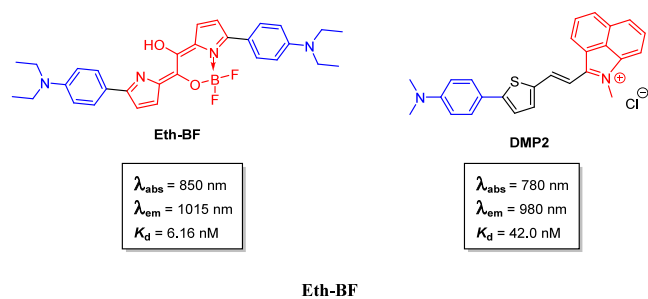


Figure 6. Chemical structures of NIR-II amyloid- β probes Eth-BF⁴² and DMP2.

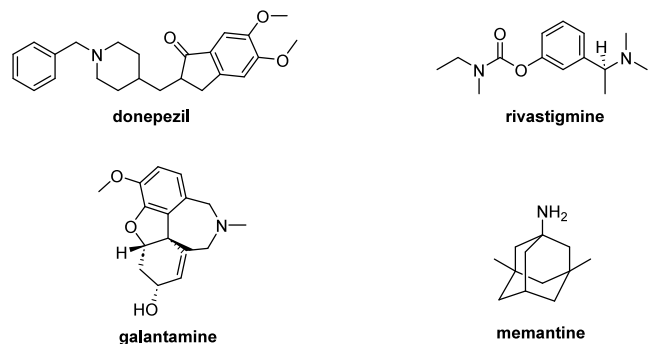


Figure 7. Currently available drugs for the treatment of AD, approved by the FDA and EMA.



Figure 8. Schematic depiction of the "theranostic" concept.

degeneration.¹¹ Therefore, the research on reliable and accurate dual imaging strategies regarding A β and tau protein aggregation processes can provide more insights and a new strategy to diagnose and monitor AD.^{11,12}

More recently, the monoclonal antibody lecanemab slowed cognitive decline in people with early stage AD and was the first

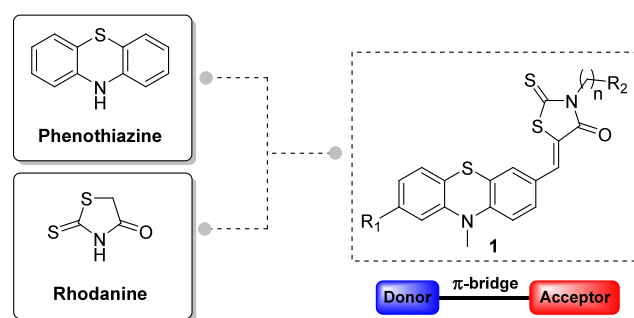


Figure 9. Donor-acceptor design by framework combination of phenothiazine and rhodanine.

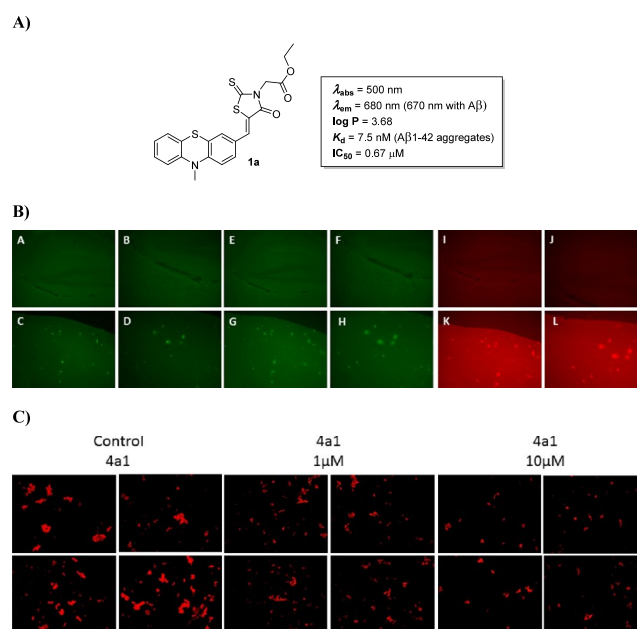
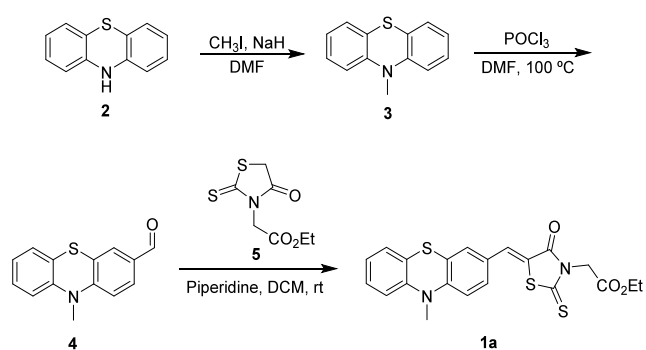


Figure 10. (A) *In vitro* binding profile of compound **1a** (4a1 in the original article). (B) *In vitro* fluorescent staining assays for A β plaques—fluorescent staining of compound **1a** on cortical brain slice sections from a double Tg mouse. (C) Inhibition of A β ₁₋₄₂ self-aggregation followed by fluorescence microscopy using compound **1a**. Reprinted in part with permission from ref 62. Copyright 2017 American Chemical Society.

treatment for this disease to unequivocally pass its clinical trials.¹³ Of course, it is possible to argue its effects because of the modest cognitive improvements in patients. However, on the other hand, these modest results helped to clarify a possible druggable pathway based on the amyloid hypothesis. Moreover, it is reasonable to say that lecanemab played a crucial role in the

Scheme 1. Synthesis of Phenothiazine-rhodanine Derivative 1a



validation of one of the hallmarks of the disease, encouraging further research to improve the results in clinical trials of anti-amyloid treatments.

THE DIAGNOSTIC STATUS QUO OF AD

Currently, AD is clinically diagnosed on the basis of mental and cognitive examinations (decline in memory, cognition, and function over time), while its pathological confirmation is obtained through post-mortem histopathological examination of brain tissue for $A\beta$ plaques and tau fibrils or through a biopsy, which is an invasive procedure with evident risk to the patient. However, the disease pathology has already caused serious brain damage in individuals diagnosed in this way, as neurodegeneration is estimated to start 20–30 years before the first clinical symptoms become apparent.⁹

In recent years, several imaging techniques have been developed to monitor and diagnose $A\beta$ plaques and tau fibrils, which are hypothesized as the major contributing factors in the diagnosis of AD. Positron emission tomography (PET), magnetic resonance imaging (MRI), and single-photon emission computed tomography (SPECT) have been used to detect $A\beta$ plaques and tau fibrils both *in vitro* and *in vivo* in the assessment of AD and also in clinical trials.^{14–16} PET ¹⁸F-labeled ligands such as florbetapir, florbetaben, flutemetamol, and more recently flortaucipir (Figure 2) are currently approved by the Food and Drug Administration (FDA) for clinical diagnosis of AD patients, contributing to the spread of this imaging technique in many countries for clinical practice.^{17–19} Nevertheless, these PET tracers specifically label insoluble $A\beta$ species and tau fibrils rather than the soluble ones that are believed to be more toxic.¹⁸

Despite PET being one of the most popular imaging techniques for clinical applications, its regular use in AD diagnosis is quite unfeasible due to its financial and technical complications. PET applications are further restricted by the short half-lives of commonly used emitting isotopes (20 min in the case of ¹⁴C and 110 min for ¹⁸F), which require the on-site synthesis of PET tracers and access to radiochemistry equip-

Scheme 2. Synthesis of the Intermediate Rhodanine Derivative 5

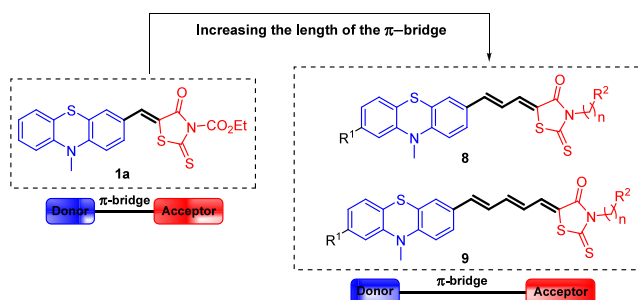
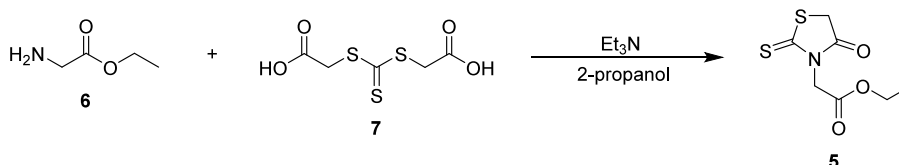
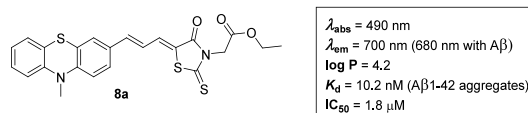
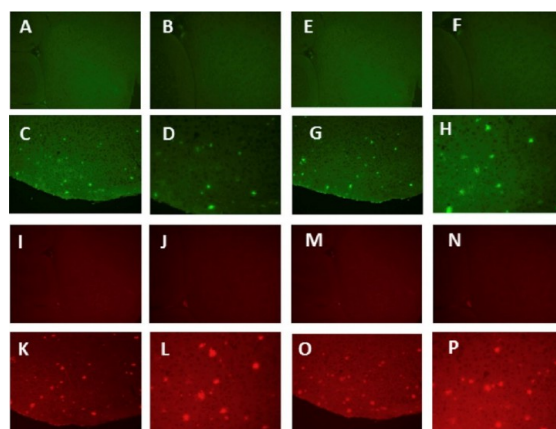


Figure 11. Design strategy of the second-generation of phenothiazine-rhodanine theranostics 8 and 9.

A)



B)



C)

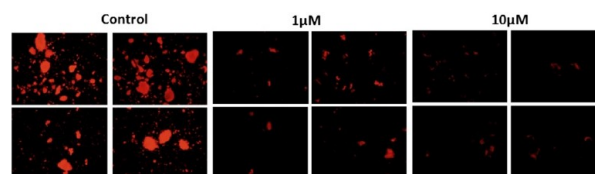


Figure 12. (A) *In vitro* binding profile of compound 8a (Sa1 in the original article). (B) Fluorescence staining with 8a on brain slices in the cerebral cortex from a double Tg mouse using ThT and $A\beta$ antibody ab2454. (C) Inhibition of self-aggregation of $A\beta_{1-42}$ by 8a using fluorescence microscopy. Reprinted in part with permission from 72. Copyright 2017 Elsevier.

ment and a cyclotron.¹⁷ Even though several PET tracers have been used to evaluate the efficacy of experimental AD drugs in clinical trials, they are not often used to monitor drug treatment

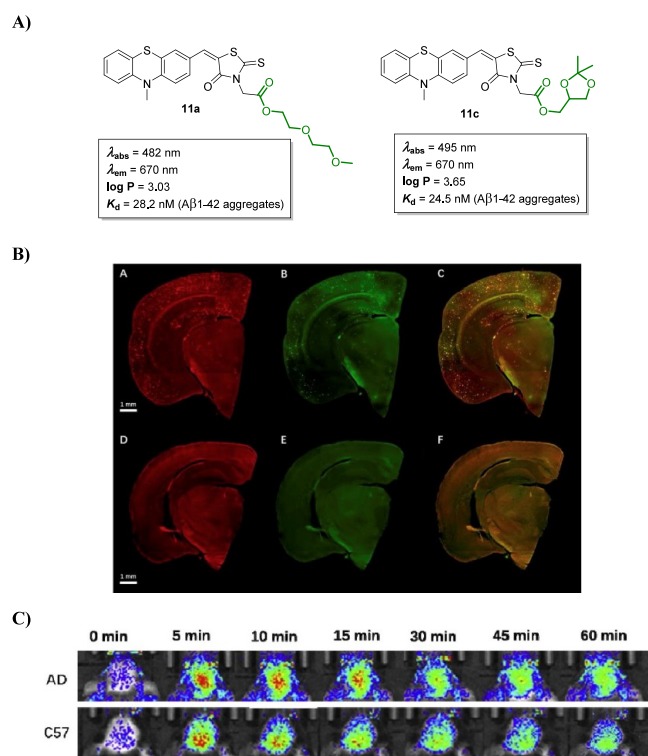


Figure 14. (A) *In vitro* binding profiles of compound **11a** (4 in the original article) and **11c** (PHTZ-1 in the original article). (B) *Ex vivo* histology staining of brain slices from a Tg mouse and wild-type control mouse after injection of probe **11a**. (C) Fluorescence images of the same Tg (top row) and WT (bottom row) mouse head at selected time points before or after intravenous injection of compound **11c**. Reprinted in part with permission from refs 73 and 74. Copyright 2019 Elsevier.

biological matter, and minimal photodamage to biological samples.²⁸

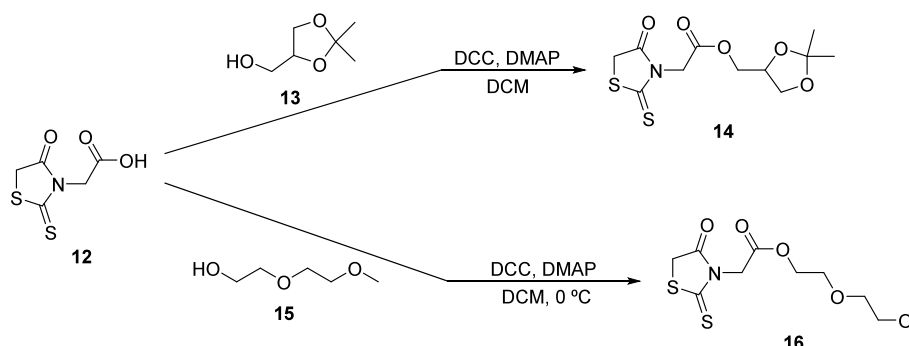
Currently, most of the existing NIRF probes share common design approaches, *i.e.*, based on the donor- π -acceptor (D- π -A) or donor- π -acceptor- π -donor (D- π -A- π -D) architectures, possessing an electron-rich donor (such as NH₂, NR₂, or OR) and an electron-withdrawing group (such as NO₂ or CN) bridged by a conjugated π -system (with various lengths and structures) (Figure 5) (for recent reviews see, refs 35 and 36).^{26,28,34–36} This type of structural design displays an excellent rigid planarity and capability of electronic transmission, pushing the emission wavelength into the NIR region.³⁷

Unfortunately, the existing NIRF probes still have a long way to go to be applied in human AD patients, since A β plaques and tau proteins are buried inside the skull-shielded brain. In fact, fluorescence signal scattering in the biological environment is perhaps the major drawback of the existing NIRF probes, limiting the quantification of the amyloid load to the surface area of the brain. However, despite the obstacles faced by the current NIRF probes, some interesting strategies can be used to bypass these intrinsic difficulties, such as the use of neural tissues that are not shielded by the skull as brain surrogates. For instance, the retina (often called as “the window to the brain”),³⁸ which is easily accessible for direct and noninvasive imaging, represents an alternative path for NIRF imaging in AD animal models and patients.³⁹

Within the fluorescence imaging techniques, the NIR-II window (1000–1700 nm) has been drawing some attention due to its deeper penetration depth, high signal-to-noise imaging, and fast response.⁴⁰ In particular, the all-organic small molecules are the object of much research as a result of their intrinsic properties such as low toxicity, fast excretion rate, good biocompatibility, versatile structures, deep tissue penetration, high imaging resolution, and low autofluorescence.⁴¹ Some examples of NIR-II staining compounds such as aza-borondipyromethenes (aza-BODIPYs), phthalocyanine derivatives, and D-A-D architecture bioprobes with benzobisthiadiazole conjugated with fluorene or triphenylamine as backbones have been reported for tumor imaging.^{42–45} Regrettably, the NIR-II probes are still quite underdeveloped for applications in AD diagnosis. To the best of our knowledge, the very first NIR-II A β -oligomer-targeting probe was just reported in 2022 by Pan and co-workers, the so-called **Eth-BF** (Figure 6).⁴⁶ Right after, a second NIR-II probe, **DMP2** (Figure 6), was reported by Miao and colleagues, demonstrating selectivity for detection of A β -plaques *in vivo* and working via a suppressed twisted intramolecular charge transfer (TICT) effect.⁴⁷

Eth-BF is built upon a D-A-D structure, in which a boron nitride-bridged azafulvene is used as a strong electron-absorbing group and *N,N*-diethylaniline acts as the recognition group, resulting in a strong push-pull arrangement leading to an emission wavelength of 1015 nm. Furthermore, **Eth-BF** demonstrated strong binding affinity for A β Os (K_d = 6.16 nM) due to the formation of hydrogen bonding interactions between **Eth-BF** and Phe20 residues of A β Os.⁴⁶ On the other hand, **DMP2** was built on a D-A architecture, where the *N,N*-dimethylaminophenyl moiety serves as electron donor group as well as an A β -binding unit. A thiophene-double bond bridge was selected as the π -conjugation bridge, providing suitable lipophilicity for BBB penetrability as well, while a benzo[*cd*]-

Scheme 4. Synthesis of Rhodanine Precursors 14 and 16 through Steglich Esterification



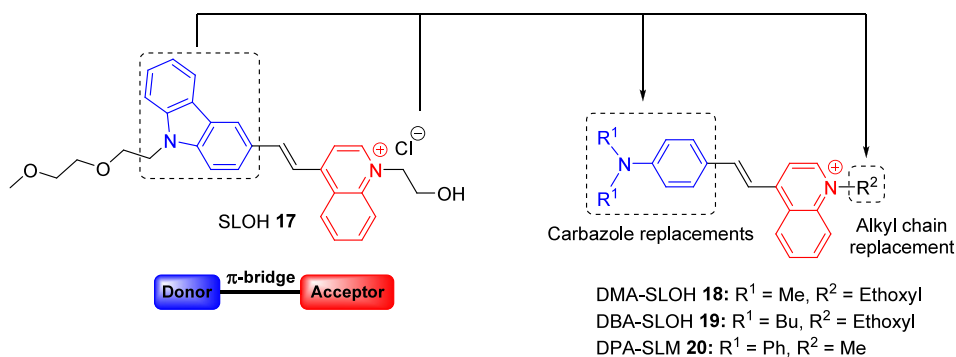


Figure 15. Design strategy for new SLOH analogues through carbazole and alkyl chain replacements.

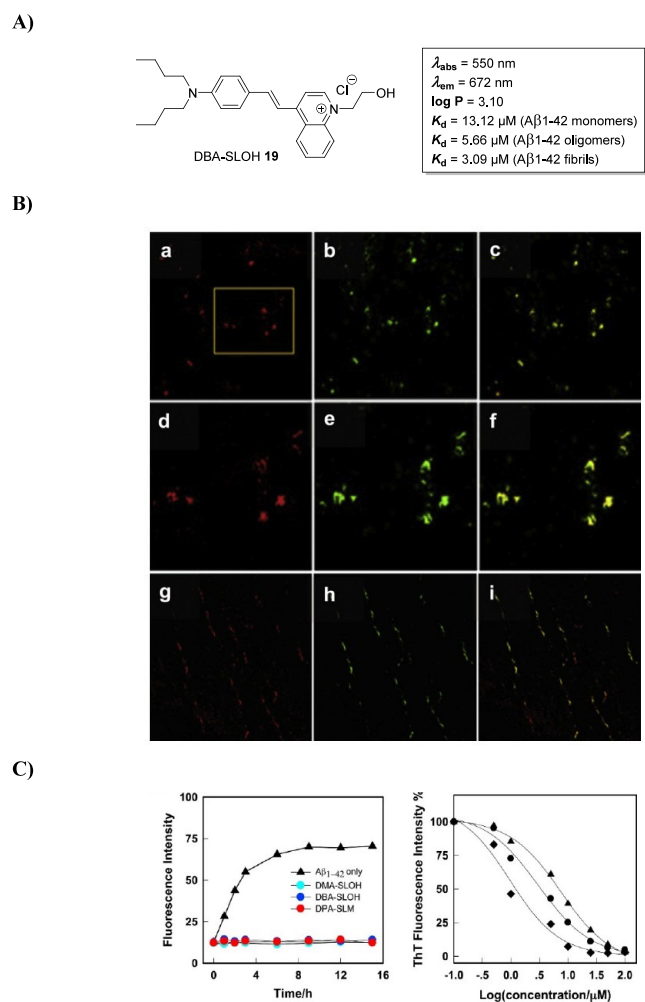


Figure 16. (A) *In vitro* binding profile of DBA-SLOH 19. (B) Histological staining of the brain slices of APP/PS1 transgenic AD mice with DBA-SLOH 19 via tail vein injection, ThT, and anti-amyloid oligomer antibody labeled with FITC. (C) The ThT-monitored inhibitory effects of DMA-SLOH 18, DBA-SLOH 19, and DPA-SLM 20 upon incubation with $A\beta_{1-42}$. Reprinted in part with permission from ref 77. Copyright 2016 Elsevier.

indol-1-ium group was chosen as the electron acceptor (Figure 6). In this case, both the absorption and emission wavelengths were 780 and 980 nm, respectively, demonstrating selectivity for $A\beta$ -plaques with $K_d = 42.0 \text{ nM}$.⁴⁷

Another interesting technique with great potential for imaging the AD biomarkers is widefield fluorescence microscopy. This

strategy can be described as a technique where the whole target is illuminated with light with a controlled wavelength, exciting the fluorescence molecules within the spotlighted area and allowing the production of images with low temporal resolution. In fact, in the last years this has been studied as a technique for monitoring activity in the mouse neocortex, implying the potential study of the human brain as well.⁴⁸ However, widefield fluorescence microscopy is cut short due to its low skull penetration, limited to depths of 1–2 mm, which forces the use of techniques such as craniotomy, cranial windows, and skull-thinning in order to obtain the desired images. In a recent work, studies led to the improvement of an epifluorescence imaging mode that allowed for penetration through the mouse skull and tissue to a depth of over 2 mm when using fluorescence between 1.3 and 1.4 μm wavelength.⁴⁸ With this improvement, through a noninvasive technique it was possible to study and follow biological processes in the brain at a molecular scale, displaying the potential of the usage of widefield fluorescence microscopy.⁴⁹

AVAILABLE THERAPEUTIC APPROACHES FOR AD

Nowadays, there are four small-molecule drugs approved by FDA and EMA for the treatment of Alzheimer's disease (Figure 7). These drugs are divided into the reversible acetylcholinesterase inhibitors (AChEIs), represented by donepezil, rivastigmine, and galantamine, and the antagonist of the *N*-methyl-D-aspartic acid (NMDA) receptor, memantine (Figure 7).⁵⁰ The mechanism of action of AChEI drugs is based on the inhibition of AChE in the synaptic cleft, which increases both cholinergic transmission and, consequently, the cognitive capacity of AD patients.⁵¹ On the other hand, memantine reduces the excitotoxicity as a result of the high concentration of glutamate in the synaptic cleft by blocking the NMDA receptor.⁵¹ However, it has been shown that these drugs only provide limited symptomatic relief and are not capable of stopping the disease progression, leading to neuron damage and ultimately to the patients' death.

Over the years, researchers continued to explore new therapeutic strategies to slow down the course of the disease, and several anti-AD agents have been developed so far, even though AD drug development has shown only a 0.4% success rate. Since 2003, a few drugs have been approved, including GV-971 only approved in China in 2019.⁵² In 2021, a landmark in AD drug discovery was achieved with Aduhelm (aducanumab), which was granted Fast Track designation by FDA through its accelerated approval pathway. Aducanumab is an $A\beta$ -directed monoclonal antibody that targets the $A\beta$ aggregates found in patients with AD.^{53,54} The phase III clinical trials showed that

Scheme 5. Two-Step Synthetic Approach for DBA-SLOH 19

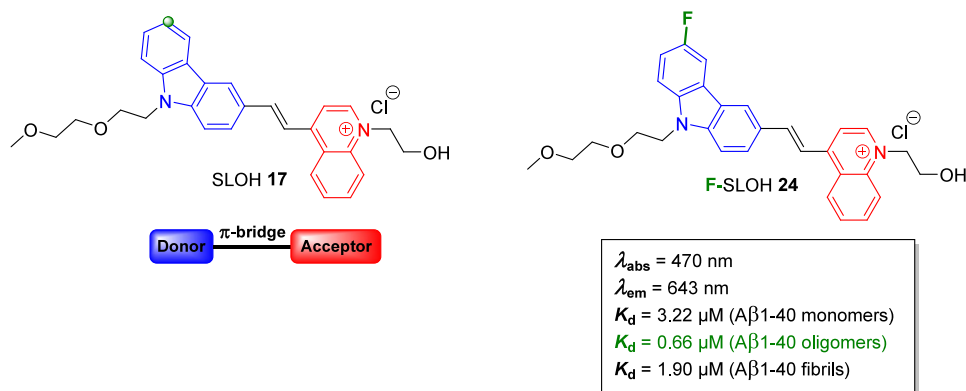
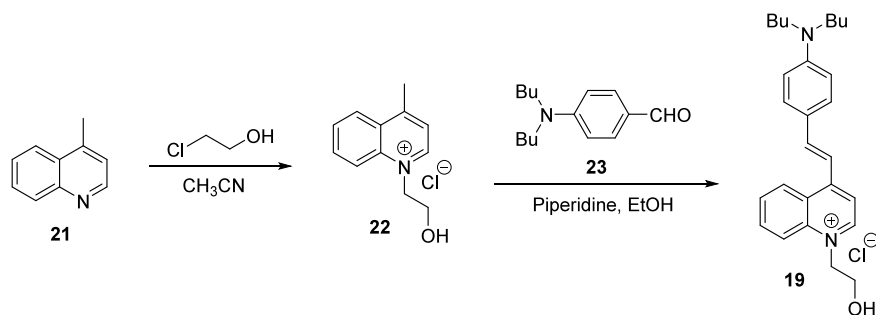


Figure 17. F-SLOH 24 obtained by installing fluorine in the carbazole moiety.

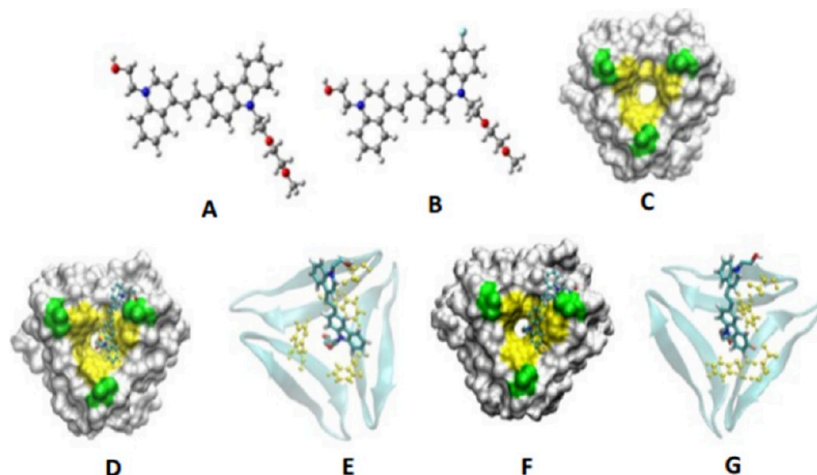


Figure 18. Complexes of (A) SLOH 17 and (B) F-SLOH 24 with (C) $A\beta$ oligomers. Residues F19 and V36 are indicated in yellow and green, respectively. Models simulating the complexes of (D and E) SLOH 17 and (F and G) F-SLOH 24 with $A\beta$ oligomers are displayed. Reprinted in part with permission from ref 79. Copyright 2017 Royal Society of Chemistry.

this drug reduced the $A\beta$ pathology, but its efficacy in promoting cognitive improvement remained ambiguous, as the same trials showed no correlation between the $A\beta$ -PET signal and the clinical outcomes in patients receiving Aduhelm.^{53,54} In fact, this monoclonal antibody was not approved by EMA due to its side effects, including brain swelling and bleeding.^{53,55} Later this year, a similar monoclonal antibody, lecanemab,¹³ was approved also by the fast-tracked approval of FDA, and another one, donanemab, which is in phase III clinical trials, is believed to decrease disease progression in 35%.⁵⁶ Despite some of the good results obtained from these antibodies, many experts believe that the number of people that will be able to get the drugs will be extremely limited, particularly countries with under-resourced

public health systems, due to the high administration cost (an estimated value of up to \$26,500 per year).

THE "THERANOSTIC" APPROACH IN AD

The term "theranostic" is usually employed to categorize a single chemical entity with the ability to deliver therapeutic effects while having an additional diagnostic functionality simultaneously.⁵⁷ The origin of the term dates back to 1998 when it was first devised by John Funkhouser to define a given material comprising diagnosis, treatment, and follow-up of a given disease.⁵⁸ Actually, in most typical approaches, imaging probes (diagnostic) and drugs (therapy) are chased and developed

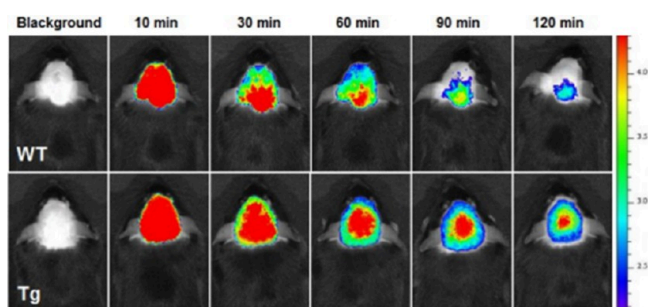


Figure 19. *In vivo* fluorescent assessment of 7-month-old Tg mice and age-matched WT mice. Images were taken at various time points both prior to and following the intravenous injection administration of F-SLOH 24. Reprinted in part with permission from ref 79. Copyright 2017 Royal Society of Chemistry.

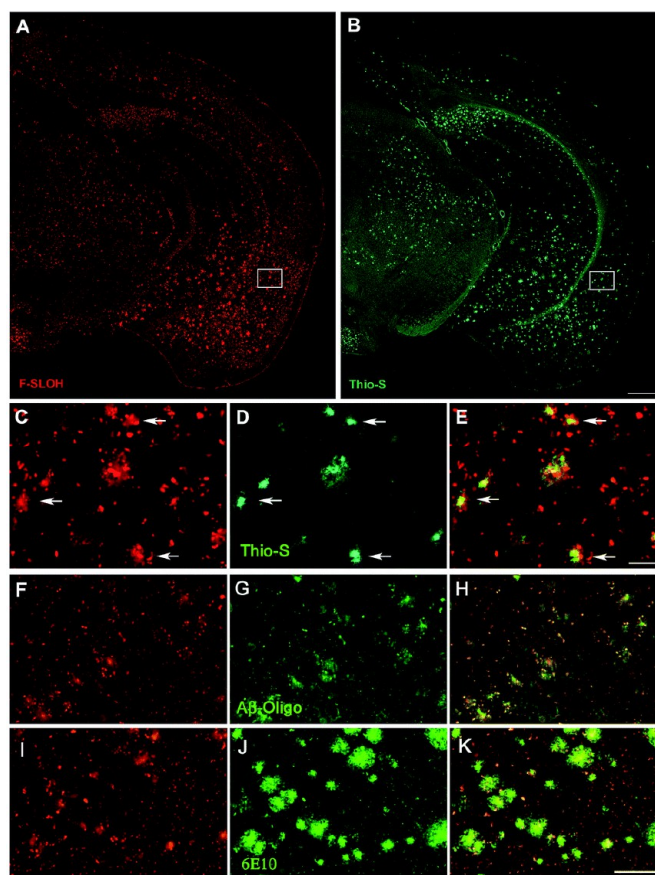
separately, which is time-consuming and expensive, having a great impact in the total amount of R&D assets of pharmaceutical companies. With the evolution of medicine throughout the years, modern-day therapies are becoming increasingly more personalized and directed at specific molecular pathways, customizing treatments to the “molecular profile” of individual patients. Cancer research and therapy are quite a case-study in the application of theranostics, and although only a few drugs are currently on the market, many

more are in clinical trials, with extremely promising early results.⁵⁹ In the case of AD, the theranostic concept is far from the degree of development observed in cancer. Nevertheless, theranostic approaches targeting neurodegenerative disorders are being increasingly investigated.

In this respect, special emphasis should be given to the NIRF theranostics (Figure 8). These compounds must have the ability to change fluorescence properties upon binding to AD biomarkers, the capacity to absorb and emit light in the far red/near-infrared region (ca. 600–800 nm), and also ability to modulate aggregation processes. Ideally, and as reported for fluorescent probes, the NIR-II window should be pursued also for theranostic compounds, as their tissue penetration is more suitable for the central nervous system (CNS). As far as we know, there are no examples of NIR-II theranostics so far.

In recent years, an ever-increasing number of theranostic compounds have been reported, mostly targeting A β species (for a recent review, see ref 61).^{60,61} However, these molecules are not always designed to have both functionalities, *i.e.*, the therapeutic and the imaging scores. Most of the time, they are based on A β NIRF imaging probes, which also have the additional ability to modulate the aggregation process of A β peptides. A seminal publication by Bolognesi et al. was the first critical review on the field of NIRF theranostics developed for AD, dating back to 2016.⁶⁰ In this review, Bolognesi et al. discuss the sort of a paradigm shift in AD research by integrating

A)



B)

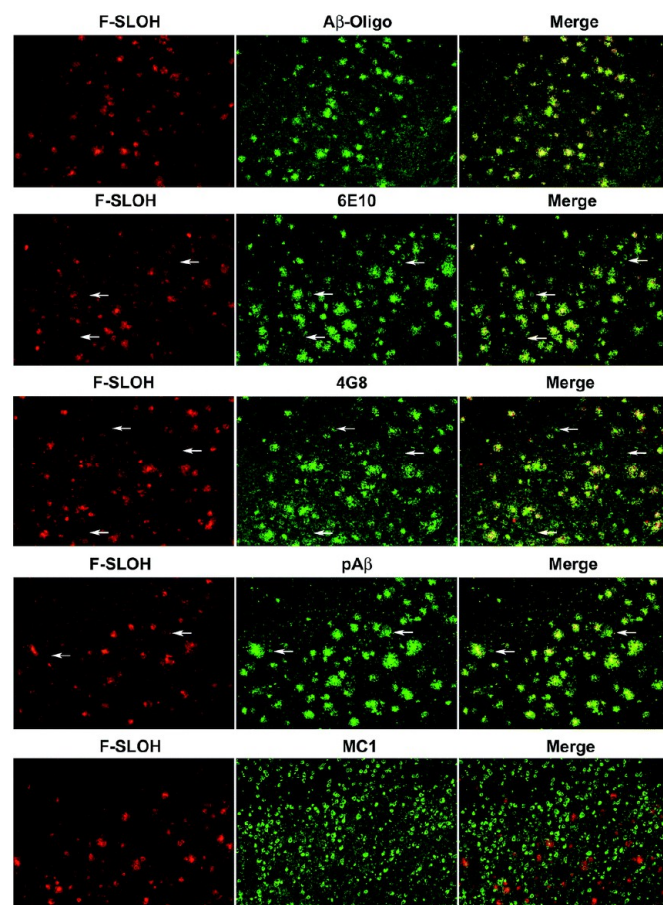


Figure 20. Co-localization studies with SLOH 17 and F-SLOH 24 with (A) ThS and (B) antibodies. Reprinted in part with permission from ref 79. Copyright 2017 Royal Society of Chemistry.

Scheme 6. Convergent Synthetic Approach to Prepare F-SLOH 24

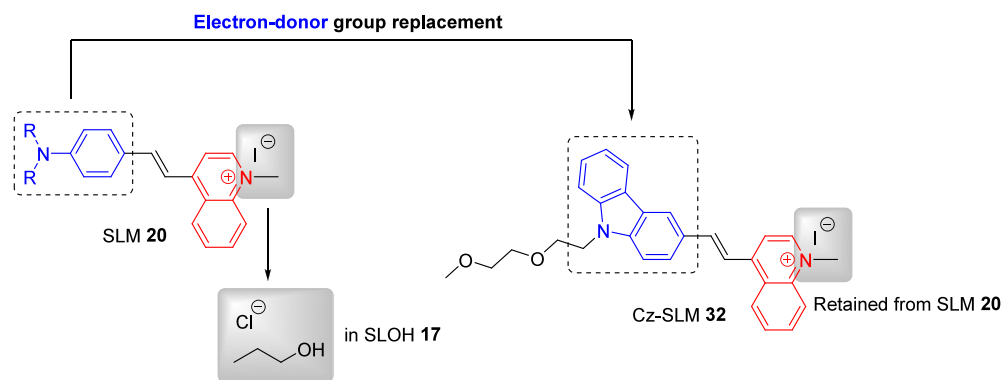
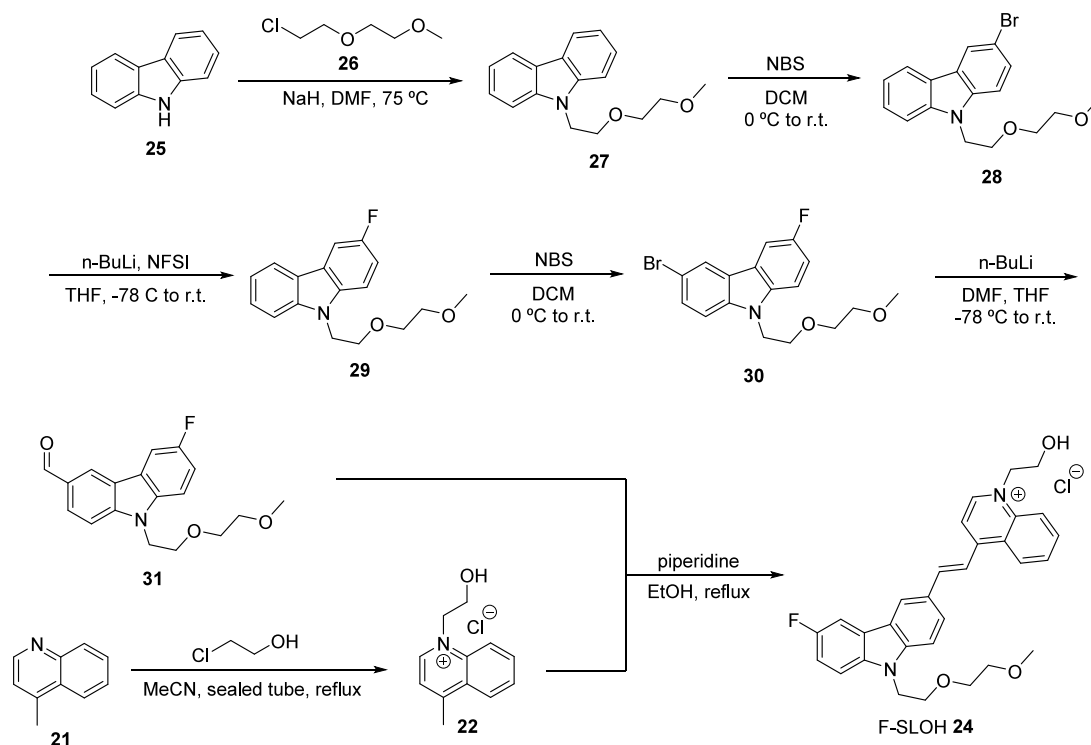


Figure 21. Structural design strategy of Cz-SLM 32.

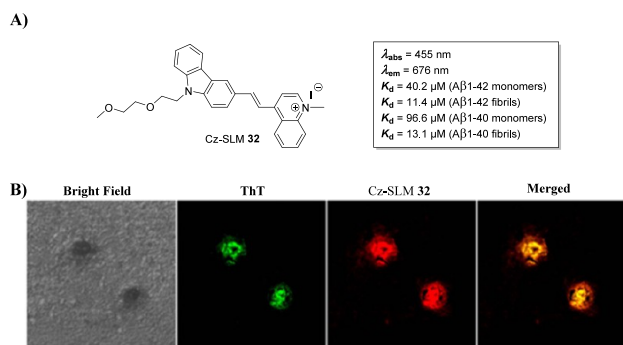


Figure 22. (A) *In vitro* binding profile of Cz-SLM 32. (B) Histological assessment performed on brain slices from 9-month-old Tg mice. The staining was carried out using Cz-SLM 32 administered via tail-vein injection, and costained with ThT. Reprinted in part with permission from ref 82. Copyright 2018 American Chemical Society.

therapeutics and diagnostics, passing through the concepts of companion diagnosis in their way to the theranostics.⁶⁰

Having the publication by Bolognesi et al. as the starting point, the present Review covers the most recent advances made in the field of theranostic compounds targeting AD biomarkers. Critical insights concerning the design strategies of each reported compound will be furnished and argued from a synthetic chemistry point-of-view, also referring to their structural, optical and binding properties. A survey of the most common chemical strategies and reactions employed in this field will be discussed in the next sections of this Review.

■ AMYLOID- β TARGETING THERANOSTICS

Phenothiazine-Based Compounds. One year after the Bolognesi et al. review on fluorescent theranostics, Chen and co-workers reported the development of the first phenothiazine-based theranostic targeting $A\beta$ aggregation.⁶² The authors followed a the classical D-A architecture bridged by conjugation of π -electron chains to design the compounds. The phenothia-

Scheme 7. Convergent Synthetic Approach to Prepare Cz-SLM 32

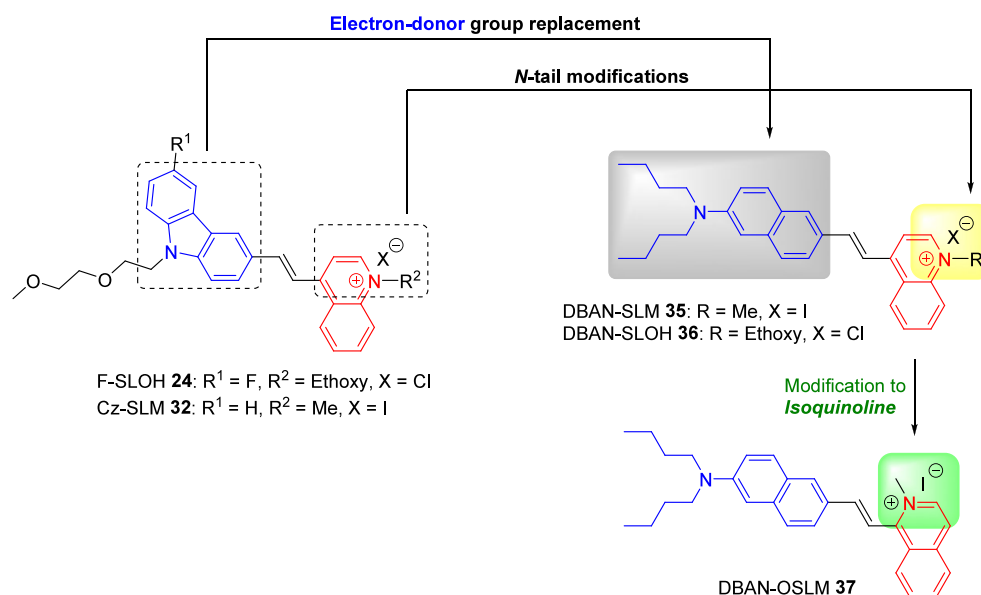
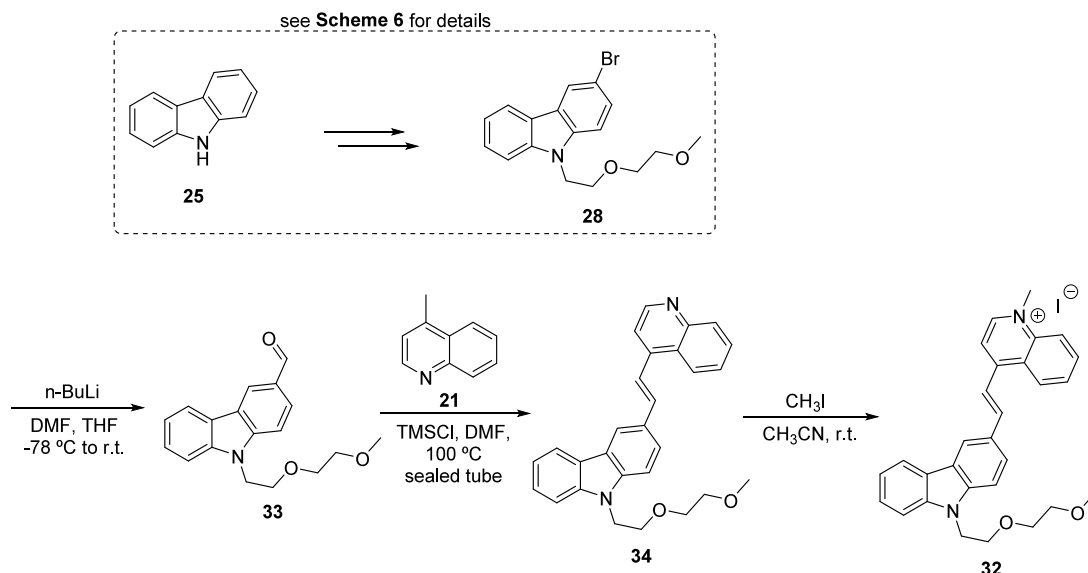
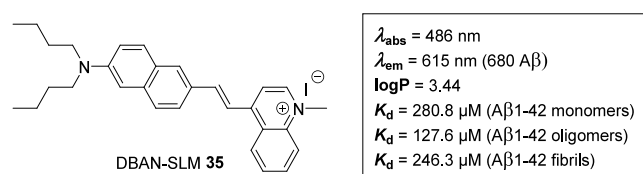


Figure 23. Design strategy for analogues DBAN-SLM 35, DBAN-SLOH 36, and DBAN-OSLM 37.

Figure 24. *In vitro* binding profile of DBAN-SLM 35.

zine was selected as the backbone scaffold, adding rhodanine units to establish the overall theranostic structure (Figure 9). The preference for phenothiazine and rhodanine frameworks was not clearly discussed and rationalized by the authors. However, we might assume that phenothiazine was chosen for its well-documented antiaggregation and antioxidant properties,^{63–66} as well as the presence of this tricyclic motif in several CNS drugs such as promethazine and chlorpromazine.⁶⁷ In the case of rhodanines the scenario is not so simple. These five-

membered heterocycles have been reported as effective tau antiaggregation motifs, and perhaps the increasing evidence suggesting a crosstalk between $A\beta$ and tau aggregation led the authors to include them in the design of theranostics.^{68–70} On the other hand, rhodanines are also known to bind a large number of targets with weak or moderate affinity, making them, in principle, suitable platforms to develop $A\beta$ -binding theranostics.⁷¹

When studying the native fluorescent properties, it was observed that all the compounds had emission wavelengths $\geq 640 \text{ nm}$ falling in an acceptable range for NIRF probes. The compounds 1 showed variable “turn-on” fluorescence intensity upon binding with $A\beta_{1-42}$ aggregates (2.3–13.1-fold), and no fluorescent response in the presence of $A\beta_{1-42}$ monomers. The authors advanced the hypothesis of compounds 1 to bind the hydrophobic pockets of $A\beta_{1-42}$ aggregates, constraining their rotation and enhancing their quantum yield upon binding to aggregate β -amyloid proteins.

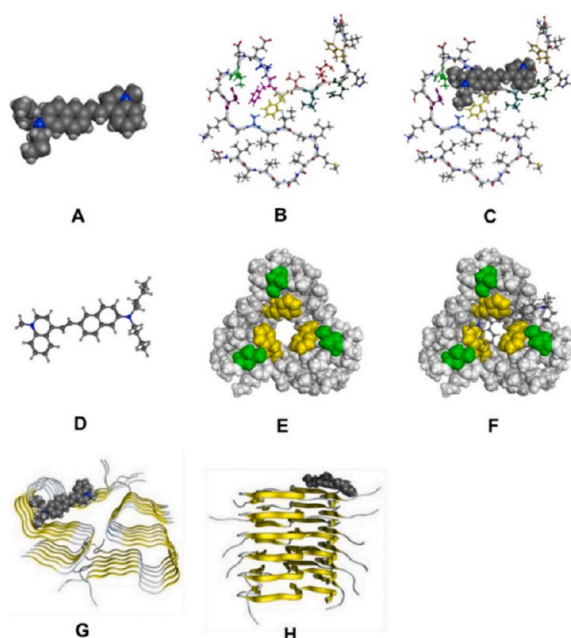


Figure 25. Model complex structure of DBAN-SLM 35 with (C) $A\beta_{1-42}$ monomer, (F) $A\beta_{1-40}$ trimer model, and (G and H) $A\beta_{1-42}$ fibril. In the trimer model, F19 and V36 residues are depicted in yellow and green, respectively. Reprinted in part with permission from ref 83. Copyright 2021 Elsevier.

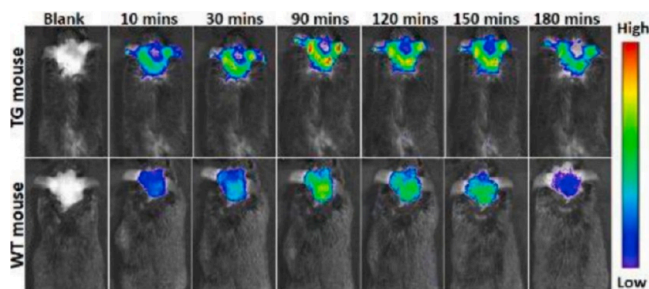


Figure 26. *In vivo* assessment: fluorescence images of 12-month-old Tg and WT mice at specific time points before or after the intravenous injection of DBAN-SLM 35. Reprinted in part with permission from ref 83. Copyright 2021 Elsevier.

In the end, although there were derivatives with higher fold intensity increases (>10), Chen et al. end up choosing derivative **1a** (Figure 10A) with only a 4.89-fold intensity enhancement because it exhibited good binding affinity toward $A\beta_{1-42}$ aggregates ($K_d = 7.5 \pm 0.4$ nM) while having a low micromolar IC_{50} value for the inhibition of $A\beta_{1-42}$ aggregation (0.67 ± 0.02 μ M). In addition, derivative **1a** demonstrated very weak interaction with bovine serum albumin (BSA) as well as low cytotoxicity in a human neuronal cell line (SH-SY5Y) up to 50 μ M.⁶² *In vitro* fluorescent staining assays of $A\beta$ plaques in brain and eye slices of double transgenic (APP^{wse}/PSEN1, 9-month old) mice overexpressing $A\beta$ demonstrated an excellent targeting ability of compound **1a** (Figures 10B and 10C).

The only mishap that **1a** showed was its predicted log P value of 3.68, which falls out of reference values (log $P = 2-3.5$) for potentially BBB-penetrating compounds.

The synthesis of the compound **1a** was accomplished by prior methylation of the amine of phenothiazine **2**, followed by the introduction of the aldehyde function onto *N*-methyl phenothiazine **3** via Vilsmeier–Haack reaction, and finally the

incorporation of the rhodanine derivative **5** by Knoevenagel condensation (Scheme 1). The required rhodanine derivative **5** was previously obtained upon reaction of ethyl glycinate **6** with trithiocarbodiglycolic acid **7** (Scheme 2).⁶²

The phenothiazine-rhodanine **1a** showed an interesting preliminary theranostic profile, but despite its emission wavelength of 680 nm and good affinity for $A\beta_{1-42}$ aggregates Chen et al. made an additional effort to push the emission further into the NIR region (>700 nm). To do so, the authors adjusted the length of the π -bridge between the phenothiazine and rhodanine moieties by means of additional double bonds ($n = 2$ or 3) designing the so-called second series of phenothiazine-rhodanine theranostics, compounds **8** and **9** (Figure 11).

With the second series of phenothiazine-rhodanine compounds **8** and **9** (Figure 11), the authors were indeed able to red-shift the native emission wavelength to 700 nm in five new derivatives, with fluorescent enhancement upon $A\beta$ binding from 2.0- to 13.0-fold.⁷² The intensity increase was generally escorted by a blue-shift in the emission spectra of 20–40 nm, together with a large increase in quantum yield. When the new compounds were assessed for their binding ability for $A\beta_{1-42}$ aggregates as well as their antiaggregation performance, the lead compound **8a** emerged with a K_d value of 10.2 nM and a IC_{50} of inhibition of 1.8 μ M (Figure 12).⁷² The second generation of phenothiazine-rhodanine theranostics **8** also showed high stability and low cytotoxicity, with maximum emission at 700 nm that blue-shifted to 680 nm upon binding $A\beta_{1-42}$ aggregates and with an emission intensity increase of 13.0-fold.⁷²

The direct comparison between the first- and second-generation lead compounds **1a** and **8a** (Figure 12), respectively, showed that the structural modifications to red-shift the emission wavelength had a slightly negative impact on both the binding affinity and the antiaggregation capacity.^{62,72} In both publications, Chen et al. reported interesting compounds with nanomolar affinities for amyloid species. However, both investigations have an important shortcoming related to the evaluation of the compounds' ability to cross BBB. The log P values of compounds **1a** and **8a** are indeed reported, but in at least an *in vitro* parallel artificial membrane permeability assay (PAMPA) assay to predict BBB penetration would be of paramount importance to select compounds to evolve to *in vivo* experimentation.

As discussed before, the synthetic strategy employed for compound **8a** (Scheme 3) was quite similar to that for the first generation of phenothiazine-rhodanine compounds. Starting with compound **4**, the original formyl tail of the phenothiazine backbone was extended further through reaction with 1,3-dioxolan-2-ylmethyl)triphenylphosphonium bromide in the presence of tris(3,6-dioxheptyl)amine (TDA-1) and K_2CO_3 , followed by *in situ* HCl hydrolysis to produce the enal **10** (Scheme 3). Then, the rhodanine **5** was installed through Knoevenagel condensation to give phenothiazine-rhodanine **8a** (Scheme 3).⁷²

In both generations of phenothiazine-rhodanine theranostics, the lead compounds share the same peripheric substituent in the rhodanine moiety, *i.e.*, an ethyl ester. In the following studies, Chen and co-workers came back to the first-generation lead **1a**, and attempted to improve its absorption, distribution, metabolism, and excretion (ADME) properties, particularly the aqueous solubility and bioavailability, and envisioned the installation of a metal chelating unit, believing that the poor solubility of the compound have impeded their application in NIR imaging *in vivo*. The rationale behind this development was

Scheme 8. Convergent Synthetic Approach for the Preparation of DBAN-SLM 35

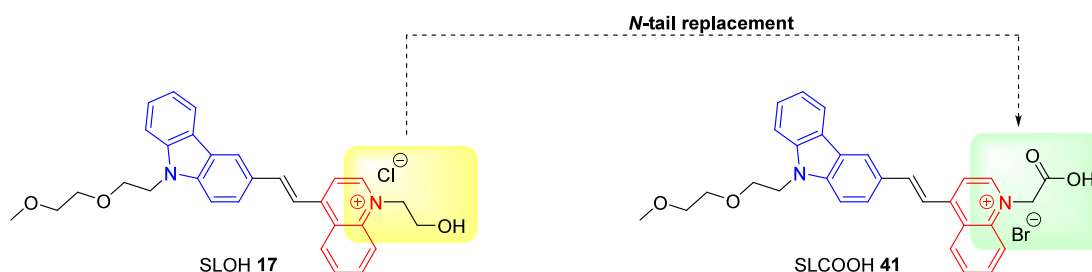
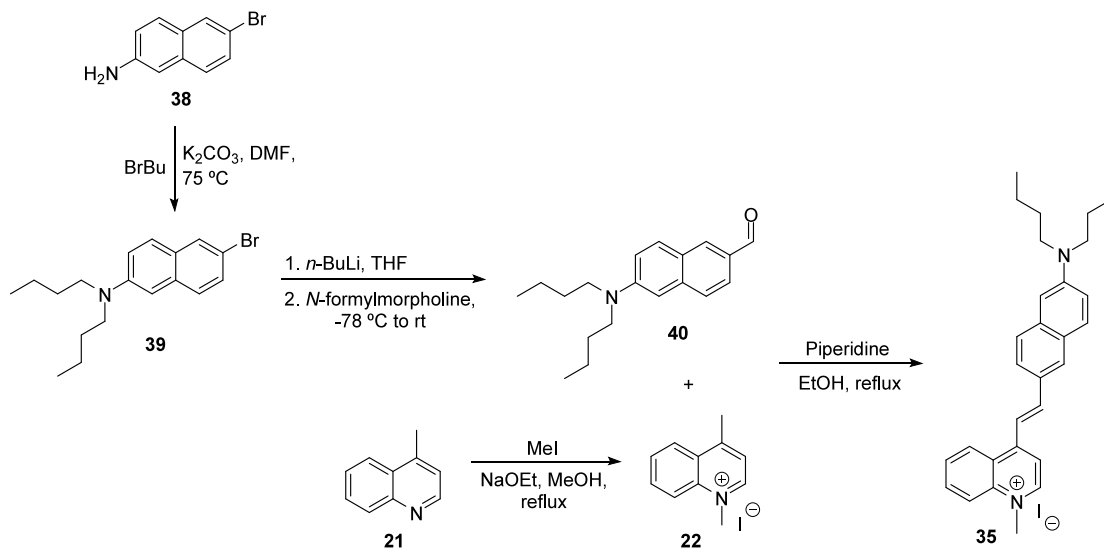


Figure 27. Design strategy for SLCOOH 41.

to run several replacements of water-soluble head groups in the rhodanine tail (Figure 13).^{73,74}

From the screening study of seven water-solubility-promoting substituents, two best-performing compounds emerged, the phenothiazine-rhodanines **11a** and **11c**, having a 2-(2-methoxyethoxy)ethyl ester group and a (2,2-dimethyl-1,3-dioxolan-4-yl)methyl group, respectively, as hydrophilic tails (Figure 14).

The compound **11c** (Figure 14A) presented a native emission wavelength of 670 nm, with a 22-fold intensity enhancement upon $A\beta$ binding. Again, a hypsochromic shift of 55 nm was observed upon incubation of compound **11c** with $A\beta$ aggregates. Compound **11c** also exhibited a K_d value of 24.5 nM and an IC_{50} value for the inhibition of $A\beta$ aggregation of 0.06 μ M. Subsequent studies indicated that compound **11c** has good biostability, exhibited low cytotoxicity at 50 μ M, and displayed some degree of neuroprotection to SH-SY5Y cells by decreasing $A\beta$ -induced toxicity and reducing the ROS level.⁷⁴ The computational ADMET studies suggested that compound **11c** can indeed be more soluble than the first-generation phenothiazine-rhodanine lead **1a**, with an appreciable predicted BBB penetration. Therefore, the phenothiazine-rhodanine theranostic **11c** moved forward to *in vivo* imaging experiments. The fluorescence staining assay on brain tissue from a double Tg mouse overexpressing $A\beta$ (C57BL6, APP^{swe}/PSEN1, 10 months old, male) showed that compound **11c** specifically stained $A\beta$ plaques both in cortex and hippocampus regions of the Tg mouse, overlapping well $A\beta$ plaque-specific thioflavin-T dye.⁷⁴

Similarly, the phenothiazine-rhodanine **11a** (Figure 14A) presented rather comparable properties compared to its analogue **11c**. The most notable difference is the 63.9-fold fluorescent intensity enhancement upon binding amyloid aggregates.⁷³ The *in vivo* imaging examinations on double Tg mice (C57BL/6, APP/PS1, 12 months old, male) using compound **11a** also demonstrated its ability to label β -amyloid plaques in brain slices (Figure 14C).⁷³

Concerning their synthesis, the theranostic compounds **11a** and **11c** were prepared following the procedure depicted earlier in Scheme 1, *i.e.*, through Knoevenagel condensation of phenothiazine-3-carbaldehyde **4** and the appropriately substituted rhodanines **14** and **16**. These later ones were presynthesized through Steglich esterification of 2-(4-oxo-2-thioxothiazolidin-3-yl)acetic acid **12** with (2,2-dimethyl-1,3-dioxolan-4-yl)methanol **13** or 2-(2-methoxyethoxy)ethan-1-ol **15** (Scheme 4).^{73,74}

Cyanine/Quinoline-Based Theranostics. The first example of cyanine-based theranostics was reported by Wong et al. in 2012, the so-called SLOH **17** (Figure 15) (reviewed elsewhere⁶⁰).⁷⁵ The underlying principle behind the use of cyanines as theranostics was grounded on investigations using carbazole-based cyanine fluorophores, reported to be suitable fluorescent light-up probes for double-stranded DNA and two-photon excited bioimaging.⁷⁶ This kind of compounds are also consistently reported to have strong fluorescence enhancement (>80-fold) upon binding the $A\beta$ peptide.⁷⁵

In a following effort, Wong et al. used the structure of SLOH **17** as the starting point to search for new theranostics with improved binding affinity toward $A\beta$ species, enhanced

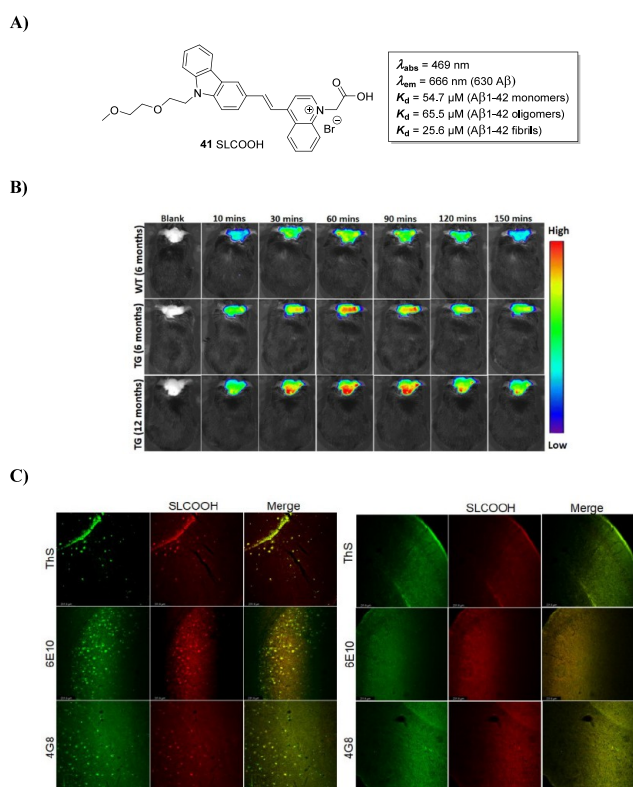


Figure 28. (A) *In vitro* binding profile of SLCOOH 41. (B) *In vivo* fluorescence brain imaging of 6- and 12-month-old 5XFAD Tg mice and a wild-type (WT) mouse. (C) *Ex vivo* images of SLCOOH 41 in brain slices of 6-month-old 5XFAD Tg and age-matched WT mice colocalized with ThS and a primary antibody (6E10 and 4G8) and then a secondary antibody conjugated with Alexa 488. Reprinted in part with permission from ref 84. Copyright 2023 Royal Society of Chemistry.

inhibition potency, more satisfactory BBB permeability for *in vivo* applications, and red-shifted emission wavelengths. Three different replacements of the carbazole moiety (dialkyl or diphenyl substituents) and one quinoline alkyl chain variation (methyl substituent) were assessed as depicted in Figure 15.⁷⁷

Among the examined compounds, the so-called DBA-SLOH 19 (Figure 16A) emerged as the one with the most interesting native fluorescent properties ($\lambda_{\text{abs}} = 550$ nm, $\lambda_{\text{em}} = 672$ nm), together with variable binding affinities toward distinct $A\beta$ species. For $A\beta_{1-40}$ species, K_{d} (fibrils) = 1.13 μM , K_{d} (oligomers) = 2.77 μM , and K_{d} (monomers) = 6.18 μM ; for $A\beta_{1-42}$ species, K_{d} (fibrils) = 3.09 μM , K_{d} (oligomers) = 5.66

μM , and K_{d} (monomers) = 13.12 μM .⁷⁷ These low micromolar K_{d} values of DBA-SLOH 19 represented a major improvement, since the K_{d} value of SLOH 19 toward $A\beta_{1-40}$ is 92 μM (92-fold improvement).⁷⁵ Concerning the antiaggregation potential of DBA-SLOH 19, it was demonstrated that it effectively inhibited the $A\beta_{1-42}$ self-aggregation with an IC_{50} value of 3.72 μM (Figure 16C). The proposed key feature of DBA-SLOH 19 was its medium length of alkyl chains, which promoted the highest binding affinity and high selectivity toward $A\beta$ species. It also demonstrated excellent BBB permeability and low cytotoxicity in neuroblastoma SH-SY5Y neuronal cells, being selected for further *in vivo* experiments on Tg mice.⁷⁷

Both the *ex vivo* costaining and *in vivo* experiments on APP/PS1 Tg mice (6 and 12 months old) (Figure 16B) suggested that DBA-SLOH 19 is highly specific to $A\beta$ plaques in the brain (Figure 16B), prompting its theranostic profile.⁷⁷

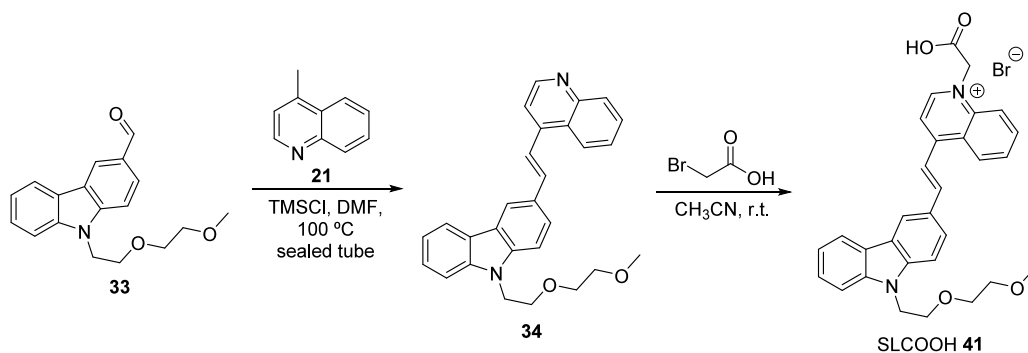
As regularly described for the majority of NIRF theranostics, the synthesis of DBA-SLOH 19 involved the Knoevenagel condensation of the *N,N*-dibutyl-*p*-aminobenzaldehyde 23 and the 4-hydroxyethylquinolinium salt 22 as the key reaction step (Scheme 5). The quinolinium salt 22 was presynthesized through *N*-alkylation of lepidine 21 with chloroethanol (Scheme 5).⁷⁷

Over the years, the scientific community has been arguing which amyloid species, *i.e.*, soluble $A\beta$ oligomers or insoluble $A\beta$ fibrils, are indeed the most neurotoxic, upstreaming the neurodegeneration process. In fact, cumulative clinical and nonclinical evidence strengthen the role of soluble $A\beta$ oligomers, making these species more neurotoxic than insoluble $A\beta$ fibrils in the plaques, causing dysfunction of neurotransmission and imbalance of neuronal excitability and ultimately resulting in neuronal death and memory loss.^{46,78}

Consequently, the development of selective probes for $A\beta$ oligomers with the additional ability to block oligomer formation is highly desirable in AD early diagnostics and therapeutics. In the particular case of carbazole-based probes, they usually show stronger binding affinities toward $A\beta$ fibrils than oligomers and/or monomers. Through the installation of a fluorine group in the carbazole moiety of SLOH 17, the new probe F-SLOH 24 became selective for $A\beta$ oligomers with a higher binding affinity over monomers or fibrils (Figure 17).⁷⁹

The initial assessment of the intrinsic fluorescent properties of F-SLOH 24 showed maximum absorption and emission wavelengths of 470 and 643 nm, respectively. Despite the low quantum yields presented by F-SLOH 24 ($\phi = 0.006$ in PBS and $\phi = 0.011$ in DMSO), it showed a stronger fluorescence enhancement upon binding to $A\beta$ oligomers compared to monomers and fibrils, ending up with a superior quantum yield

Scheme 9. Synthetic Approach for the Preparation of SLCOOH 41



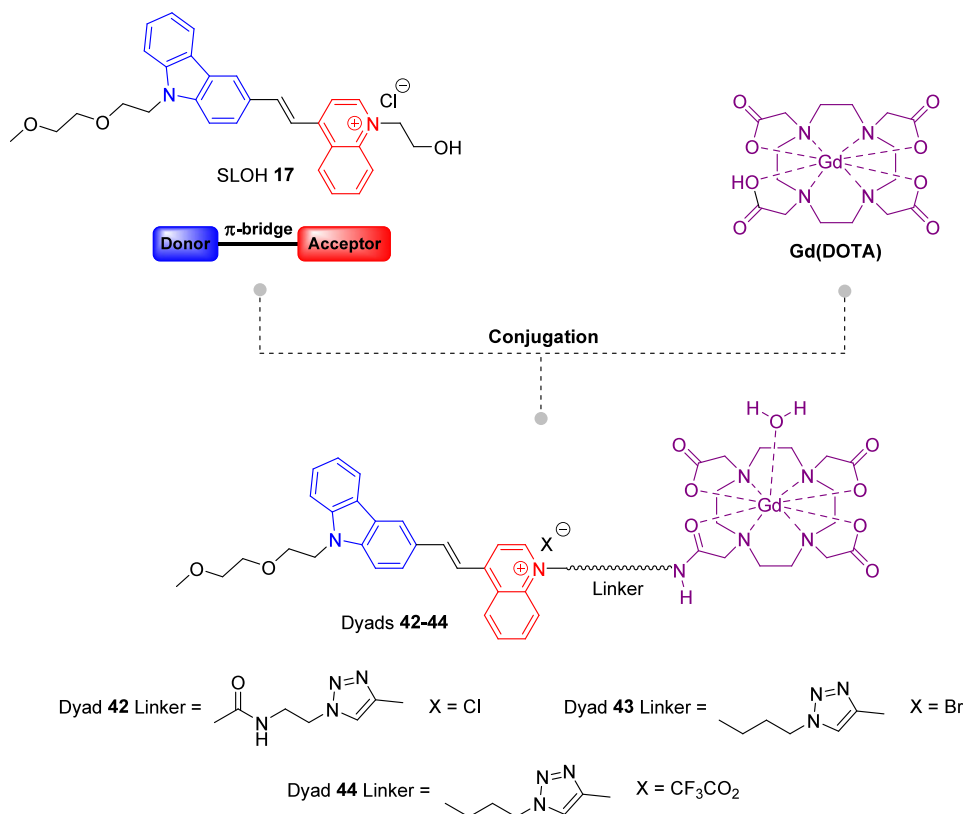


Figure 29. Conjugation approach to build-up dyads 42–44.

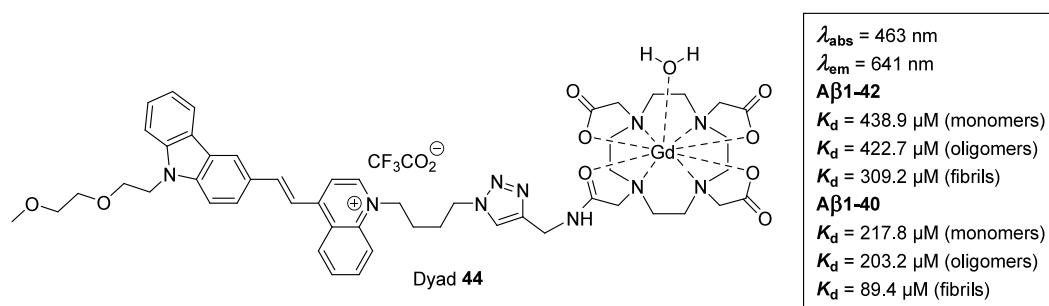


Figure 30. *In vitro* binding profile of dyad 44.

of 0.26.⁷⁹ The F-SLOH 24 showed quite distinct binding affinities toward $A\beta$ species, presenting considerably greater affinity toward $A\beta$ oligomers over monomers and fibrils (Figure 17). Moreover, the monitoring of the $A\beta_{1-40}$ fibrillation process at different time points using ThT and F-SLOH 24 demonstrated that the fluorescence enhancement of F-SLOH 24 upon binding $A\beta$ species is size-dependent, as after 2 h of incubation the fluorescence intensity of F-SLOH 24 decreases over time ($A\beta_{1-40}$ species larger than 300 nm).⁷⁹ The putative ability of F-SLOH 24 to interfere with $A\beta_{1-40}$ was investigated by circular dichroism (CD) and further confirmed by a ThT fluorescence assay. In fact, the *in vitro* self-aggregation process of $A\beta_{1-40}$ was clearly inhibited in the presence of one equivalent of F-SLOH 24 and further confirmed with an IC_{50} value of 3.4 μM .^{79,80} Furthermore, the $A\beta_{1-40}$ fibrillation process was instantly terminated upon addition of F-SLOH 24. The antiaggregation effects of F-SLOH 24 were also confirmed for the most toxic $A\beta_{1-42}$ species.⁷⁹ In a subsequent publication, F-SLOH 24 was extensively studied *in vivo* and proved effective for

the treatment of multiple neuropathological changes in AD mouse models.⁸⁰

Wong and colleagues also ran quantum mechanical calculations as well as docking search and molecular dynamic simulations for both assemblies of F-SLOH 24 and SLOH 17 with the $A\beta$ oligomer in order to rationalize the observed selective binding of F-SLOH 24 toward oligomers.

In both compounds, π - π stacking interactions favored the accommodation of the carbazole moiety in the F19 residue of $A\beta$ oligomer (Figure 18). Regarding the quinolinium moiety, it showed close proximity to the hydrophobic domain of the $A\beta$ oligomer, while the hydroxyethyl tail formed a $\text{CH}\cdots\text{O}$ interaction with the side chain of the V36 residue. Finally, the presence of fluorine in the carbazole offered another binding point with F19 residue through $\text{CH}\cdots\text{F}$ interaction, cumulatively explaining the F-SLOH 24 selectivity toward oligomers.⁷⁹

The toxicity of F-SLOH 24 was evaluated on the neuronal SH-SY5Y cell line, and the results indicate very low cytotoxicity with an LC_{50} value of 49 μM , as well as noticeable

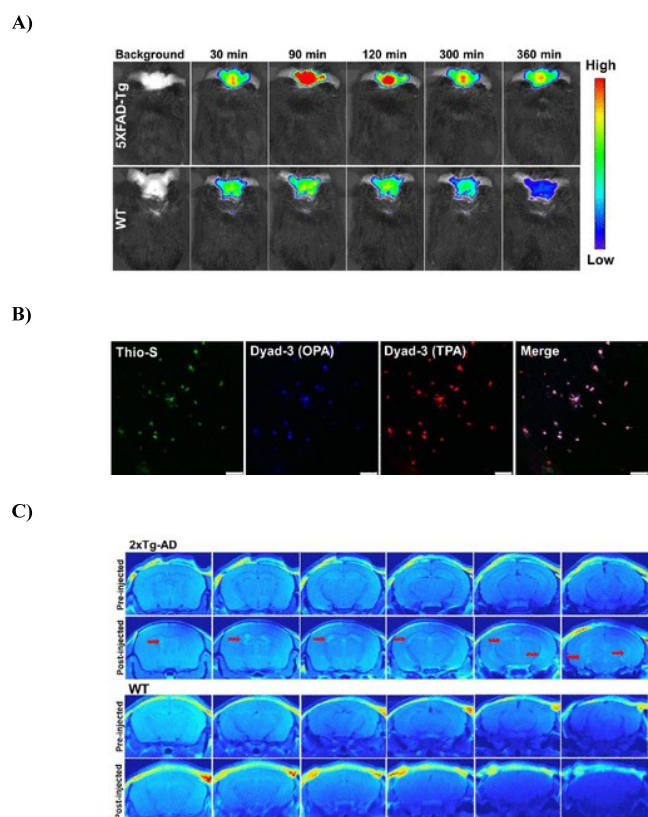


Figure 31. (A) *In vivo* fluorescence images of 12-month-old 5XFAD Tg and age-matched WT mice before and after administration with dyad 44 (Dyad-3 in the original article). (B) *Ex vivo* images of the brain slices of a 5XFAD Tg-mouse excited by one-photon (OPA) and two-photon (TPA) excitation costained with ThS. (C) *In vivo* T_1 -weighted MR pseudocolor mapped images of 6-month-old double Tg-AD and age-matched WT mice before and after the injection of dyad 44. Reprinted in part with permission from ref 88. Copyright 2021 American Chemical Society.

neuroprotective effect (~ 25 – 75%) on primary hippocampus neuronal cells against $A\beta$ -induced toxicity. The promising neuroprotective profile of F-SLOH 24 was further demonstrated by its ability to reduce the level of reactive oxygen species (ROS) as well as the calcium uploading of neuronal cells upon coincubation with both $A\beta_{1-40}$ and $A\beta_{1-42}$.⁷⁹

The encouraging *in vitro* profile of F-SLOH 24 prompted its application for further specific detection and labeling of $A\beta$ oligomers in Tg mouse brain tissue. The colocalization studies with SLOH 17, F-SLOH 24, and thioflavin-S (ThS) indicated that F-SLOH 24 is indeed capable of staining the transient and unstable oligomer species present in the transition to fibril elongation, and these indications were further confirmed using an $A\beta$ oligomer-specific antibody ($A\beta$ -Oligo). The *in vivo* potential of F-SLOH 24 was also demonstrated in imaging experiments of 7-month-old AD mouse models (Figure 19). First, an intense fluorescence signal of F-SLOH 24 was observed in the brains of both the Tg and WT mice within 10 min compared to that of the preinjected mouse, indicating that F-SLOH 24 was indeed capable to cross BBB with a high initial brain uptake (Figure 19).⁷⁹

Further colocalization studies with ThS and several antibodies showed a colocalization extent between F-SLOH 24 and $A\beta$ -Oligo of $\sim 90\%$, higher than 6E10, 4G8, p $A\beta$, or ThS (~ 50 –

65%), supporting the specificity of F-SLOH 24 to $A\beta$ oligomers *in vivo* (Figure 20).⁷⁹

The whole story behind F-SLOH 24 is quite an example of how the introduction of a fluorine in a compound can significantly change its properties. Many more examples of the role of fluorine in medicinal chemistry can be found in the literature (for a relevant review on the topic, see ref 81).

In the specific case of F-SLOH 24, the installation of fluorine in the carbazole moiety and subsequent synthesis of the overall scaffold of F-SLOH 24 was not straightforward, requiring a stepwise synthetic methodology (Scheme 6). The synthetic endeavor toward F-SLOH 24 followed a convergent approach, starting with the *N*-alkylation of carbazole 25 with 2-(2-chloroethoxy)-1-methoxyethane 26 (Scheme 6). Then, the *N*-alkylated carbazole 27 was selectively brominated using NBS as halogen source (Scheme 6). The Br was subsequently replaced by lithium using BuLi (classical metal–halogen exchange), allowing the fluorination of carbazole with *N*-fluorobenzene-sulfonimide (NFSI) as the fluorination agent (Scheme 6). The presence of the fluorine in the carbazole 29, worked as directing group for the second bromination, afforded the dihalogenated carbazole 30 (Scheme 6). Afterward, the Br substitution was used to install the required formyl group through a metal–halogen exchange strategy and further reaction with dimethylformamide (DMF), affording the F-substituted carbazole-3-carbaldehyde 31, the first component of the convergent strategy (Scheme 6). The second component, *i.e.*, the 1-(2-hydroxyethyl)-4-methylquinolin-1-ium chloride 34, was obtained through *N*-alkylation of lepidine 32 with 2-chloroethanol 33 (Scheme 6).

Finally, both components, the F-substituted carbazole-3-carbaldehyde 31 and 1-(2-hydroxyethyl)-4-methylquinolin-1-ium chloride 22, were coupled together through a piperidine-promoted condensation reaction to complete the π -bridge between the donor and the acceptor units (Scheme 6).⁷⁹

In 2018, Wong and colleagues revisited the structure of SLM 20 (Figure 15), aiming to develop a theranostic compound with *in vivo* efficacy to improve cognitive decline and decrease the content of $A\beta$ plaques and tau in AD mouse models.⁸² The working approach was to replace the electron-donor group of SLM 20 with the carbazole moiety, like the one present in SLOH 17 (Figure 15), to build up the final structure of the so-called Cz-SLM 32 (Figure 21). The main difference between the SLOH 17 and Cz-SLM 32 structures is the *N*-hydroxyethyl tail, which was replaced by a *N*-methyl group (Figure 21).

Cz-SLM 32 showed distinctive K_d values upon binding $A\beta$ species, *i.e.*, $K_d(A\beta_{1-40})$ fibril = 13.1 and 96.6 μM and $K_d(A\beta_{1-42})$ = 11.4 and 40.2 μM for fibril and monomer, respectively, with measured $\lambda_{\text{abs}}/\lambda_{\text{em}}$ = 455/676 nm (Figure 22A).⁸² Although not clear enough why the authors did not measure the binding affinity of Cz-SLM 32 toward oligomers, it might be due to the absence of both structural features responsible for oligomer binding, *i.e.*, the hydroxyethyl tail on the quinolinium moiety and the fluorine atom on the carbazole. As such, it is reasonable to expect a low binding affinity of Cz-SLM 32 for $A\beta$ oligomers.

Nevertheless, the study followed its natural course, and the *in vivo* applicability of Cz-SLM 32 in imaging $A\beta$ species was investigated using 9-month-old APP/PS1 Tg mice. The results seem to point for the ability of Cz-SLM 32 to bind $A\beta$ species *in vivo*, although the kind of species (monomers, oligomers or fibrils) is not clear. Subsequent *ex vivo* costaining experiments with $A\beta$ plaque-specific ThT dye indicate that Cz-SLM 32 is

Scheme 10. Synthesis of the Multifunctional Dyad 44

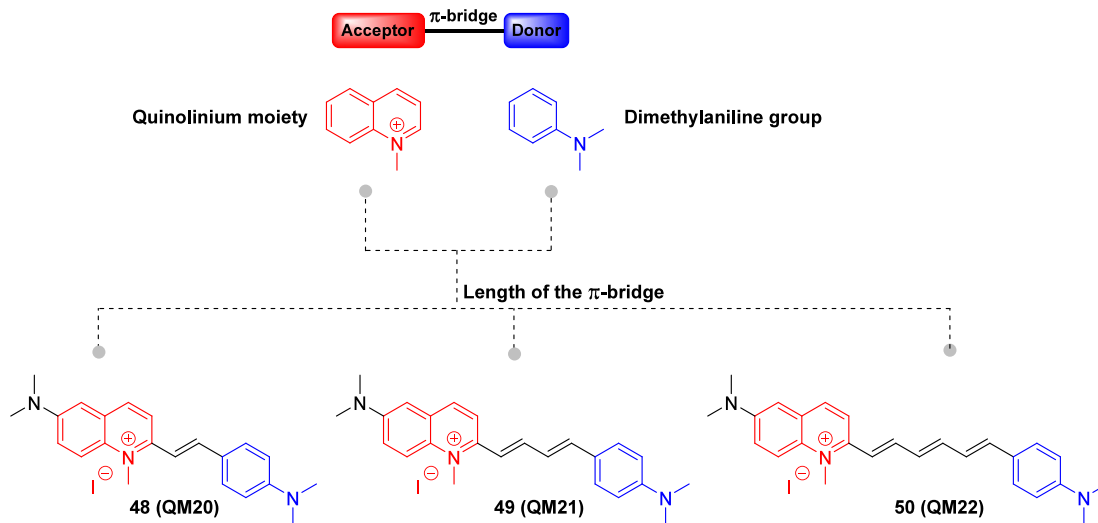
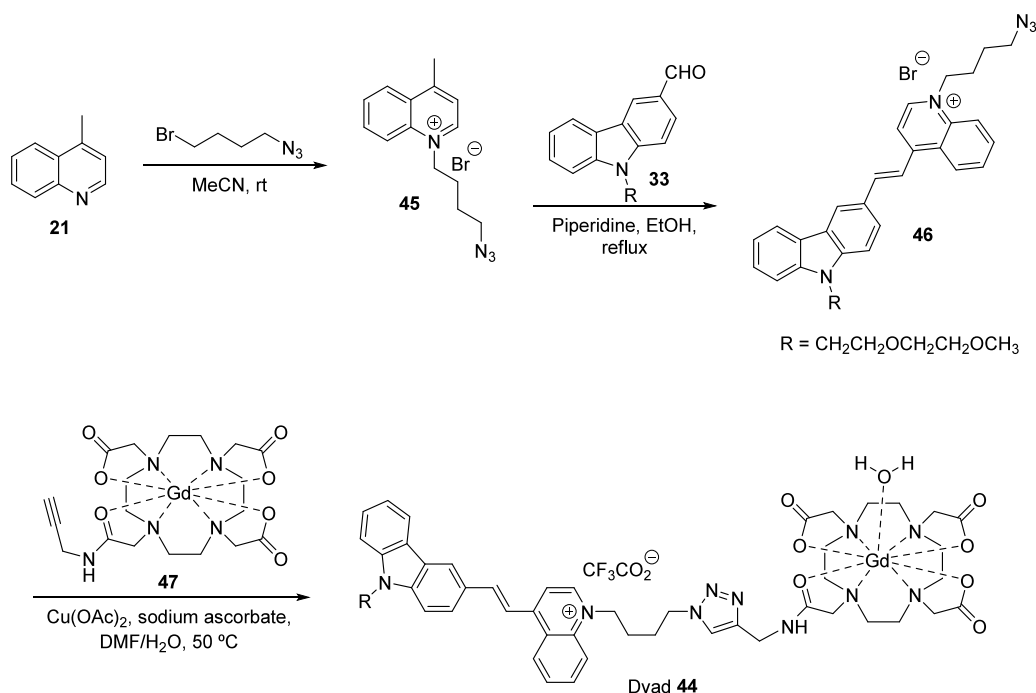


Figure 32. Design strategy for the development of “off-on” D- π -A photosensitizers 48–50.

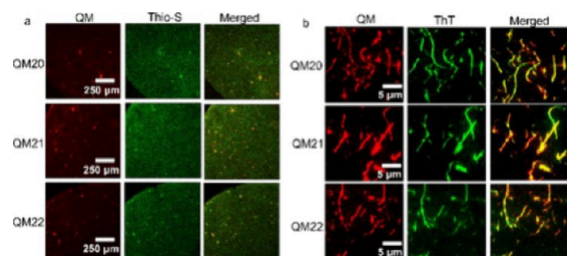


Figure 33. (a) Confocal light microscopy images of A β fibrils costained with ThS and compounds 48–50 (QM20–QM22, respectively, in the original article) on APP/PSI mouse brain slices in the cortex region. Scale bar represents 250 μ m. (b) Fluorescence images of A β fibrils costained with ThT and compounds 48–50. Reprinted in part with permission from ref 92. Copyright 2022 American Chemical Society.

highly specific for A β plaques, but it can also strongly bind to A β oligomers (Figure 22B).⁸²

Cz-SLM 32 also appears to have the capacity to inhibit the oligomerization of A β _{1–42}, displaying a neuroprotective effect on both A β _{1–42} and ROS-induced toxicity in primary hippocampal cells over a period of 24 h.⁸² The *in vivo* profile of Cz-SLM 32 was further assessed in triple transgenic AD mice in order to evaluate its effects against cognitive impairment. The intraperitoneally administered Cz-SLM 32 indeed had an important impact by shortening the latency to escape onto the hidden platform as compared to the control Tg mice on days 3, 4, and 5 (Morris water maze tests). Furthermore, the Cz-SLM 32-treated mice traveled to the previously learned platform quadrant more frequently than the control ones, the time spent in the previously learned platform quadrant being longer for the treated mice. Interestingly, the treated mice showed a relevant reduction in

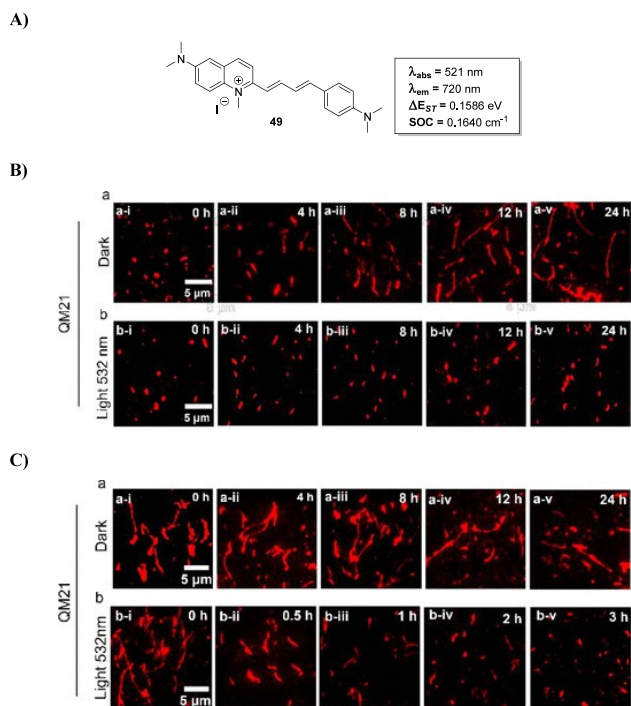


Figure 34. (A) Photophysical properties of compound 49. (B) Status of the $A\beta$ monomers stained with compound 49 (QM21 in the original article) with/without irradiation (532 nm) at specific time points between 0 and 24 h monitored by fluorescence confocal microscopy. (C) Status of $A\beta$ aggregates stained with compound 49 with/without irradiation (532 nm) at specific time points between 0 and 3/20 h monitored by fluorescence confocal microscopy. Reprinted in part with permission from ref 92. Copyright 2022 American Chemical Society.

oligomeric $A\beta$ contents (8, 12, 16, 25, 40, and 55 kDa) and tau proteins [total tau (tau-5) and phosphorylated tau (ps422)] in hippocampal regions of the brain.⁸²

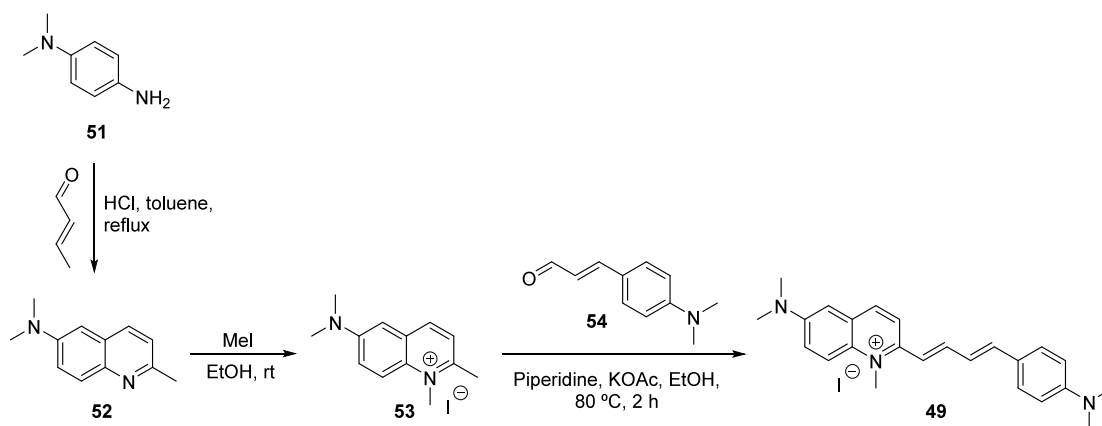
The synthetic strategy for Cz-SLM 32 is quite similar to the one employed for F-SLOH 24, but with slight modifications in the π -bridge build up. Actually, the required brominated carbazole intermediate 28 is prepared in two reactions steps through N -alkylation followed by bromination of carbazole 25 (see Scheme 6 for details). Then, the formyl group was installed through reaction with DMF after a lithium–halogen exchange reaction promoted by BuLi, affording the desired formyl-carbazole 33 (Scheme 7).

From the formyl-carbazole intermediate 33 on, the synthetic strategy was inverted in comparison to the one of F-SLOH 24. This means that the double bond was built through TMSCl-promoted reaction of lepidine 21 with formyl-carbazole 33 prior to the final N -methylation of compound 34 with iodomethane (Scheme 7).⁸²

In 2021, Wong and colleagues made an additional effort to expand a bit further the chemical space of theranostic probes focused on $A\beta$ oligomers. The above-described F-SLOH 24 and Cz-SLM 32 (Figure 17 and Figure 22A) were revisited as leading assemblies for further modifications to tackle the common hypsochromic shift in emission upon binding with $A\beta$ species, which normally falls into emission wavelengths below 650 nm. In order to mitigate this pitfall, Wong et al. formulated additional turn-on fluorophores based upon carbazole replacement with the 2-naphthylamine framework, as well as quinolinium N -tail modifications and quinoline replacement with isoquinoline, searching for the optimal photophysical and biological properties (Figure 23). Following this strategy, the authors came up with three new D-A structured compounds, DBAN-SLM 35, DBAN-SLOH 36, and DBAN-OSLM 37 (Figure 23), to be further investigated for their theranostic potential.⁸³

The native fluorescence profile in organic solvents of the three new analogues 35–37 showed a pronounced solvatochromic effect with absorption and emission wavelengths of 486–621 nm and from 615–816 nm, respectively.⁸³ In physiological buffer (PBS, 20 mM, pH 7.4), the fluorescent properties were narrowed to absorption and emission wavelengths of 486–521 nm and 604–615 nm, together with very low quantum yields ($\phi = 0.01$ – 0.02%).⁸³ The initial goal of red-shifting the emission of DBAN-SLM 35, DBAN-SLOH 36, and DBAN-OSLM 37 was only barely accomplished, as all the three compounds presented $\lambda_{em} = 650$ – 685 nm upon binding with $A\beta$ species including monomers, oligomers, and fibrils.⁸³ The binding affinities of DBAN-SLM 35, DBAN-SLOH 36, and DBAN-OSLM 37 varied a lot upon incubation with either $A\beta_{1-40}$ and $A\beta_{1-42}$ species, although it was possible to identify a stronger fluorescent enhancement in the presence of oligomers and monomers over fibrils.⁸³ DBAN-SLM 35 emerged as lead compound with 40–103- and 51–126-fold fluorescence enhancement upon binding with $A\beta_{1-40}$ and $A\beta_{1-42}$ species, respectively.⁸³ The estimated K_d of DBAN-SLM 35 confirmed the selectivity and specificity toward $A\beta$ oligomers, *i.e.*, $K_d(A\beta_{1-40}) = 39.3$, 20.1, and 71.1 μM and $K_d(A\beta_{1-42}) =$

Scheme 11. Synthetic Strategy to Prepare the Lead Compound 49



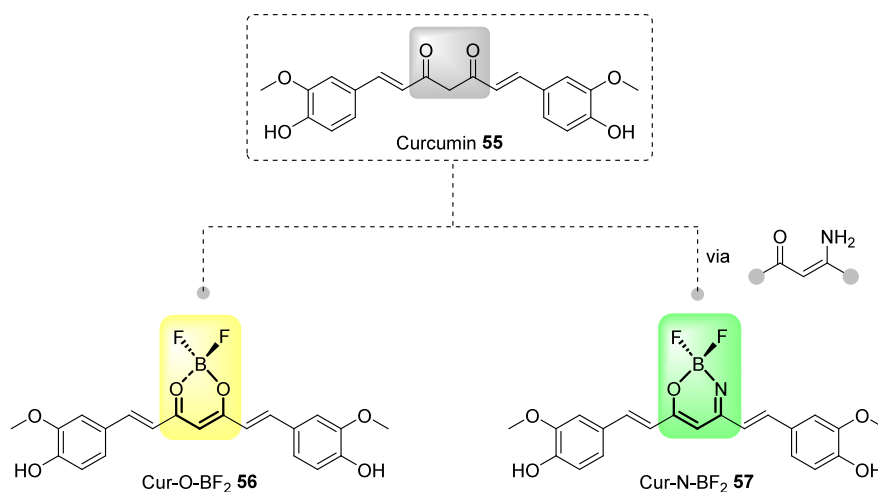


Figure 35. Design strategy of Cur-O-BF₂ 56 and Cur-N-BF₂ 57 AIE fluorophores from curcumin 55.

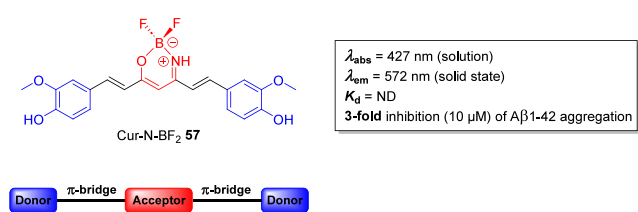


Figure 36. Cur-N-BF₂ 57 as an AIE theranostic with neuroprotective effects.

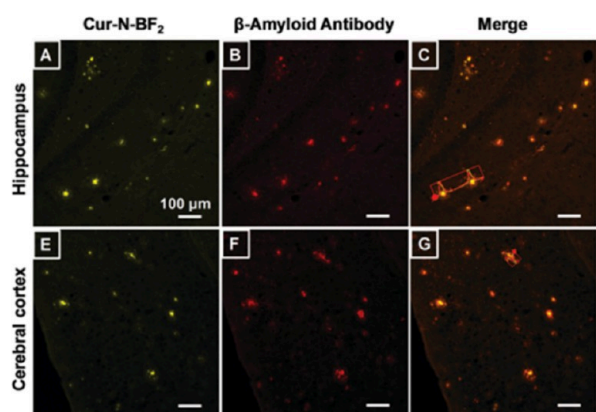


Figure 37. Imaging assessment of hippocampus and cerebral cortex brain slices from APP/PS1 mice. These slices were stained with (A and E) Cur-N-BF₂ 57 and with (B and F) β -amyloid antibody. Reprinted in part with permission from ref 98. Copyright 2019 Royal Society of Chemistry.

246.3, 127.6, and 280.8 μ M for the fibril, oligomer, and monomer, respectively (Figure 24).

The selectivity of DBAN-SLM 35 for amyloid oligomeric assemblies can be explained by the adoption of a slightly twisted geometry with the quinolinium ring entrapped within the hydrophobic pocket (hydrophobic F19/V36 residues of A β ₁₋₄₀), which is absent in the case of monomers and fibrils (Figure 25).⁸³

The estimated log *P* values of the new compounds indicate that only DBAN-SLM 35 and DBAN-OSLM 37 have the potential to cross the BBB. The experimental evidence using SXFAD Tg and WT mice only confirmed the ability of DBAN-

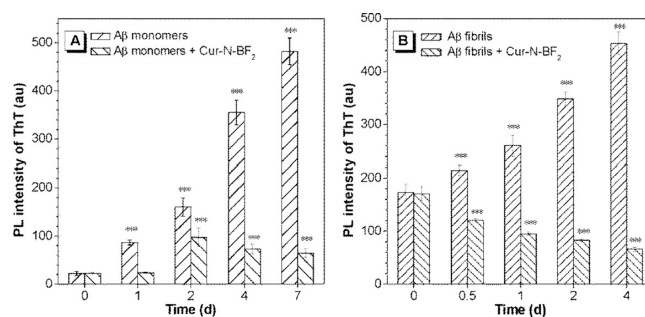


Figure 38. ThT fluorescence assay for monitoring the formation and disassembly of A β ₁₋₄₂ fibrils. (A) The monomeric A β ₁₋₄₂ peptides (20 μ M) were incubated with Cur-N-BF₂ 57 (10 μ M) for 0, 1, 2, 4, and 7 days. (B) The A β ₁₋₄₂ fibrils (20 μ M) formed at day 2 were incubated with and without Cur-N-BF₂ 57 (10 μ M) for 0.5, 1, 2, and 4 days at 37 °C. Reprinted in part with permission from ref 98. Copyright 2019 Royal Society of Chemistry.

SLM 35 to cross the BBB and therefore its possible *in vivo* applicability (Figure 26).

Concerning the synthetic strategy toward the preparation of DBAN-SLM 35 (Scheme 8), it follows the overall procedure reported for the above-discussed quinoline-based compounds. The electron-donor component 40 was prepared in two steps: the *N*-bisalkylation of 6-bromonaphthalen-2-amine 38 with 1-bromobutane (BrBu), followed by bromo-lithium exchange and formylation with *N*-formylmorpholine to give the 6-(dibutylamino)-2-naphthaldehyde 40 (Scheme 8). The synthesis of DBAN-SLM 35 was finally accomplished via piperidine-promoted condensation of *N*-methyl quinolinium 22 with 6-(dibutylamino)-2-naphthaldehyde 40 (Scheme 8).

Given the multifactorial nature of AD, the development of multitarget or multifunctional drugs with the ability to hit AD-related targets such as the prevention of A β aggregation and deposition, the alleviation of tau hyperphosphorylation, the amelioration of synaptic deficits, or the prevention of neuronal loss is highly desirable. With this idea in mind, Wong and co-workers developed an A β -targeting theranostic compound with the additional capacity to reduce A β -induced toxicity, inhibit the A β -induced ROS production, and relieve the A β and tau pathologies. Again, the compound in question is a SLOH 17 analogue, which results from the replacement of the *N*-ethanol tail with a *N*-propionic acid group, resulting in SLCOOH 41

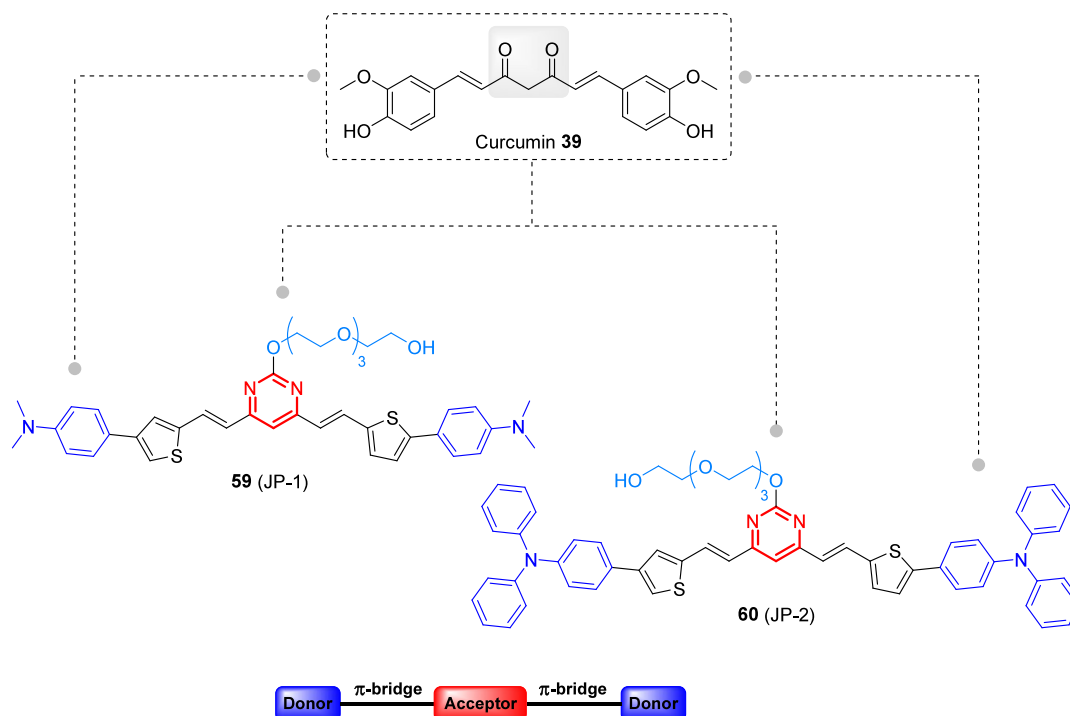
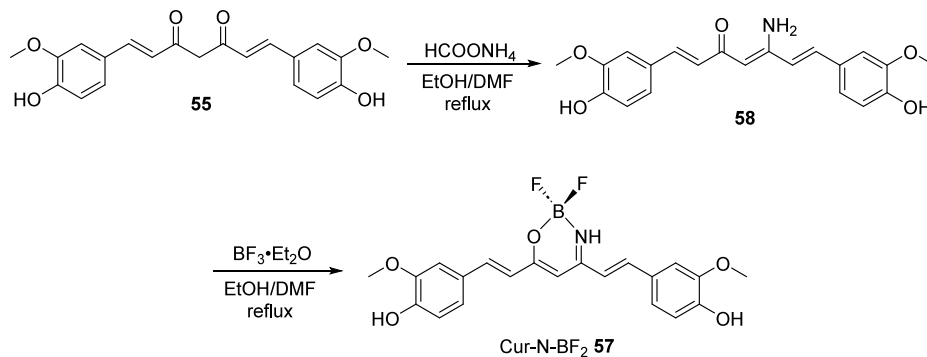
Scheme 12. Two-Step Synthetic Approach to Prepare Cur-N-BF₂ 57

Figure 39. Structural design of curcumin surrogates 59 and 60.

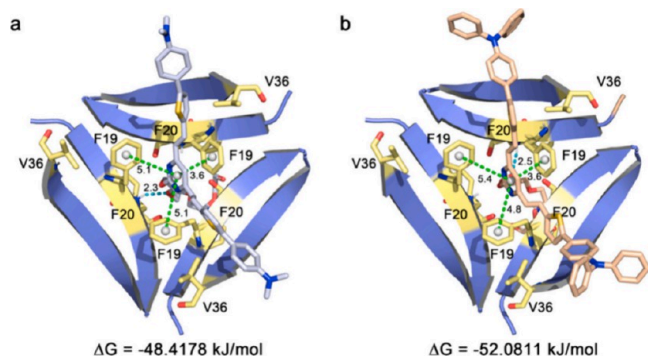


Figure 40. Docking assessment of (a) compound 59 (JP-1 in the original article) and (b) 60 (JP-2 in the original article) with A β oligomer. The hydrogen-bond and π - π stacking interaction were shown as green dots. Reprinted in part with permission from ref 99. Copyright 2021 Elsevier.

(Figure 27).⁸⁴ The previously reported analogues SLOH 17 and Cz-SLM 32 were shown to exhibit different degrees of A β aggregation inhibition *in vitro*, low cytotoxicity toward SH-SY5Y

cells, and *in vivo* therapeutic effects in an AD-affected mouse. This means that the biological properties can easily be tuned by modifying the *N*-substituent on the quinolinium ring.

SLCOOH 41 exhibited strong absorption at 469 nm and emission at 666 nm, together with a very low quantum yield in PBS (0.003). On the other hand, the SLCOOH 41 showed strong fluorescence turn-on concomitant with a blue-shift in emission upon binding A β_{1-42} fibrils (265-fold enhancement). The dissociation constants were reported as 54.7 μM for monomers, 65.5 μM for oligomers, and 25.6 μM for fibrils.⁸⁴ Noteworthy, the carboxylic acid replacement resulted in the loss of selectivity within A β species (monomers, oligomers and fibrils), but on the other hand it gave SLCOOH 41 selectivity over tau-441 aggregates, BSA, α -synuclein, IgM, IgG, human serum albumin (HAS), L-cysteine, IAPP (islet amyloid polypeptide), and PrP. Additionally, SLCOOH 41 demonstrated the capacity to displace ThT from the ThT/A β_{1-42} aggregate complex ($K_d = 2.31$ μM). This was indeed a good indication that SLCOOH 41 could interfere with and inhibit the A β_{1-42} aggregation. Compound 41 was further determined as

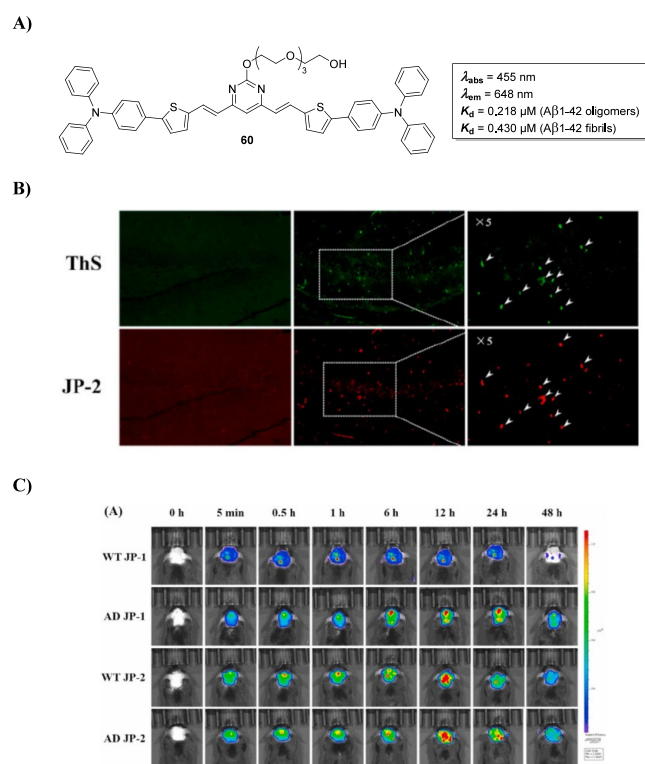


Figure 41. (A) *In vitro* binding properties of compound **60** (JP-2 in the original article). (B) Histological staining on brain slices in the hippocampus region from APP/PS1 Tg mice with ThS and compound **60**. (C) *In vivo* mapping of A β deposition in AD model mice (C57BL6, APP/PS1, 5-month-old, male) and WT mice (C57BL6, 5-month-old, male). Reprinted in part with permission from ref 99. Copyright 2021 Elsevier.

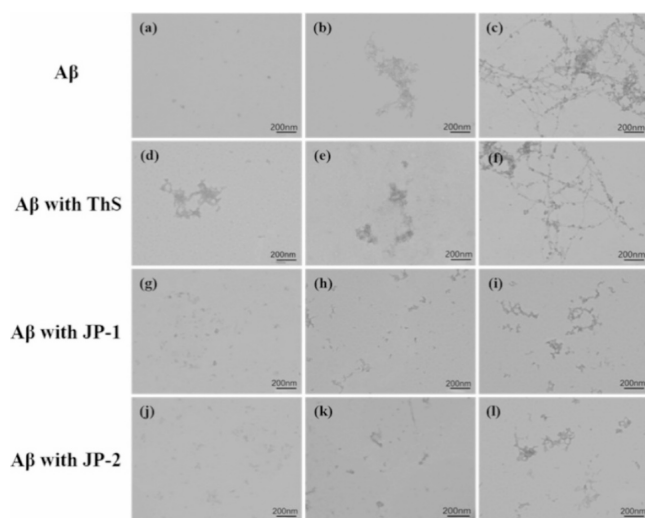


Figure 42. TEM images of A β _{1–42} fibril grown (a–c) without and the presence of (d–f) ThS, (g–i) compound **59** (JP-1 in the original article), and (j–l) compound **60** (JP-2 in the original article) after 24 h incubation at 37 °C by seed-mediated growth. Reprinted in part with permission from ref 99. Copyright 2021 Elsevier.

nontoxic and neuroprotective in human neuroblastoma SH-SY5Y cells, reducing the A β -induced ROS production.

The *in vivo* brain imaging performance of SLCOOH **41** was also assessed in 6- and 12-month-old 5XFAD Tg mice and a wild-type mouse. Strong fluorescence signals were observed in

the tested mice over a period of 150 min (Figure 28B), confirming the BBB permeability of the tested compound. Subsequent *ex vivo* costaining studies with A β plaque-specific staining dye, ThS, and A β antibodies (6E10 or 4G8), reinforced the A β -targeting capability of SLCOOH **41** (Figure 28C). Therapeutically, the SLCOOH **41**-treated AD mice showed marked improvement in their total escape latencies in the 5 day hidden platform test and significantly lower contents of tau and phosphorylated tau in the brains.⁸⁴ Following a similar synthetic strategy as for the previous carbazole compounds, SLCOOH **41** was prepared through condensation of formyl carbazole **33** with lepidine **21** and then *N*-alkylation with bromoacetic acid (Scheme 9).

Despite the potential of NIRF theranostics described so far in this Review, they all contain the limitation of being routinely used in AD patients mainly due to their shallow tissue penetration. Magnetic resonance imaging (MRI) is the most universally used clinical technique/tool for disease diagnostics due to its noninvasiveness, high temporal and spatial resolution, and deep tissue penetration, yet it suffers from intrinsic low sensitivity to A β plaques.⁸⁵ To overcome this pitfall, contrast agents are often employed to enhance the image contrast, resulting in hyphenated imaging techniques such as combinations of magnetic resonance, fluorescence (in the visible or near-infrared region), and two-photon excited fluorescence (TPEF). The most common MRI contrast agents are based on gadolinium(III) complexes such as Gd(DOTA) (DOTA, 1,4,7,10-tetraazacyclododecane-1,4,7,10-tetraacetic acid) and Gd(DTPA) (DTPA, diethylenetriaminepentaacetic acid), which usually offer bright images while having good biostability and high inertness.⁸⁶ However, when it comes to their applicability in targeting A β species, Gd(III) complexes present the huge limitation of very low BBB penetrability and lack of A β specificity.⁸⁷ To somehow tackle this hitch, Wong and colleagues reported in 2021 the conjugation of Gd(DOTA) complex with the former NIRF theranostic SLOH **17** through triazole linkers obtained by a copper(I)-catalyzed azide–alkyne click reaction (Figure 29).⁸⁸

Employing the strategy depicted in Figure 29, three dyads were produced differing both in the linker and the respective counterion. Dyad **44** (Figure 30) exhibited improved solubility in PBS, prompting its further bioapplication, while having absorption and emission wavelengths of 463 and 641 nm in PBS and 490 and 642 nm in DMSO, respectively. The quantum yield of dyad **44** was very low, but upon excitation above 800 nm the compound displayed strong TPEF with a maximum two-photon brightness ($\delta_2\Phi$) of ~ 210 GM at 950 nm.⁸⁸ The binding affinity for different A β species was not very good, with K_d values ranging from 89.4 μ M for A β _{1–40} fibrils to 438.9 μ M for A β _{1–42} monomers (Figure 30).⁸⁸ This means that the linkage of Gd(DOTA) with the SLOH **17** precursor had a negative impact in the binding affinity for A β species (see Table 1 for comparison purposes).

The imaging performance of dyad **44** was then evaluated in brains of 12-month-old 5XFAD Tg mice that overexpressed A β species and age-matched WT mice, in which strongly increased fluorescence in the Tg mouse was observed after 90 min due to the A β binding-induced fluorescence enhancement of dyad **44** in the Tg mouse (Figure 31A). The binding toward A β was further confirmed through *ex vivo* colocalization studies in brain slices of Tg mice upon one-photon (OPA) and two-photon (TPA) excitations, showing good colocalization with ThS (Figure 31B) and confirming the suitability of dyad **44** for

Scheme 13. Convergent Synthesis of Theranostics 59 and 60

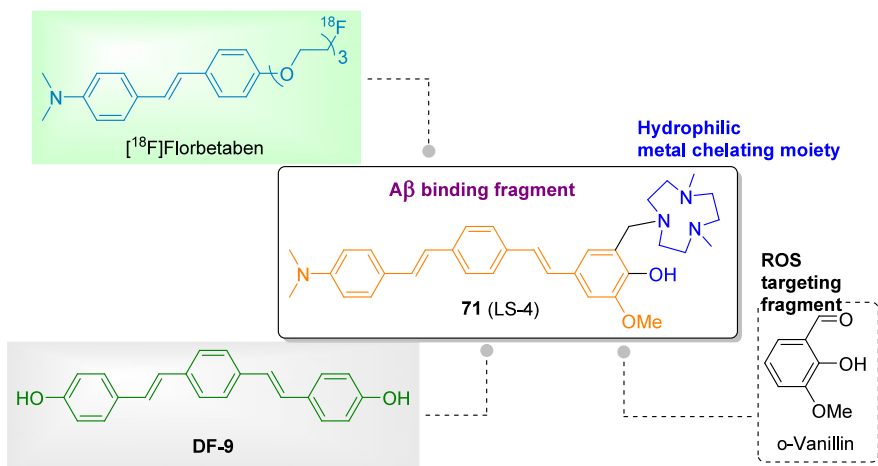
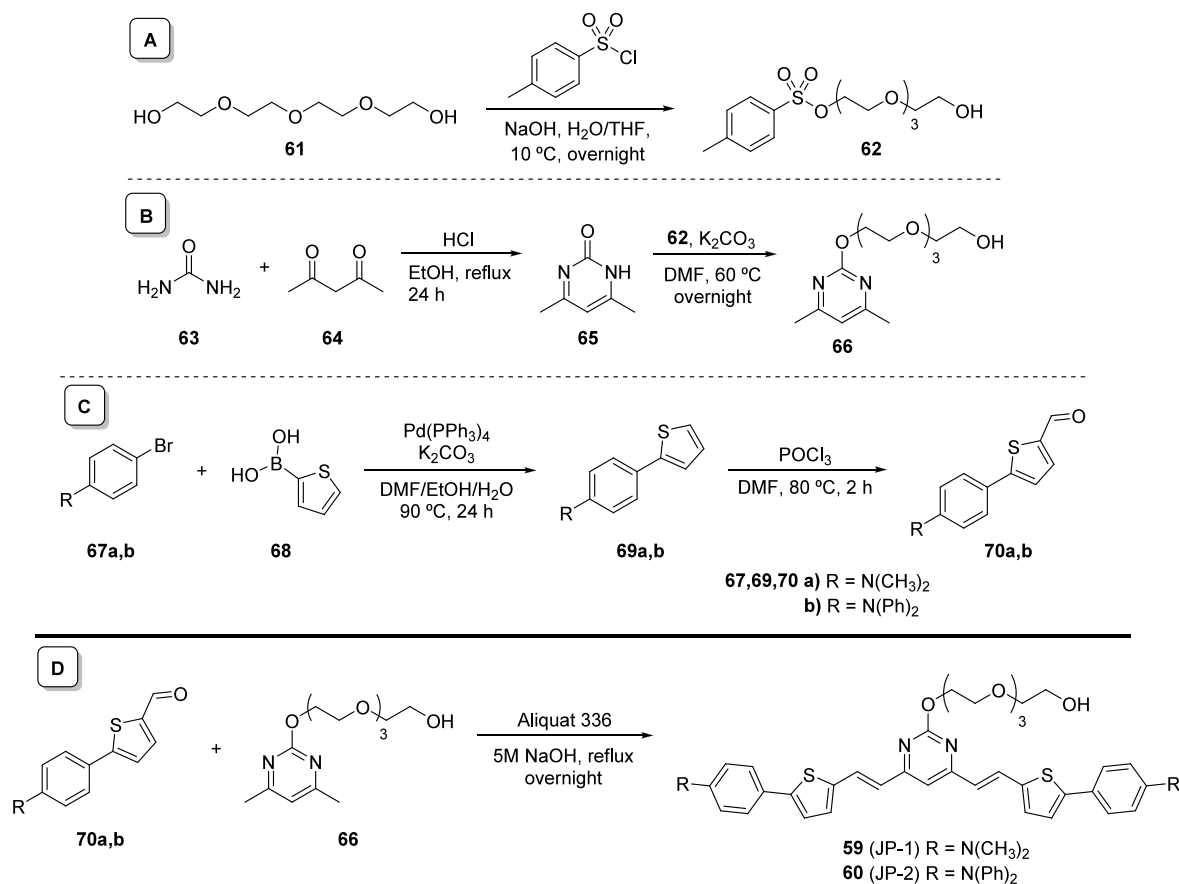


Figure 43. Framework combination design of compound 71 (LS-4) with a multifunctional framework encompassing an Aβ binding hydrophobic moiety, a hydrophilic and metal chelating unit, and a ROS targeting fragment.

imaging of Aβ species *ex vivo* and *in vivo* in the brain of an AD mouse model.⁸⁸

Concerning the magnetic resonance properties of dyad 44 *in vivo*, it was shown that postinjected images are brighter at different depths of the brain than the preinjected images, in sharp contrast to those from the WT mice, prompting the use of dyad 44 as new T₁-weighted MRI contrast agent (Figure 31C). In addition to the multimodal imaging properties of dyad 44, the ThT fluorescence assay allowed the establishment of an IC₅₀ value of 2.83 μM for the Aβ self-aggregation inhibition, suggesting its further potential as therapeutic agent in AD.

Furthermore, dyad 44 showed a considerable neuroprotective effect in SH-SY5Y cells, as well as a decreasing effect in the ROS production induced by various Aβ_{1–42} species.⁸⁸

As for the synthesis of dyad 44, the process was similar to that for previous cyanine theranostics regarding its fluorescent unit. The distinct synthetic approach in this particular case employed copper(I)-catalyzed azide–alkyne cycloaddition to link the Gd(DOTA) complex. In more detail, the authors started with the alkylation of lepidine 21 using 1-azido-4-bromobutane, followed by condensation with formyl carbazole 33, completing the fluorescent unit 46 (Scheme 10). Then, the cycloaddition

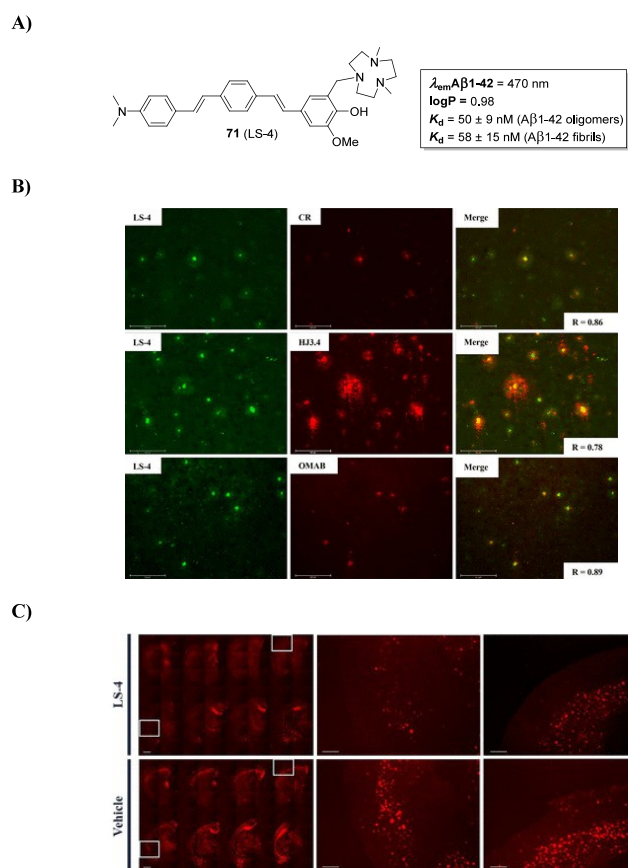


Figure 44. Staining profile and antiaggregation properties of compound 71 (LS-4 in the original article) evaluated using 5xFAD mice. (A) *In vitro* A β binding profile. (B) *In vivo* costaining assays. (C) *In vivo* amyloid pathology. Reprinted in part with permission from ref 100. Copyright 2021 American Chemical Society.

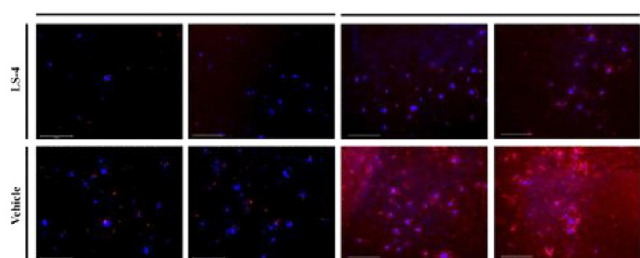


Figure 45. Representative fluorescence microscopy images of the CF594-AT8 and CF594-Iba1 immunostained brain sections from 5xFAD mice treated with compound 71 (LS-4) and vehicle. Reprinted in part with permission from ref 100. Copyright 2021 American Chemical Society.

reaction between intermediate **46** and Gd(DOTA)-alkyne **47** allowed the linkage of the two units, completing the synthesis of dyad **44** (Scheme 10). It is worth mentioning that the counteranion was exchanged to trifluoroacetate during the column chromatography, as 0.1% of trifluoroacetic acid was employed in the eluent.

Photodynamic therapy (PDT) has been emerging as an alternative tool to modulate proteinopathies, including A β aggregation, resorting to singlet oxygen ($^1\text{O}_2$) as the main substance for the photo-oxygenation.^{89,90} The photo-oxygenation of A β presents some interesting advantages, such as its less

invasive approach, spatiotemporal controllability, and high selectivity.⁹¹ This method can decrease the A β aggregation process under physiological conditions, since the covalent introduction of hydrophilic oxygen atoms into amyloid proteins disrupts their amyloidogenic properties.⁹¹ However, this kind of antiaggregation strategy also has its own issues, such as the low penetration depth of excitation light into the skull and brain and the off-target oxidative damage promoted by the photosensitizers. Attempting to deal with these pitfalls, in 2022, an investigation by Yan et al. reported a series of “off-on” D- π -A photosensitizers based on the quinoline scaffold that, following a target-sensing catalyst activation (TaSCAc) approach, were expected to decrease the oxygen production at the off-target tissues (Figure 32).⁹² The authors used the well-studied quinolinium moiety (donor group present in many theranostics described so far) as the acceptor group, which was bridged with a dimethylaniline group as the acceptor and A β recognition group, and screened the optimal length of the π -bridge to produce compounds **48–50** (Figure 32).⁹²

As expected, extending the π -bridge resulted in the red-shift of the excitation and emission wavelengths, with compound **50** (Figure 32) presenting the most interesting values ($\lambda_{\text{abs}} = 620$ nm; $\lambda_{\text{em}} = 812$ nm).⁹² All the compounds in this series showed selectivity toward A β aggregates over oligomers and monomers, exhibiting turn-on emission upon binding A β aggregates. This was attributed to the compound's intramolecular rotation inhibition upon binding aggregates, which was later verified in a high-viscosity environment. Among the series, compound **49** presented the best detection performance, with quantum yields alone and with A β aggregates of 0.37% and 35%, respectively (95-fold enhancement upon binding).⁹² Compounds **48–50** also showed good performance in staining A β aggregates in slices of the cortex from APP/PS1 mice (C57BL/6, 13-month-old, male) and good colocalization with ThS, although with a lower background, suggesting that compounds **48–50** exhibit a longer emission wavelength and have a better S/N ratio than ThS (Figure 33A). The staining performance of compounds **48–50** was further confirmed toward A β fibers using ThT as a positive control, in which the red fluorescence signals overlap the ThT green fluorescence, suggesting a high selectivity toward A β fibrils (Figure 33, B).⁹²

The ability of compounds **48–50** to generate $^1\text{O}_2$ was further assessed and confirmed both theoretically and experimentally while showing very low biological toxicity in SH-SY5Y cells, up to 50 μM . Since compound **49** (Figure 34A) exhibited the most promising panorama in mapping A β aggregation and the capacity to generate singlet oxygen, it was selected for further studies, namely the phototriggered suppression and disintegration of A β aggregates (Figure 34B and C).⁹²

Upon irradiation (532 nm), the A β peptide did not show a significant length increase, suggesting that compound **49** effectively inhibited the A β self-aggregation by photo-oxygenation (Figure 34B). The A β monomer molecular weight before and after the incubation with compound **49** showed regular increments of 16, 32, and 48 Da, suggesting that some amino acids were indeed oxidized. Compound **49** was further able to degrade preformed A β aggregates via photo-oxygenation (Figure 34C), suggesting a strong binding capacity and photo-oxygenation toward A β species. This promising result was further confirmed in PC12 cells, in which compound **49** reduced the A β -induced neurotoxicity.⁹²

The lead compound **49** was synthesized in three reaction steps, starting with the preparation of quinoline **52** through

Scheme 14. Four-Step Synthetic Route for the Preparation of Compound 71 (LS-4)

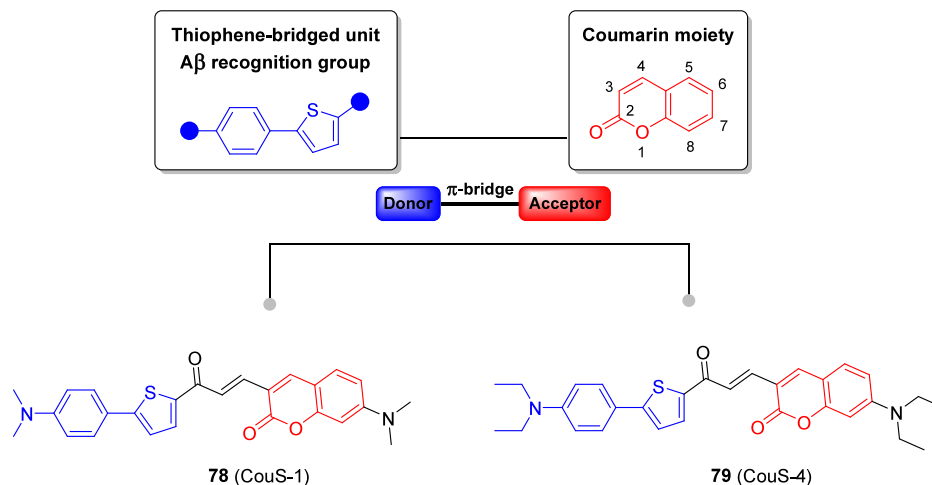
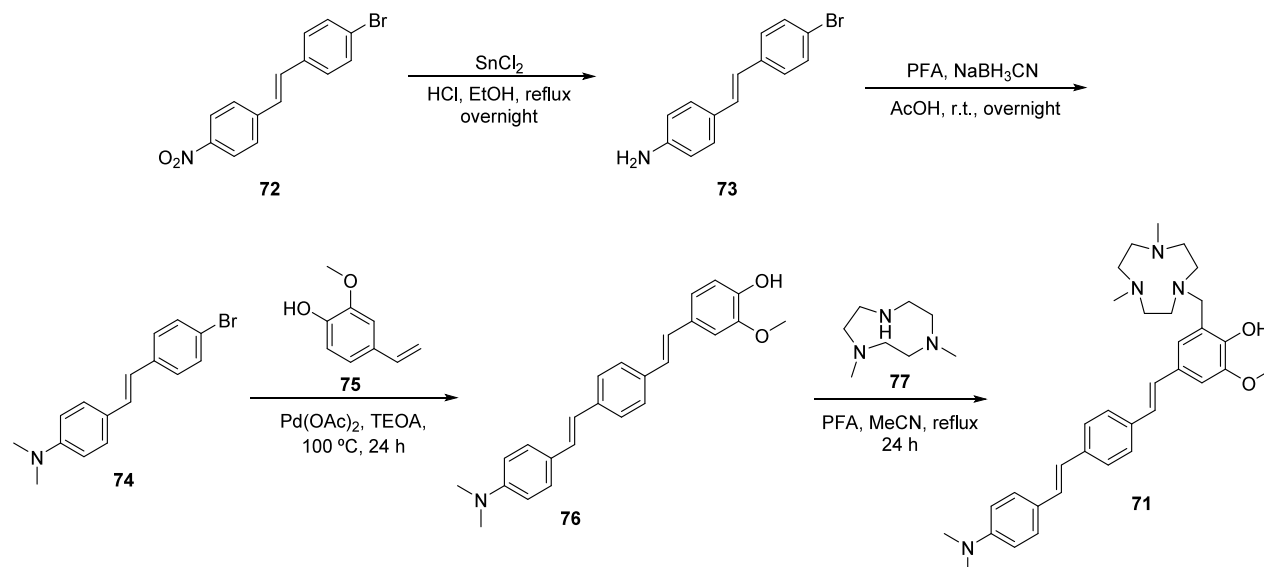


Figure 46. Structural design of Coumarin-based imaging probes 78 (CouS-1) and 79 (CouS-4).

Doebner–Miller reaction and subsequent *N*-methylation to achieve quinolinium moiety 53 (Scheme 11). Then, the condensation reaction between the quinolinium 53 and cinnamaldehyde 54 completes the D- π -A architecture of compound 49 (Scheme 11).

Curcumin-Based Theranostics. Thioflavin derivatives, *i.e.*, ThT or ThS, are considered the gold-standard dyes for the *in vitro* histological staining of amyloid fibrils.^{25,93,94} Although these dyes are commercially available at low costs, they have important drawbacks such as (i) distorted signals from enrichment quenching effect on fluorescence, (ii) inevitable noises from always-on pattern, and (iii) limited BBB permeability, hindering their translation into *in vivo* applications. A plausible alternative strategy to the use of molecular rotors such as ThT and ThS to label amyloid fibrillation processes is the use of aggregation-induced emission (AIE) fluorophores, which usually show a light-up feature associated with binding events during the aggregation process, strong photostability, and excellent biocompatibility.^{95,96} Among the existing AIE fluorophores, curcumin has noteworthy potential for both imaging and inhibition of A β aggregation.⁹⁷ Aiming to mitigate

the aggregation-caused quenching (ACQ) effects of a large portion of curcumin derivatives, Tang and co-workers endeavored to develop a novel multifunctional AIE-curcumin derivative for light-up detection of A β fibrils and plaques, inhibition of A β fibrillation, and disassembly of preformed A β fibrils.⁹⁸ To do so, the authors focused on the central dicarbonyl moiety of curcumin 55 (Figure 35, gray inset), designing two new boron-complex analogues, Cur-O-BF₂ 56 assembled by direct complexation of curcumin 55 with BF₃·Et₂O and Cur-N-BF₂ 57, which required the imine replacement preceding the boron complexation (Figure 35).

Despite the appealing D-A-D structure of both fluorophores, their emission wavelengths in solid state were not very different from those of the previous theranostics examined in this Review. In fact, the Cur-N-BF₂ 57 showed a maximum emission wavelength at 572 nm ($\phi = 14.0\%$), while the Cur-O-BF₂ 56 revealed a more interesting emission wavelength of 655 nm, although with a much lower quantum yield ($\phi = 1.2\%$). In opposition, the cytotoxicity of Cur-N-BF₂ 57 ($\sim 100\%$ cell viability) was nonexistent, while its oxygen analogue 56 showed only 37.8% cell viability at 20 μ M in mouse hippocampal

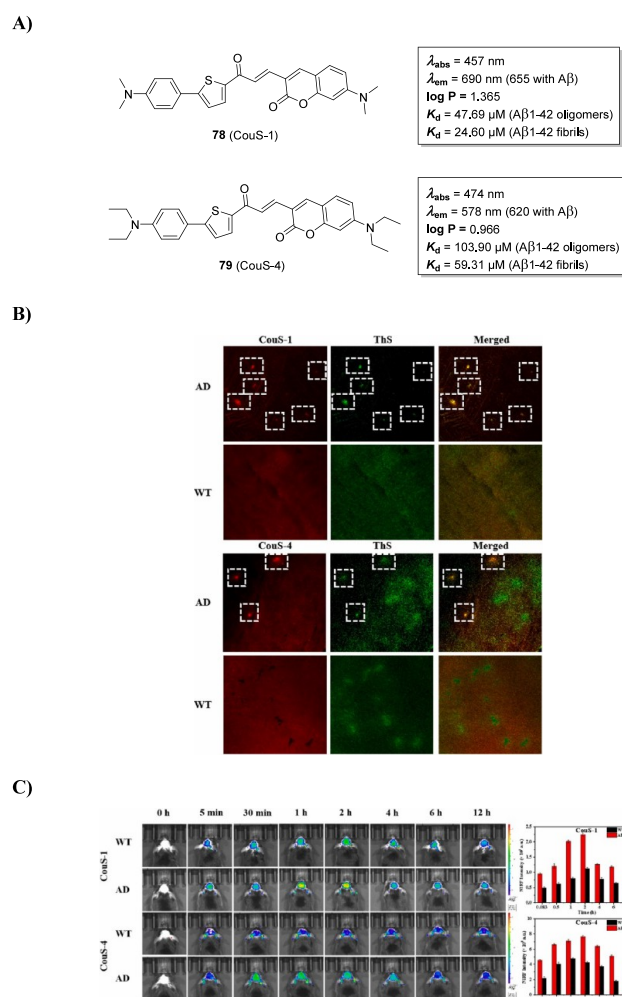


Figure 47. Imaging profile of theranostics 78 and 79 (CouS-1 and CouS-4, respectively, in the original article). (A) *In vitro* binding profile. (B) Co-staining studies with wild-type mice (WT) and APP/PS1 transgenic mice (AD). (C) *In vivo* A β deposition profiles in AD mice (C57BL6, APP/PS1, 4 months old, male) and wild-type mice (C57BL6, 4 months old, male). Reprinted in part with permission from ref 102. Copyright 2023 Elsevier.

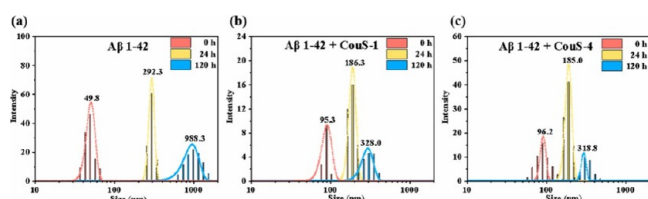


Figure 48. DLS measurement of the fibrillation process of A β (5 μM). (a) A β alone, (b) A β and 78 (CouS-1), and (c) A β and 79 (CouS-4) (10 μM). Reprinted in part with permission from ref 102. Copyright 2023 Elsevier.

neuronal cells (HT22 cells). The low toxicity of Cur-N-BF₂ 57 was further confirmed in human neuroblastoma SH-SY5Y cells and rat pheochromocytoma PC12 cells, which showed nearly 100% viability at 20 μM . Therefore, the authors focused their attention on Cur-N-BF₂ 57 to move further to *in vitro* A β ₁₋₄₂ fibril detection studies, using also curcumin 55 and ThT for comparison purposes.

The results revealed a fluorescence enhancement of Cur-N-BF₂ 57 upon incubation with A β ₁₋₄₂ species, especially for

longer incubation times, which indicates a higher binding affinity for A β ₁₋₄₂ fibrils rather than smaller species (oligomers and monomers). The authors assumed that such enhancement is due to Cur-N-BF₂ 57 binding within hydrophobic domains of A β ₁₋₄₂ fibrils, restricting the intramolecular motion and inhibiting the twisted intramolecular charge transfer (TICT) effect.⁹⁸ The authors also verified that Cur-N-BF₂ 57 presented a better light-up detection ability even at higher concentrations (up to 4.0 mM), while curcumin 55 and ThT suffered from self-quenching effects at concentrations above 0.05 and 0.25 mM, respectively. The selective staining profile of Cur-N-BF₂ 57 was also demonstrated in brain slices from APPswe/PSEN 1dE9 transgenic mice (APP/PS1), where A β plaques were clearly identified on the hippocampus and cerebral cortex with a high signal-to-noise ratio, and with overlap coefficients of 0.93 and 0.89, respectively, upon costaining with A β antibody (Figure 37).⁹⁸

Unfortunately, the binding affinity of Cur-N-BF₂ 57 toward A β species, by means of its K_d , was not assessed by the authors, which would be quite useful for some sort of ranking comparison with other reported theranostics in this Review.

Likewise, the inhibition ability of Cur-N-BF₂ 57 toward A β fibrillation as well as its capacity to disassemble of A β fibrils was only evaluated qualitatively. The standard ThT fluorescence assay was employed, and the experimental outcomes showed a 3-fold lower light-up ratio in the presence of Cur-N-BF₂ 57 (A β peptide/Cur-N-BF₂ 57 ratio 2:1), in opposition to a 22-fold ThT fluorescent enhancement in the absence of Cur-N-BF₂ 57. Furthermore, the ThT fluorescence intensity also decreased after the addition of Cur-N-BF₂ 57 into the A β ₁₋₄₂ fibril solution, which is an indication of the disassembly of preformed aggregates upon incubation with Cur-N-BF₂ 57 (Figure 38). An additional neuroprotective effect of Cur-N-BF₂ 57 against A β fibril-induced toxicity was also observed in HT22 model cell line, shown by the cells recovering their normal morphology and also cell viability increasing to 83.2%.⁹⁸

The synthetic approach of Cur-N-BF₂ 57 is perhaps the simplest one of all the others described theranostics in this review. It involved only two very simple reaction steps, *i.e.*, the replacement of a carbonyl group from curcumin 55 with an enamine moiety to obtain intermediate 58 upon reaction with ammonium formate (Scheme 12), followed by complexation with BF₃·Et₂O to provide the Cur-N-BF₂ 57 theranostic molecule (Scheme 12).

Subsequent publications on modified curcuminoids for theranostic purposes have been reported. In 2021, Pan et al proposed additional theranostics to the chemical space already covered, based on both the modification of the central unit of curcumin and its side moieties (Figure 39).⁹⁹ The authors designed two curcumin surrogates 59 and 60 (Figure 39), which were based on the replacement of the curcumin dicarbonyl moiety with a pyrimidine unit having a solubility-enhancing substituent (Figure 39). Additionally, both sides of curcumin were modified with thiophene heterocycles as well as with different EDGs to modulate photophysical and A β recognition properties (Figure 39).

The study of the photophysical properties showed that compounds 59 and 60 exhibited absorption wavelengths of 475 and 455 nm, emission wavelengths of 678 and 648 nm, and quantum yields of 0.14 and 0.65, respectively.⁹⁹ The replacement of the curcumin's diketone moiety with a pyrimidine indeed enhanced the stability of compounds 59 and 60, which remained in more than 80%, when compared to

Scheme 15. Convergent Synthesis of Theranostics 78 (CouS-1) and 79 (CouS-4)

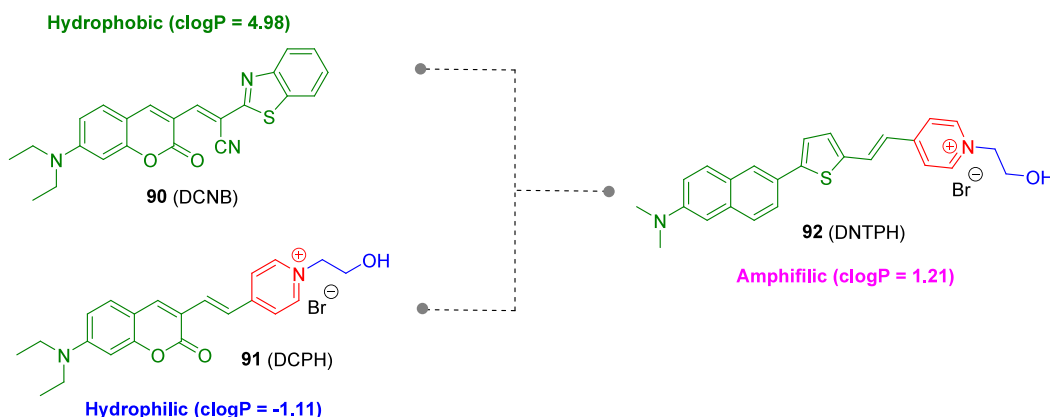
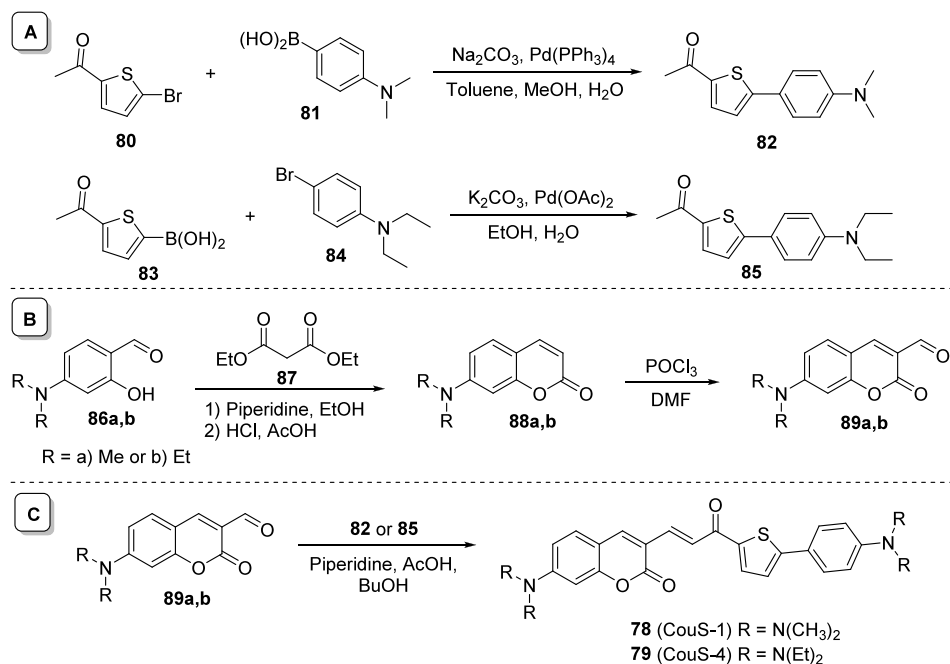
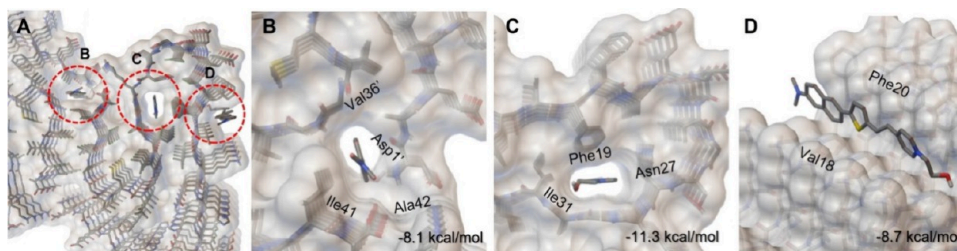


Figure 49. Design strategy toward the amphiphilic theranostic 92 (DNTPH).

Figure 50. Top view of two consecutive Aβ₄₂ fibrils. (A) Three protein–ligand binding sites on the surface and the internal tunnel in Aβ₄₂ fibrils. (B) Protein–ligand interactions on the Asp1', Val36', Ile41, and Ala42 surface between two Aβ₄₂ fibrillar chains. (C) Top view of 92 (DNTPH) encapsulated by the Phe19, Asn27, and Ile31 internal tunnel in Aβ₄₂ fibrils. (D) Clipped view of 92 (DNTPH) within the Aβ₄₂ fibril groove defined by Val18 and Phe20. Reprinted in part with permission from ref 103. Copyright 2023 Wiley-VCH GmbH.

the curcumin, which only remained in 20%.⁹⁹ The K_d values of compounds 59 and 60 toward Aβ_{1–42} oligomers and fibrils were determined as 0.264 and 0.218 μM and 0.312 and 0.430 μM, respectively. This means that compound 59 was not selective to any Aβ_{1–42} species, while compound 60 was only slightly selective for oligomers over fibrils. Such lack of selectivity can be explained by the similarity of the predicted binding modes of

compounds 59 and 60 toward Aβ oligomers, which are mainly based on hydrogen bonding between the ethoxy groups and the –NH group of Phe20 and π–π stacking interactions between the pyrimidine moieties and the benzene rings of three Phe19 residues (Figure 40).⁹⁹ The binding energies of compounds 59 and 60, –48.4178 and –52.0811 kJ/mol, respectively, showed

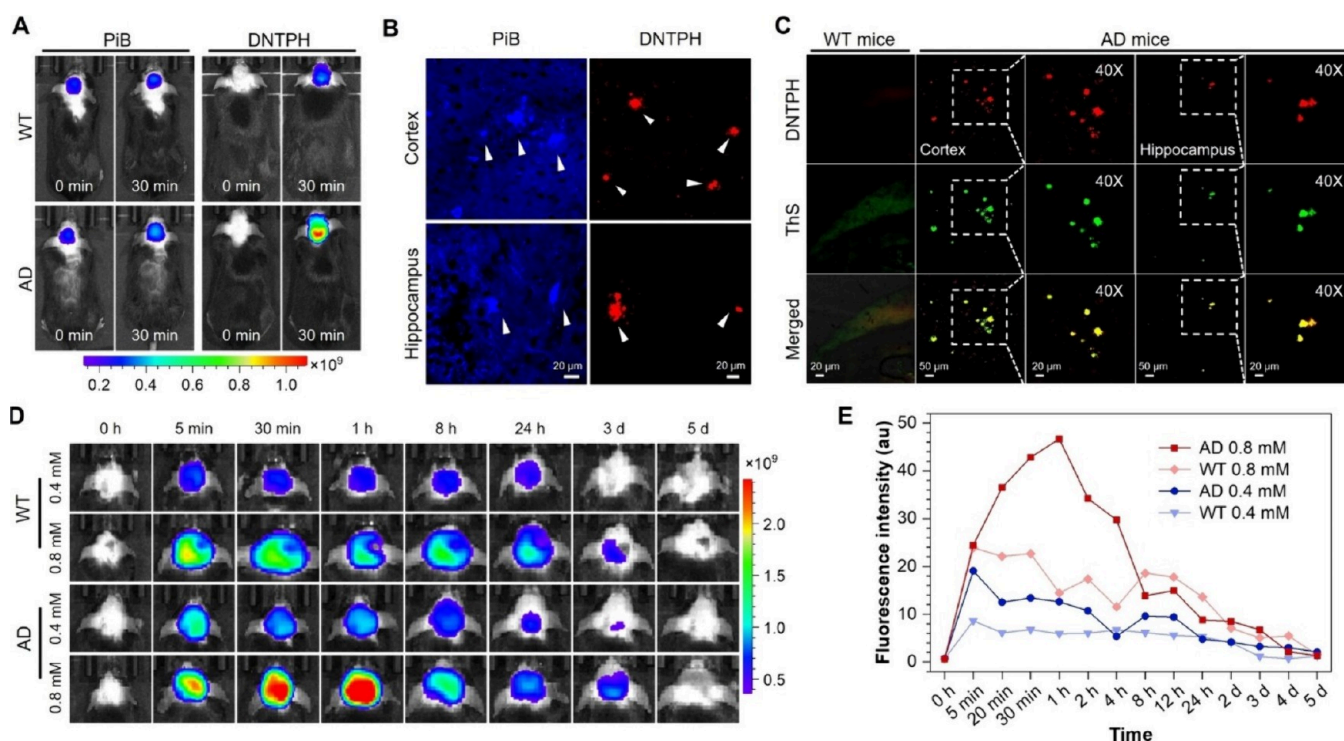


Figure 51. *In vivo* imaging of $A\beta_{42}$ deposition in 7-month-old APP/PS1 transgenic mice. (A) Comparison of the fluorescence images of the brain at 30 min after intravenous injection of 0.4 mM PiB or 92 (DNTPH) to wild-type (WT) mice and AD mice. (B) *Ex vivo* fluorescence imaging of brain slices removed from AD mice at 2 h post intravenous injection of PiB and 92 (DNTPH) (0.4 mM). (C) *Ex vivo* fluorescence imaging of brain slices removed from WT and AD mice after intravenous injection of 92 (DNTPH). (D) *In vivo* imaging of 7-month-old WT and AD mouse brain areas at different times after intravenous injection of 0.4 or 0.8 mM 92 (DNTPH). (E) The NIR fluorescence as a function of time after intravenous administration of 0.4 or 0.8 mM 92 (DNTPH) in WT and AD mice. Reprinted in part with permission from ref 103. Copyright 2023 Wiley-VCH GmbH.

that the latter might have a slightly stronger affinity toward the $A\beta$ oligomer than compound 59.⁹⁹

Although both compounds 59 and 60 present similar properties, in our opinion compound 60 should be considered as the lead, since it has slightly better selectivity (Figure 41A). The *in vitro* imaging performance of compound 60 showed good colocalization with the standard ThS (Figure 41B), while the *in vivo* imaging studies using APP/PS1 transgenic mice (C57BL6, APP/PS1, 5-month-old, male) as the AD model also revealed the good performance of compound 60 after 12 h of injection (Figure 41C).

Regarding the $A\beta$ aggregation inhibition performance of compound 60, it was observed by TEM images that the amount and length of $A\beta_{1-42}$ fibrils decreased in the presence of compound 60, in opposition to the control experiments with $A\beta$ alone and with ThS, which did not show a significant inhibition effect (Figure 42).

The synthesis of theranostics 59 and 60 follows a convergent strategy, where two components 66 and 70 were previously prepared (Scheme 13D). The building block 66 was prepared in two steps, starting with the synthesis of 4,6-dimethylpyrimidin-2-one 65 in acidic media, followed by K_2CO_3 -promoted alkylation using compound 62 as the alkylation agent (Scheme 13A and 13B). The second building block 70 was also obtained in two steps: Suzuki coupling of aryl bromides 67 and boronic acid 68, followed by Vilsmeier–Haack formylation of thiophenes 69 (Scheme 13C). The convergent synthesis was completed through base-promoted condensation reaction between thiophene 70 and dimethylpyrimidine 66 (Scheme 13D).

Distyrylbenzene-Based Theranostics. Most of the theranostics described so far are designed to have hydrophobic π -conjugated aromatic systems aimed at interacting with hydrophobic residues in the β -sheet cores of the amyloid fibrils through hydrophobic interactions. Most of the compounds have micromolar affinity for amyloid species, and very few examples reach nanomolar affinities. On the other hand, the development of multifunctional theranostics, *i.e.*, compounds capable to perform imaging and therapy with the bonus of targeting other AD pathologies (e.g., as metal ion dishomeostasis, ROS formation, neuroinflammation, and acetylcholinesterase inhibition) could have great potential in the development of effective AD therapies. In attempting to cover all these requirements, Mirica et al. generated an amphiphilic compound 71, LS-4 in the original paper (Figure 43), by linking a hydrophobic amyloid fibril-binding fragment with a hydrophilic metal-chelating azamacrocyclic, which was intended to increase the binding affinity toward $A\beta$ peptide aggregates.¹⁰⁰ The choice of the hydrophobic fragment was based on the structural similarity with the FDA-approved PET imaging agent [^{18}F]florbetaben (blue inset), combined with the amyloid fluorescent dye DF-9 (green inset) (Figure 43). The overall structure of 71 (LS-4) was further tailored with the introduction of the 2-methoxy-phenol fragment (*o*-vanillin patch) and 2,4-dimethyl-1,4,7-triazacyclononane as the metal-chelating hydrophilic moiety (Figure 43).

Although the authors didn't mention anything about the native fluorescent profile of 71 and the so-called pre-LS-4 (without the hydrophilic moiety) in organic solvents and/or in PBS, we might infer from the fluorescence $A\beta$ binding experiments that the two compounds have emission wavelengths around 525 and 470 nm, respectively. In addition, the

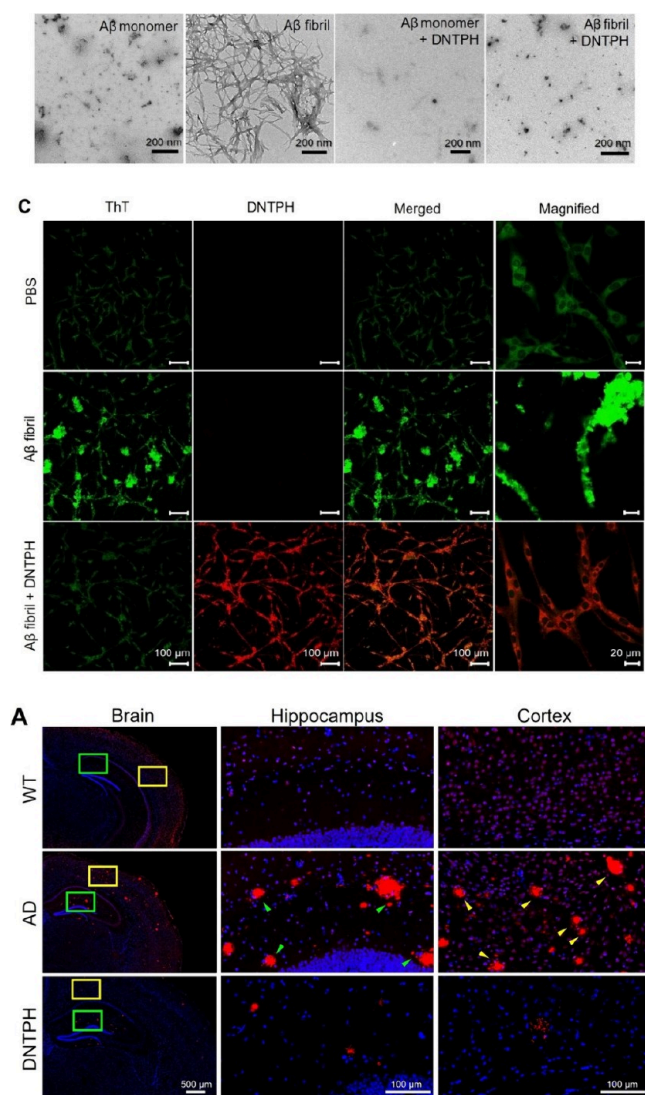


Figure 52. Fibrosis inhibition and fibril disassembly by compound **92** (DNTPH). (A) TEM images of Aβ₄₂ monomer and Aβ₄₂ fibril grown with or without **92** (DNTPH). (B) Confocal images of PC-12 cells treated with PBS, Aβ₄₂ fibrils, or **92** (DNTPH) mixed with Aβ₄₂ fibrils for 48 h and stained with ThT. (C) Immunofluorescence staining of Aβ₄₂ plaques (red) of brain slices of WT mice, AD mice, and **92** (DNTPH)-treated AD mice. Reprinted in part with permission from ref 103. Copyright 2023 Wiley-VCH GmbH.

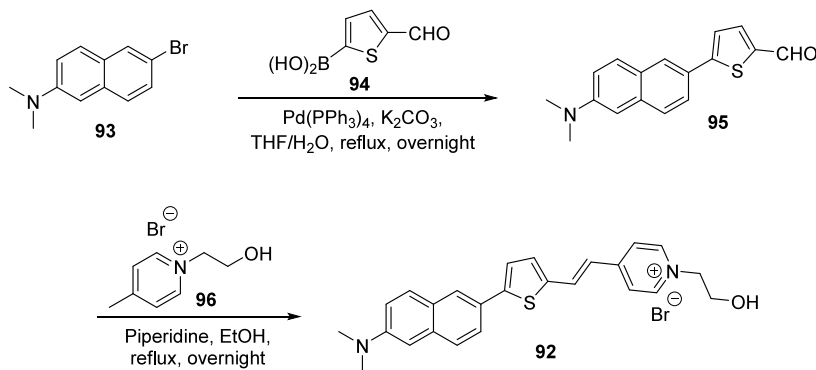
compound **71** experienced a blue-shift in emission and a 50-fold fluorescence intensity enhancement upon binding Aβ_{1–42} oligomers. In the case of Aβ_{1–42} fibrils, the fluorescence enhancement was only 20-fold, and no emission wavelength shift was observed. In the absence of the hydrophilic moiety (**pre-LS-4**), no significant variation on the fluorescence intensity was observed, indicating the important role of the aza-macrocycle in the fluorescent enhancement upon binding soluble Aβ_{1–42} oligomers. The binding affinity of both **71** and **pre-LS-4** was further assessed by means of their K_d values toward Aβ species. Compound **71** showed nanomolar affinity for Aβ_{1–42} oligomers ($K_d = 50 \pm 9$ nM) and fibrils ($K_d = 58 \pm 15$ nM). Again, in the absence of the hydrophilic unit, the K_d values increase to 9–10 μM, strengthening the theory behind the essential role of the aza-macrocycle in binding to the Aβ_{1–42} species (Figure 44A).¹⁰⁰ The ability of **71** to detect Aβ_{1–42} species was assayed in fluorescence staining assays of 5xFAD mouse brain sections using Congo red or specific and nonspecific antibodies (Aβ oligomer-specific monoclonal antibody (OMAB) and HJ3.4 antibody). Indeed, **71** showed excellent colocalization with the immunofluorescence of OMAB ($R = 0.89$), higher than the that for the brain sections immunostained with HJ3.4 ($R = 0.78$), demonstrating good capacity for probing Aβ oligomers and fibrils in AD brain sections (Figure 44B). The immunostaining studies with **pre-LS-4** revealed much lower colocalization with the HJ3.4 antibody, which is consistent with the *in vitro* findings.¹⁰⁰

Compound **71** was further demonstrated to be able to rescue the viability of N2a cells and relieve the neurotoxicity of Cu²⁺-Aβ₄₂ species. Compound **71** also showed further *in vivo* therapeutic efficacy by reducing the HJ3.4-labeled amyloid aggregates up to 60% (Figure 44C). Last but not least, compound **71** (LS-4) significantly decreased by 47% the number of p-tau aggregates surrounding the amyloid plaques in 5xFAD mice (Figure 45).¹⁰⁰

The synthesis of multifunctional theranostic **71** (LS-4) involves four sequential reaction steps (Scheme 14). First, the nitro group of styrylbenzene **72** was reduced to the corresponding amine with SnCl₂, followed by reductive N-methylation with paraformaldehyde (PFA) of the resulting intermediate **73**, resulting in compound **74** (Scheme 14). Then, the 2-methoxy-4-vinylphenol **75** was installed through Heck reaction to afford intermediate **76** (the so-called **pre-LS-4**), which upon Mannich reaction with PFA and Me₂HTACN produced the desired compound **71** (Scheme 14).¹⁰⁰

Coumarin-Based Theranostics. Coumarins, also known as benzopyran-2-ones, have a large range of biological applications

Scheme 16. Synthesis of Theranostic Compound **92** (DNTPH)



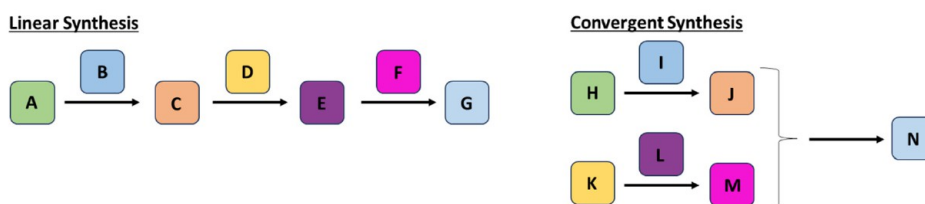


Figure 53. Schematic depiction of linear and convergent synthesis.

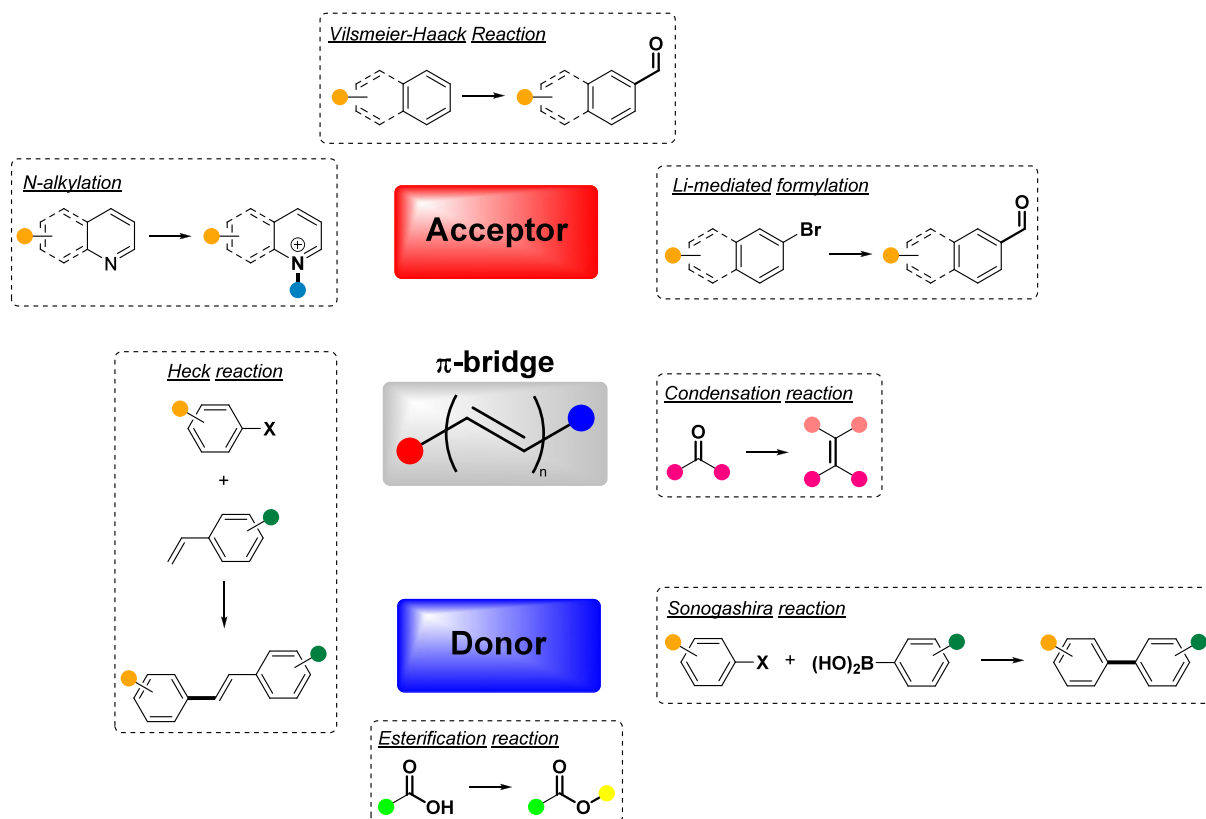


Figure 54. Reaction mapping of common transformations to prepare theranostics.

due to their straightforward synthesis, biological significance, and low toxicity. The basic structure of this molecule displays no fluorescence. However, its fluorescence can be greatly increased by introducing EDGs at the 6- or 7-position and EWGs at the 3- or 4-position, which promotes the push–pull electron system within the coumarin's structure.¹⁰¹ Based on the D- π -A architecture, Pan et al. designed two novel fluorescence imaging probes for A β , compounds **78** and **79** (CouS-1 and CouS-4, respectively, in the original paper) (Figure 46).¹⁰² These two amphiphilic probes contain a lipophilic conjugated thiophene-bridged unit as the EDG and A β recognition group, an amino-modified benzofuran group as the EWG, and a vinyl moiety between both groups to extend the conjugated system (Figure 46).

Regarding the native photophysical properties, compounds **78** and **79** exhibited absorption wavelengths at 457 and 474 nm and emission wavelengths at 690 and 578 nm, respectively; compound **79** exhibited a quantum yield of 0.748, higher than that of compound **78** ($\phi = 0.057$). The fluorescence intensity of **79** was notably more stable than **78**, as it remained at about 80% after 24 h. The binding assays with A β_{1-42} oligomers and fibrils showed fluorescence intensity enhancements of 1.4- and 1.5-fold

for compound **78**, while compound **79** exhibited 2.1- and 2.2-fold enhancement, suggesting a small degree of selectivity for fibrils. The binding constants toward oligomers and fibrils for compounds **78** and **79** were 47.69 and 24.60 μM and 103.90 and 59.31 μM , respectively, suggesting the weaker affinity of compound **79** (Figure 47A). The cytotoxicity in HeLa (human cervical carcinoma cell line), PC12 (nerve cells line), and bEnd.3 cells (mouse brain microvascular endothelial cells line) showed that both compounds have a certain degree of toxicity at 20 μM , with only 70% of cells remaining viable. Despite the differences in affinity for A β fibrils, both compounds **78** and **79** showed similar capacity to stain fibrils *ex vivo* (Figure 47B). On the other hand, the *in vivo* experiments showed that compound **79** reaches a maximum fluorescence intensity at 2 h after injection, with good BBB permeability (Figure 47C).

The A β aggregation inhibition effects were very briefly addressed *in vitro* using dynamic light scattering (DLS). Compounds **78** and **79** were tested at 10 μM , and the results showed a decrease in the number and length of A β_{1-42} fibrils (Figure 48). The efficacy of both compounds for reducing aggregation *in vivo* remained unclear.

Table 1. Overview Chart of the Potential Theranostics Discussed in This Review^a

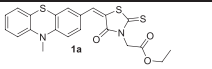
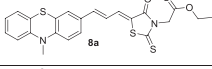
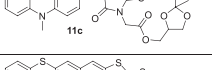
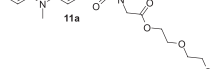
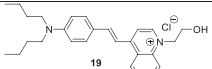
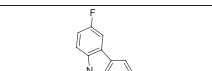
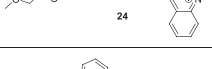
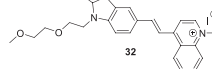
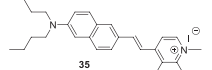
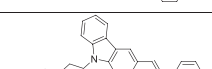
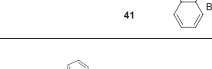
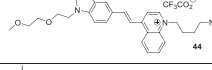
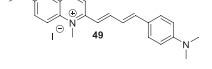
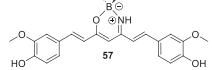
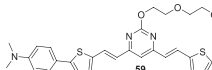
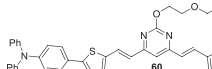
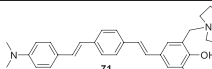
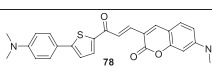
Compound	Emission		Fold	K_d (A β 1-42) (μ M)	Therapeutic activity IC ₅₀ (μ M)	Log <i>P</i>	Mouse type
	$\lambda_{em}^{[a]}$ (nm)	$\lambda_{em}^{[b]}$ (nm)					
	680	670	4.9	0.0075 \pm 0.0004	0.67 \pm 0.02	3.68	APPwsc/PSEN1
	700	680	13.0	0.0102 \pm 0.0011	1.8 \pm 0.1	ND	ND
	670	615	22.0	0.0245 \pm 0.0020	0.06	3.65	C57BL6,APPsw e/PSEN1
	670	610	63.9	0.0282 \pm 0.0020	0.4	3.03	C57BL/6,APP/PS1
	672	652	ND	13.12 ^[m] /5.66 ^[ol] /3.09 ^[l]	3.72	3.10	APP/PS1
	643	620	ND	3.22 ^[m] /0.66 ^[ol] /1.90 ^[l]	3.4	2.50 ^[e]	APP/PS1 5XFAD 3XTg-AD
	ND	676	ND	40.2 ^[m] /11.4 ^[l]	ND	2.59	APP/PS1
	615	680	51-126	280.8 ^[m] /127.6 ^[ol] /246.3 ^[l]	ND	3.44	5XFAD
	666	630	160-265	54.7 ^[m] /65.5 ^[ol] /25.6 ^[l]	ND	ND	5XFAD
	641	ND	ND	438.9 ^[m] /422.7 ^[ol] /309.2 ^[l]	2.83	ND	APP/PS1 5XFAD
	720	ND	95	ND	ND	ND	APP/PS1
	572	565	ND	ND	ND	ND	APPsw e/PSEN1 dE9
	678	670	3.2 ^[ol] /4.6 ^[l]	0.264 ^[ol] /0.218 ^[l]	ND	[e]	APP/PS1
	648	640	4.6 ^[ol] /5.5 ^[l]	0.312 ^[ol] /0.430 ^[l]	ND	[e]	APP/PS1
	530	470 ^[ol] /500 ^[l]	50 ^[ol] /20 ^[l]	0.050 \pm 0.009 ^[ol] / 0.058 \pm 0.015 ^[l]	ND	0.98 ^[e]	5x FAD
	690	655	1.4 ^[ol] /2.1 ^[l]	47.09 ^[ol] /24.60 ^[l]	ND	1.365	APP/PS1
	578	620	1.5 ^[ol] /2.2 ^[l]	103.90 ^[ol] /59.39 ^[l]	ND	0.966	APP/PS1
	708	710	18.1 ^[l]	0.146 ^[l]	0.19	1.21	APP/PS1

Table 1. continued

^aND, not defined; [a], maximum emission value without A β ; [b], maximum emission value with A β ; [c], values not precisely given; [d], mean of both emission values; [e], permeable *in vivo*, [m], monomers; [ol], oligomers; [f], fibrils.

Very much like many compounds described in this Review, theranostics **78** and **79** were prepared following a convergent synthetic strategy, where the two components (Scheme 15A and B) were coupled to achieve the desired D-A structure (Scheme 15C).

The thiophene components **82** and **85** were synthesized via Pd-catalyzed Suzuki-coupling using the respective aryl halides and boronic acids (Scheme 15A). The required 3-formylcoumarins **89a** and **89b** were prepared in two steps starting from the salicylaldehydes **86a** and **86b**, which were converted into the corresponding coumarins **88a** and **88b** through the reaction with diethylmalonate. Subsequent POCl₃/DMF formylation provided compounds **89a** and **89b** (Scheme 15, B). Finally, the thiophene and coumarin components were coupled through base-promoted condensation, completing the π -bridge of compounds **78** and **79** (Scheme 15C).

The coumarin-based theranostics sometimes suffer from very high hydrophobicity, limiting the interactions with A β . An appropriate balance between hydrophobic and hydrophilic interactions is often more suitable for optimizing binding, BBB permeability, and specificity for A β fibrils. To encompass these requirements, Tang and co-workers designed a theranostic probe based on coumarin surrogates, covalently installing an hydrophilic pyridinium moiety (Figure 49).¹⁰³

The target molecule was compound **92**, but nevertheless the authors also prepared compounds **90** and **91** as control molecules to get a SAR profile and mechanistic insights (Figure 49).

The native fluorescent profile of target compound **92** showed absorption and emission wavelengths of 510 and 708 nm, respectively. Upon binding with A β fibrils, the fluorescent intensity of compound **92** increased up to 18.1-fold, with a dissociation constant of 143 nM (6-fold higher binding affinity than ThT).¹⁰³ Such a high binding affinity was further rationalized by molecular docking, which predicted three major interaction locations in the fibrillar aggregate: (i) a first binding site relying on the groove between two entangled fibril axes, consisting of the side chains Asp1', Val36', Ile41, and Ala42 (Figure 50B); (ii) a tunnel along the fibril axis, where **92** interacts with Phe19, Asn27, and Ile31 residues (Figure 50C); and (iii) a groove along the fibril axis on the exposed surface adjacent to the hydrophobic residues of Val18 and Phe20 (Figure 50D).¹⁰³

The imaging performance of compound **92** was examined *in vivo* using 7-month-old APP/PS1 transgenic AD model mice (Figure 51). The overall imaging data showed that the mice treated with compound **92** have a higher S/N ratio than those treated with Pittsburgh-B (PiB), superior specificity through the costaining with thioflavin S, and effective metabolism after 7 days.¹⁰³

Regarding the therapeutic effects of compound **92**, it was verified that it has an evident positive impact the inhibition of A β 42 fibrosis by reducing granular oligomers with ~10 nm diameter and branched entangled fibrils to short and fragmented nanoaggregates (Figure 52A). Furthermore, both the *in vitro* and cell model ThT-monitored fibrillation assays demonstrated the high ability of **92** to reduce fibrillation with an IC₅₀ value of 0.19 μ M (Figure 52B). The theranostic compound **92** was further

demonstrated to have *in vivo* therapeutic potential, as it was capable of rescuing the cognitive impairments of 7-month-old WT and APP/PS1 mice with A β 42 plaque and severe AD-like phenotypes.¹⁰³ The authors further demonstrated a direct correlation between the cognitive improvements and the reduction of A β 42 plaques in both the cortex and hippocampal regions of compound **92**-treated mice (Figure 52C), as well as no observable damage to the heart, lung, liver, spleen, and kidney.¹⁰³

The synthesis of compound **92** was straightforward and was achieved in two reaction steps: (i) the Suzuki coupling of 6-bromonaphthalene **93** with boronic acid **94** to prepare intermediate **95** and (ii) the condensation between intermediate **95** and pyridinium **96** to give the target compound **92** (Scheme 16).¹⁰³

■ AMYLOID- β -BASED THERANOSTICS OVERVIEW

In Table 1, we summarize the main photochemical, binding, and antiaggregation properties of the compounds outlined in this Review regarding their potential application as theranostic agents against AD.

Regarding the imaging performance of the compounds and their potential application in patients with AD, the developed compounds are still far from clinic, as they have (i) limited penetration of NIR light across the thick skull-shielded brain in humans to reach the desired depth of penetration for imaging, (ii) multifaceted AD etiology, and (ii) complex brain morphology. The development of NIR-II-region theranostics should be envisioned, increasing the chances of clinical applications. Dual-targeted theranostics, hitting both A β and tau aggregation crosstalk, should be pursued in order to better understand the pathology and to develop disease-modifying therapies. In terms of binding affinity, several theranostics such as phenothiazines or coumarin analogues achieved nanomolar dissociation constants. However, the majority of the compounds have low or no selectivity for A β species (monomers, oligomers, and fibrils).

An appreciable therapeutic effect seems harder to achieve. The therapeutic outcomes of most of the theranostics were only evaluated *in vitro*, with IC₅₀ values ranging from 0.06 to 3.72 μ M. Usually, the therapeutic potential is not assessed *in vivo* using animal models, and only one theranostic effectively showed promising behavioral and cognitive results in a mouse model.

■ ANALYSIS OF THE SYNTHETIC METHODOLOGIES TO BUILD THERANOSTICS

The strategic and practical role of organic synthesis is critical for successfully discovering and developing new drugs. In the case of developing theranostic small molecules, the role of organic synthesis is even more relevant, as it accounts for the construction of specific architectures to meet the requirements of diagnostic and therapeutic tools. Several factors are often considered when deciding on which design route to pursue for the desired compounds. One of these factors is the convergence of the synthetic strategy in the preparation of the compounds. Convergent synthetic routes (Figure 53) played a major role in the development of the theranostics described in this review (7 synthetic routes are convergent out of 18 compounds analyzed)

(Schemes 1, 3, 6, 78, 13, and 15). Despite the advantages of convergent routes, linear strategies (Figure 53) are often necessary, also accounting for 7 examples in this Review (Schemes 5, 9–12, 14 and 1).

Regarding the reaction types employed in the described synthetic methodologies, condensations, the Vilsmeier–Haack reaction, BuLi-mediated formylation, the Wittig reaction, and *N*-alkylation are the most commonly employed reactions (Figure 54). Occasionally, Sonogashira, Heck coupling and esterification are also used, essentially to functionalize/decorate the donor or acceptor building blocks (Figure 54).

As clearly demonstrated throughout this Review, almost all the theranostics are built upon a D- π -A architecture. If we analyze the synthetic procedures and the reactions employed to achieve each component, *i.e.*, the donor, the π -bridge and the acceptor, we realize that the Vilsmeier–Haack reaction, BuLi-mediated formylation, and *N*-alkylation are the most frequent transformations to prepare the acceptor moiety (Figure 54). Regarding the π -bridge, condensation reactions with carbonyls are almost exclusive to install the required double bonds, but the Heck reaction was also employed once (Figure 54). Finally, the donor moiety is often functionalized through Heck and Sonogashira cross-coupling reactions, as well as classical esterification between carboxylic acids and alcohols (Figure 54). Sporadically, either Vilsmeier–Haack or BuLi-mediated formylation of the donor moiety is also necessary.

CONCLUSIONS

In the last few years, several examples of theranostics have been developed to combine diagnostic and therapeutic outcomes, aiming to change the current status quo of AD research and drug discovery. The integration of imaging and therapeutic tools in one single chemical entity has the potential to move clinical practice toward personalized medicine. In the past decade, the theranostic chemical space was enriched by means of scaffolds such as phenothiazine, cyanine, quinoline, curcumin and curcumin surrogates, styrylbenzenes, and coumarin and coumarin analogues, with some examples having great potential.

The design strategies are not well established, lacking critical insights into the geometry of the architectural scaffold and the binding pocket of the target macromolecules. With the ever increasing number of cryo-EM structures of A β and tau becoming available, it is now feasible to use computer-assisted design (CAD) for probe and theranostic development in a more rational approach.

This comprehensive analysis will encourage current research work to develop imaging probes together with therapeutic tools to provide effective diagnosis of AD, paving the way to personalized medicine. The successful development of optical theranostics that can assist early stage monitoring and serve as complementary tools in AD drug discovery can change the AD paradigm forever.

AUTHOR INFORMATION

Corresponding Author

Hélio M. T. Albuquerque – LAQV-REQUIMTE, Department of Chemistry, University of Aveiro, Campus de Santiago 3810-193 Aveiro, Portugal; orcid.org/0000-0001-5905-3316; Email: helio.albuquerque@ua.pt

Authors

Telmo N. Francisco – LAQV-REQUIMTE, Department of Chemistry, University of Aveiro, Campus de Santiago 3810-193 Aveiro, Portugal

Daniela Malafaia – LAQV-REQUIMTE, Department of Chemistry, University of Aveiro, Campus de Santiago 3810-193 Aveiro, Portugal

Lúcia Melo – LAQV-REQUIMTE, Department of Chemistry, University of Aveiro, Campus de Santiago 3810-193 Aveiro, Portugal

Artur M. S. Silva – LAQV-REQUIMTE, Department of Chemistry, University of Aveiro, Campus de Santiago 3810-193 Aveiro, Portugal; orcid.org/0000-0003-2861-8286

Complete contact information is available at:

<https://pubs.acs.org/10.1021/acsomega.3c10417>

Funding

This work received financial support from PT national funds (OE) through FCT/MCTES (Fundação para a Ciência e a Tecnologia and Ministério da Ciência, Tecnologia e Ensino Superior) within the projects LAQV-REQUIMTE (UIDB/50006/2020 and UIDP/50006/2020) and MuTaTher-AD: “Multi-target theranostics for Alzheimer’s disease” (2022.06064.PTDC) (<https://doi.org/10.54499/2022.06064.PTDC>).

Notes

The authors declare no competing financial interest.

ACKNOWLEDGMENTS

T.N.F., D.M., and L.M. thank FCT/MCTES (Fundação para a Ciência e Tecnologia and Ministério da Ciência, Tecnologia e Ensino Superior) and ESF (European Social Fund) through NORTE 2020 (Programa Operacional Região Norte) for their Ph.D. grants (2022.12243.BD, 2021.05641.BD, and 2023.02496.BD), respectively. H.A. acknowledges MuTaTher-AD (<https://doi.org/10.54499/2022.06064.PTDC>) for his researcher contract.

ABBREVIATIONS

AD	Alzheimer’s Disease
AChEI	Acetylcholinesterase Inhibitors
ACQ	Aggregation-Caused Quenching
AIE	Aggregation-Induced Emission
aza-BODIPYs	Aza-borondipyromethenes
A β	Amyloid- β
A β Os	A β Oligomers
BBB	Blood–Brain Barrier
BChE	Butyrylcholinesterase
BSA	Bovine Serum Albumin
CD	Circular Dichroism
CNS	Central Nervous System
CR	Congo Red
DFT	Density Functional Theory
DLS	Dynamic Light Scattering
DMF	Dimethylformamide
D- π -A	Donor- π -Acceptor
D- π -A- π -D	Donor- π -Acceptor- π -Donor
EDG	Electron Donating Group
EMA	European Medicines Agency
EWG	Electron Withdrawing Group
FDA	Food and Drug Administration
LMICs	Low-Income and Middle-Income Countries

MRI	Magnetic Resonance Imaging
NBS	N-Bromosuccinimide
NFTs	Neurofibrillary Tangles
NIRF	Near-Infrared Fluorescent
NMDA	N-Methyl-D-aspartic Acid
OMAB	Oligomer-specific Monoclonal Antibody
PAMPA	Parallel Artificial Membrane Permeability Assay
PAS	Peripheral Active Site
PDT	Photodynamic therapy
PET	Positron Emission Tomography
PFA	Paraformaldehyde
ROS	Reactive Oxygen Species
SOC	Spin–Orbit Coupling
SOSG	Singlet Oxygen Sensor Green
SPECT	Single-Photon Emission Computed Tomography
TaSCAc	Target-Sensing Catalyst Activation
TEM	Transmission Electron Microscopy
Tg	Transgenic
ThS	Thioflavin S
ThT	Thioflavin T
TICT	Twisted Intramolecular Charge Transfer
TIRFM	Total Internal Reflection Fluorescence Microscope
TSE	Transmissible Spongiform Encephalopathies
WT	Wild-Type
ΔE_{ST}	Singlet–Triplet Energy Gap

■ ADDITIONAL NOTE

^aThe structure of Eth-BF is incorrectly drawn in the original paper (ref 46). According to the characterization data provided by the authors, we believe that the correct structure is the one in Figure 6.

■ REFERENCES

- (1) Feigin, V. L.; Vos, T.; Nichols, E.; Owolabi, M. O.; Carroll, W. M.; Dichgans, M.; Deuschl, G.; Parmar, P.; Brainin, M.; Murray, C. The global burden of neurological disorders: translating evidence into policy. *Lancet Neurol.* **2020**, *19* (3), 255–265.
- (2) Ropper, A. H.; Samuels, M. A.; Klein, J. P. *Adams and Victor's Principles of Neurology*, 10 ed.; McGraw-Hill Education Medical: New York, NY, 2014.
- (3) *Handbook of Clinical Neuropsychology*, 2nd ed.; Gurd, J. M., Kischka, U., Marshall, J. C., Eds.; Oxford University Press: Oxford, UK, 2012.
- (4) Viña, J.; Lloret, A. Why Women Have More Alzheimer's Disease Than Men: Gender and Mitochondrial Toxicity of Amyloid- β Peptide. *J. Alzheimers Dis.* **2010**, *20*, S527–S533.
- (5) Scheltens, P.; De Strooper, B.; Kivipelto, M.; Holstege, H.; Chételat, G.; Teunissen, C. E.; Cummings, J.; van der Flier, W. M. Alzheimer's disease. *Lancet (London, England)* **2021**, *397* (10284), 1577–1590.
- (6) Kasper, D. L.; Fauci, A. S.; Hauser, S. L.; Longo, D. L.; Jameson, J. L.; Loscalzo, J. *Harrison's Principles of Internal Medicine*, 19th ed.; McGraw-Hill Professional Publishing: Blacklick, NY, 2015.
- (7) Gustavsson, A.; Norton, N.; Fast, T.; Frölich, L.; Georges, J.; Holzapfel, D.; Kirabali, T.; Krolak-Salmon, P.; Rossini, P. M.; Ferretti, M. T.; Lanman, L.; Chadha, A. S.; van der Flier, W. M. Global estimates on the number of persons across the Alzheimer's disease continuum. *Alzheimers Dement.* **2023**, *19* (2), 658–670.
- (8) Ferri, C. P.; Jacob, K. S. Dementia in low-income and middle-income countries: Different realities mandate tailored solutions. *PLOS Medicine* **2017**, *14* (3), No. e1002271.
- (9) Scheltens, P.; Blennow, K.; Breteler, M. M. B.; de Strooper, B.; Frisoni, G. B.; Salloway, S.; Van der Flier, W. M. Alzheimer's disease. *Lancet* **2016**, *388* (10043), S05–S17.
- (10) Pickett, E. K.; Herrmann, A. G.; McQueen, J.; Abt, K.; Dando, O.; Tulloch, J.; Jain, P.; Dunnett, S.; Sohrabi, S.; Fjeldstad, M. P.; Calkin, W.; Murison, L.; Jackson, R. J.; Tzioras, M.; Stevenson, A.; d'Orange, M.; Hooley, M.; Davies, C.; Colom-Cadena, M.; Anton-Fernandez, A.; King, D.; Oren, I.; Rose, J.; McKenzie, C.-A.; Allison, E.; Smith, C.; Hardt, O.; Henstridge, C. M.; Hardingham, G. E.; Spiers-Jones, T. L. Amyloid Beta and Tau Cooperate to Cause Reversible Behavioral and Transcriptional Deficits in a Model of Alzheimer's Disease. *Cell Reports* **2019**, *29* (11), 3592–3604.
- (11) Jack, C. R.; Bennett, D. A.; Blennow, K.; Carrillo, M. C.; Dunn, B.; Haeblerlein, S. B.; Holtzman, D. M.; Jagust, W.; Jessen, F.; Karlawish, J.; Liu, E.; Molinuevo, J. L.; Montine, T.; Phelps, C.; Rankin, K. P.; Rowe, C. C.; Scheltens, P.; Siemers, E.; Snyder, H. M.; Sperling, R.; Elliott, C.; Masliah, E.; Ryan, L.; Silverberg, N. NIA-AA Research Framework: Toward a biological definition of Alzheimer's disease. *Alzheimer's Dementia* **2018**, *14* (4), 535–562.
- (12) Alzheimer's Association. 2018 Alzheimer's disease facts and figures. *Alzheimer's Dementia* **2018**, *14* (3), 367–429.
- (13) van Dyck, C. H.; Swanson, C. J.; Aisen, P.; Bateman, R. J.; Chen, C.; Gee, M.; Kanekiyo, M.; Li, D.; Reyderman, L.; Cohen, S.; Froelich, L.; Katayama, S.; Sabbagh, M.; Vellas, B.; Watson, D.; Dhadda, S.; Irizarry, M.; Kramer, L. D.; Iwatsubo, T. Lecanemab in Early Alzheimer's Disease. *N. Engl. J. Med.* **2023**, *388* (1), 9–21.
- (14) Slough, C.; Masters, S. C.; Hurley, R. A.; Taber, K. H. Clinical Positron Emission Tomography (PET) Neuroimaging: Advantages and Limitations as a Diagnostic Tool. *J. Neuropsychiatry Clin. Neurosci.* **2016**, *28* (2), A4–71.
- (15) Morris, E.; Chalkidou, A.; Hammers, A.; Peacock, J.; Summers, J.; Keevil, S. Diagnostic accuracy of 18F amyloid PET tracers for the diagnosis of Alzheimer's disease: a systematic review and meta-analysis. *Eur. J. Nucl. Med. Mol. Imaging* **2016**, *43* (2), 374–385.
- (16) Valotassiou, V.; Malamitsi, J.; Papatriantafyllou, J.; Dardiotis, E.; Tsougos, I.; Psimadas, D.; Alexiou, S.; Hadjigeorgiou, G.; Georgoulas, P. SPECT and PET imaging in Alzheimer's disease. *Ann. Nucl. Med.* **2018**, *32* (9), 583–593.
- (17) Bao, W.; Xie, F.; Zuo, C.; Guan, Y.; Huang, Y. H. PET Neuroimaging of Alzheimer's Disease: Radiotracers and Their Utility in Clinical Research. *Front. Aging Neurosci.* **2021**, *13*, 624330.
- (18) Bollack, A.; Pemberton, H. G.; Collij, L. E.; Markiewicz, P.; Cash, D. M.; Farrar, G.; Barkhof, F. Longitudinal amyloid and tau PET imaging in Alzheimer's disease: A systematic review of methodologies and factors affecting quantification. *Alzheimer's Dementia* **2023**, *19*, 5232.
- (19) Jie, C. V. M. L.; Treyer, V.; Schibli, R.; Mu, L. Tauvid: The First FDA-Approved PET Tracer for Imaging Tau Pathology in Alzheimer's Disease. *Pharmaceuticals* **2021**, *14* (2), 110.
- (20) Liu, K.; Li, J.; Raghunathan, R.; Zhao, H.; Li, X.; Wong, S. T. C. The Progress of Label-Free Optical Imaging in Alzheimer's Disease Screening and Diagnosis. *Front. Aging Neurosci.* **2021**, *13*, 699024.
- (21) Frid, P.; Anisimov, S. V.; Popovic, N. Congo red and protein aggregation in neurodegenerative diseases. *Brain Res. Rev.* **2007**, *53* (1), 135–160.
- (22) Jung, S. J.; Park, Y. D.; Park, J. H.; Yang, S. D.; Hur, M. G.; Yu, K. H. Synthesis and evaluation of thioflavin-T analogs as potential imaging agents for amyloid plaques. *Med. Chem. Res.* **2013**, *22* (9), 4263–4268.
- (23) Nesterov, E. E.; Škoch, J.; Hyman, B. T.; Klunk, W. E.; Bacskai, B. J.; Swager, T. M. In Vivo Optical Imaging of Amyloid Aggregates in Brain: Design of Fluorescent Markers. *Angew. Chem., Int. Ed.* **2005**, *44* (34), 5452–5456.
- (24) Khurana, R.; Coleman, C.; Ionescu-Zanetti, C.; Carter, S. A.; Krishna, V.; Grover, R. K.; Roy, R.; Singh, S. Mechanism of thioflavin T binding to amyloid fibrils. *J. Struct. Biol.* **2005**, *151* (3), 229–238.
- (25) Groenning, M. Binding mode of Thioflavin T and other molecular probes in the context of amyloid fibrils—current status. *J. Chem. Biol.* **2010**, *3* (1), 1–18.

- (26) Bajad, N. G.; Kumar, A.; Singh, S. K. Recent Advances in the Development of Near-Infrared Fluorescent Probes for the in Vivo Brain Imaging of Amyloid- β Species in Alzheimer's Disease. *ACS Chem. Neurosci.* **2023**, *14* (17), 2955–2967.
- (27) Aliyan, A.; Cook, N. P.; Martí, A. A. Interrogating Amyloid Aggregates using Fluorescent Probes. *Chem. Rev.* **2019**, *119* (23), 11819–11856.
- (28) Staderini, M.; Martín, M. A.; Bolognesi, M. L.; Menéndez, J. C. Imaging of β -amyloid plaques by near infrared fluorescent tracers: a new frontier for chemical neuroscience. *Chem. Soc. Rev.* **2015**, *44* (7), 1807–1819.
- (29) Gyasi, Y. I.; Pang, Y.-P.; Li, X.-R.; Gu, J.-X.; Cheng, X.-J.; Liu, J.; Xu, T.; Liu, Y. Biological applications of near infrared fluorescence dye probes in monitoring Alzheimer's disease. *Eur. J. Med. Chem.* **2020**, *187*, 111982.
- (30) Peng, C.; Wang, X.; Li, Y.; Li, H.-W.; Wong, M. S. Versatile fluorescent probes for near-infrared imaging of amyloid- β species in Alzheimer's disease mouse model. *J. Mater. Chem. B* **2019**, *7* (12), 1986–1995.
- (31) Yang, J.; Zeng, F.; Ge, Y.; Peng, K.; Li, X.; Li, Y.; Xu, Y. Development of Near-Infrared Fluorescent Probes for Use in Alzheimer's Disease Diagnosis. *Bioconjugate Chem.* **2020**, *31* (1), 2–15.
- (32) Rai, H.; Gupta, S.; Kumar, S.; Yang, J.; Singh, S. K.; Ran, C.; Modi, G. Near-Infrared Fluorescent Probes as Imaging and Theranostic Modalities for Amyloid-Beta and Tau Aggregates in Alzheimer's Disease. *J. Med. Chem.* **2022**, *65* (13), 8550–8595.
- (33) Tang, F.; Wang, K.; Liu, X.; Zhang, X.; Zhou, W.; Mu, Z.; Zhang, T.; Shu, W.; Liu, Y.; Xiao, H. Small Molecular Fluorescent Probes for Alzheimer's Disease Associated Active Species. *Chem. Eur. J.* **2023**, *29* (35), No. e202300592.
- (34) Su, D.; Diao, W.; Li, J.; Pan, L.; Zhang, X.; Wu, X.; Mao, W. Strategic Design of Amyloid- β Species Fluorescent Probes for Alzheimer's Disease. *ACS Chem. Neurosci.* **2022**, *13* (5), 540–551.
- (35) Teppang, K. L.; Zhao, Q.; Yang, J. Development of fluorophores for the detection of oligomeric aggregates of amyloidogenic proteins found in neurodegenerative diseases. *Front. Chem.* **2023**, *11*, 1343118.
- (36) Jun, Y. W.; Cho, S. W.; Jung, J.; Huh, Y.; Kim, Y.; Kim, D.; Ahn, K. H. Frontiers in Probing Alzheimer's Disease Biomarkers with Fluorescent Small Molecules. *ACS Cent. Sci.* **2019**, *5* (2), 209–217.
- (37) Lee, D.; Kim, S. M.; Kim, H. Y.; Kim, Y. Fluorescence Chemicals To Detect Insoluble and Soluble Amyloid- β Aggregates. *ACS Chem. Neurosci.* **2019**, *10* (6), 2647–2657.
- (38) Zhang, Y.; Wang, Y.; Shi, C.; Shen, M.; Lu, F. Advances in retina imaging as potential biomarkers for early diagnosis of Alzheimer's disease. *Trans. Neurodegener.* **2021**, *10*, 6.
- (39) Yang, J.; Yang, J.; Li, Y.; Xu, Y.; Ran, C. Near-infrared Fluorescence Ocular Imaging (NIRFOI) of Alzheimer's Disease. *Mol. Imaging Biol.* **2019**, *21* (1), 35–43.
- (40) Li, B.; Zhao, M.; Zhang, F. Rational Design of Near-Infrared-II Organic Molecular Dyes for Bioimaging and Biosensing. *ACS Materials Lett.* **2020**, *2* (8), 905–917.
- (41) Li, L.; Dong, X.; Li, J.; Wei, J. A short review on NIR-II organic small molecule dyes. *Dyes Pigm.* **2020**, *183*, 108756.
- (42) Godard, A.; Kalot, G.; Pliquett, J.; Busser, B.; Le Guével, X.; Wegner, K. D.; Resch-Genger, U.; Rousselin, Y.; Coll, J.-L.; Denat, F.; Bodio, E.; Goze, C.; Sancey, L. Water-Soluble Aza-BODIPYs: Biocompatible Organic Dyes for High Contrast In Vivo NIR-II Imaging. *Bioconjugate Chem.* **2020**, *31* (4), 1088–1092.
- (43) Pan, H.; Li, S.; Kan, J.-L.; Gong, L.; Lin, C.; Liu, W.; Qi, D.; Wang, K.; Yan, X.; Jiang, J. A cruciform phthalocyanine pentad-based NIR-II photothermal agent for highly efficient tumor ablation. *Chem. Sci.* **2019**, *10* (35), 8246–8252.
- (44) Zhou, H.; Zeng, X.; Li, A.; Zhou, W.; Tang, L.; Hu, W.; Fan, Q.; Meng, X.; Deng, H.; Duan, L.; Li, Y.; Deng, Z.; Hong, X.; Xiao, Y. Upconversion NIR-II fluorophores for mitochondria-targeted cancer imaging and photothermal therapy. *Nat. Commun.* **2020**, *11*, 6183.
- (45) Shimogawa, H.; Murata, Y.; Wakamiya, A. NIR-Absorbing Dye Based on BF₂-Bridged Azafulvene Dimer as a Strong Electron-Accepting Unit. *Org. Lett.* **2018**, *20* (17), 5135–5138.
- (46) Li, H.; Wang, J.; Li, Y.; Chen, X.; Zhang, W.; Zhao, Y.; Liu, G.; Pan, J. Detection of A β oligomers in early Alzheimer's disease diagnose by in vivo NIR-II fluorescence imaging. *Sens. Actuators B Chem.* **2022**, *358*, 131481.
- (47) Miao, J.; Miao, M.; Jiang, Y.; Zhao, M.; Li, Q.; Zhang, Y.; An, Y.; Pu, K.; Miao, Q. An Activatable NIR-II Fluorescent Reporter for In Vivo Imaging of Amyloid- β Plaques. *Angew. Chem., Int. Ed.* **2023**, *62* (7), No. e202216351.
- (48) Waters, J. Sources of widefield fluorescence from the brain. *eLife* **2020**, *9*, e59841.
- (49) Hong, G.; Diao, S.; Chang, J.; Antaris, A. L.; Chen, C.; Zhang, B.; Zhao, S.; Atochin, D. N.; Huang, P. L.; Andreasson, K. I.; Kuo, C. J.; Dai, H. Through-skull fluorescence imaging of the brain in a new near-infrared window. *Nat. Photonics* **2014**, *8* (9), 723–730.
- (50) Blaikie, L.; Kay, G.; Kong Thoo Lin, P. Current and emerging therapeutic targets of alzheimer's disease for the design of multi-target directed ligands. *Med. Chem. Commun.* **2019**, *10* (12), 2052–2072.
- (51) Folch, J.; Ettcheto, M.; Petrov, D.; Abad, S.; Pedrós, I.; Marin, M.; Olloquequi, J.; Camins, A. Review of the advances in treatment for Alzheimer disease: Strategies for combating β -amyloid protein. *Neurologia* **2018**, *33* (1), 47–58.
- (52) Cummings, J.; Lee, G.; Ritter, A.; Sabbagh, M.; Zhong, K. Alzheimer's disease drug development pipeline: 2020. *Alzheimer's Dementia* **2020**, *6*, No. e12050.
- (53) Karlawish, J.; Grill, J. D. The approval of Aduhelm risks eroding public trust in Alzheimer research and the FDA. *Nat. Rev. Neurol.* **2021**, *17* (9), 523–524.
- (54) Cummings, J.; Aisen, P.; Lemere, C.; Atri, A.; Sabbagh, M.; Salloway, S. Aducanumab produced a clinically meaningful benefit in association with amyloid lowering. *Alzheimers Res. Ther.* **2021**, *13*, 98.
- (55) Moutinho, S. The long road to a cure for Alzheimer's disease is paved with failures. *Nat. Med.* **2022**, *28* (11), 2228–2231.
- (56) Mintun, M. A.; Lo, A. C.; Duggan Evans, C.; Wessels, A. M.; Ardayfio, P. A.; Andersen, S. W.; Shcherbinin, S.; Sparks, J.; Sims, J. R.; Brys, M.; Apostolova, L. G.; Salloway, S. P.; Skovronsky, D. M. Donanemab in Early Alzheimer's Disease. *N. Engl. J. Med.* **2021**, *384* (18), 1691–1704.
- (57) Chen, X. S. Introducing Theranostics Journal - From the Editor-in-Chief. *Theranostics* **2011**, *1*, 1–2.
- (58) Kelkar, S. S.; Reineke, T. M. Theranostics: Combining Imaging and Therapy. *Bioconjugate Chem.* **2011**, *22* (10), 1879–1903.
- (59) Arnold, C. Theranostics could be big business in precision oncology. *Nat. Med.* **2022**, *28* (4), 606–608.
- (60) Bolognesi, M. L.; Gandini, A.; Prati, F.; Uliassi, E. From Companion Diagnostics to Theranostics: A New Avenue for Alzheimer's Disease? *J. Med. Chem.* **2016**, *59* (17), 7759–7770.
- (61) Sarabia-Vallejo, Á.; López-Alvarado, P.; Menéndez, J. C. Small-molecule theranostics in Alzheimer's disease. *Eur. J. Med. Chem.* **2023**, *255*, 115382.
- (62) Dao, P.; Ye, F.; Liu, Y.; Du, Z. Y.; Zhang, K.; Dong, C. Z.; Meunier, B.; Chen, H. Development of Phenothiazine-Based Theranostic Compounds That Act Both as Inhibitors of β -Amyloid Aggregation and as Imaging Probes for Amyloid Plaques in Alzheimer's Disease. *ACS Chem. Neurosci.* **2017**, *8* (4), 798–806.
- (63) Tin, G.; Mohamed, T.; Gondora, N.; Beazely, M. A.; Rao, P. P. N. Tricyclic phenothiazine and phenoselenazine derivatives as potential multi-targeting agents to treat Alzheimer's disease. *Med. Chem. Commun.* **2015**, *6* (11), 1930–1941.
- (64) Taniguchi, S.; Suzuki, N.; Masuda, M.; Hisanaga, S.-i.; Iwatsubo, T.; Goedert, M.; Hasegawa, M. Inhibition of Heparin-induced Tau Filament Formation by Phenothiazines, Polyphenols, and Porphyrins*. *J. Biol. Chem.* **2005**, *280* (9), 7614–7623.
- (65) Hui, A.-L.; Chen, Y.; Zhu, S.-j.; Gan, C.-s.; Pan, J.; Zhou, A. Design and synthesis of tacrine-phenothiazine hybrids as multitarget drugs for Alzheimer's disease. *Med. Chem. Res.* **2014**, *23* (7), 3546–3557.
- (66) Gorecki, L.; Uliassi, E.; Bartolini, M.; Janockova, J.; Hrabínova, M.; Hepnarova, V.; Prchal, L.; Muckova, L.; Pejchal, J.; Karasova, J. Z.; Mezeiova, E.; Benkova, M.; Koblrova, T.; Soukup, O.; Petralla, S.; Monti, B.; Korabecny, J.; Bolognesi, M. L. Phenothiazine-Tacrine

Heterodimers: Pursuing Multitarget Directed Approach in Alzheimer's Disease. *ACS Chem. Neurosci.* **2021**, *12* (9), 1698–1715.

(67) Ohlow, M. J.; Moosmann, B. Phenothiazine: the seven lives of pharmacology's first lead structure. *Drug Discovery Today* **2011**, *16* (3), 119–131.

(68) Bulic, B.; Pickhardt, M.; Khlistunova, I.; Biernat, J.; Mandelkow, E.-M.; Mandelkow, E.; Waldmann, H. Rhodanine-Based Tau Aggregation Inhibitors in Cell Models of Tauopathy. *Angew. Chem., Int. Ed.* **2007**, *46* (48), 9215–9219.

(69) Gandini, A.; Bartolini, M.; Tedesco, D.; Martinez-Gonzalez, L.; Roca, C.; Campillo, N. E.; et al. Tau-Centric Multitarget Approach for Alzheimer's Disease: Development of First-in-Class Dual Glycogen Synthase Kinase 3beta and Tau-Aggregation Inhibitors. *J. Med. Chem.* **2018**, *61* (17), 7640–7656.

(70) Ono, M.; Hayashi, S.; Matsumura, K.; Kimura, H.; Okamoto, Y.; Ihara, M.; Takahashi, R.; Mori, H.; Saji, H. Rhodanine and Thiohydantoin Derivatives for Detecting Tau Pathology in Alzheimer's Brains. *ACS Chem. Neurosci.* **2011**, *2* (5), 269–275.

(71) Mendgen, T.; Steuer, C.; Klein, C. D. Privileged Scaffolds or Promiscuous Binders: A Comparative Study on Rhodanines and Related Heterocycles in Medicinal Chemistry. *J. Med. Chem.* **2012**, *55* (2), 743–753.

(72) Dao, P.; Ye, F.; Du, Z. Y.; Chen, Q.; Zhang, K.; Dong, C. Z.; Meunier, B.; Chen, H. Design and synthesis of new theranostic agents for near-infrared imaging of β -amyloid plaques and inhibition of β -amyloid aggregation in Alzheimer's disease. *Dyes Pigm.* **2017**, *147*, 130–140.

(73) Li, Y.; Cai, J.; Yan, L.; Zhang, W.; Li, L.; Du, Z.; Fang, Y.; Dong, C.; Meunier, B.; Chen, H. Phenothiazine-based theranostic compounds for in vivo near-infrared fluorescence imaging of β -amyloid plaques and inhibition of A β aggregation. *Dyes Pigm.* **2019**, *171*, 107744.

(74) Li, Y.; Yan, L.; Cai, J.; Zhang, W.; Li, L.; Du, Z.; Dong, C.; Meunier, B.; Chen, H. Development of novel theranostic agents for in vivo amyloid imaging and protective effects on human neuroblastoma cells. *Eur. J. Med. Chem.* **2019**, *181*, 111585.

(75) Yang, W.; Wong, Y.; Ng, O. T. W.; Bai, L.-P.; Kwong, D. W. J.; Ke, Y.; Jiang, Z.-H.; Li, H.-W.; Yung, K. K. L.; Wong, M. S. Inhibition of Beta-Amyloid Peptide Aggregation by Multifunctional Carbazole-Based Fluorophores. *Angew. Chem., Int. Ed.* **2012**, *51* (8), 1804–1810.

(76) Feng, X. J.; Wu, P. L.; Bolze, F.; Leung, H. W. C.; Li, K. F.; Mak, N. K.; Kwong, D. W. J.; Nicoud, J.-F.; Cheah, K. W.; Wong, M. S. Cyanines as New Fluorescent Probes for DNA Detection and Two-Photon Excited Bioimaging. *Org. Lett.* **2010**, *12* (10), 2194–2197.

(77) Li, Y.; Xu, D.; Ho, S.-L.; Li, H.-W.; Yang, R.; Wong, M. S. A theranostic agent for in vivo near-infrared imaging of β -amyloid species and inhibition of β -amyloid aggregation. *Biomaterials* **2016**, *94*, 84–92.

(78) Tolar, M.; Hey, J.; Power, A.; Abushakra, S. Neurotoxic Soluble Amyloid Oligomers Drive Alzheimer's Pathogenesis and Represent a Clinically Validated Target for Slowing Disease Progression. *Int. J. Mol. Sci.* **2021**, *22* (12), 6355.

(79) Li, Y.; Xu, D.; Sun, A.; Ho, S.-L.; Poon, C.-Y.; Chan, H.-N.; Ng, O. T. W.; Yung, K. K. L.; Yan, H.; Li, H.-W.; Wong, M. S. Fluoro-substituted cyanine for reliable in vivo labelling of amyloid- β oligomers and neuroprotection against amyloid- β induced toxicity. *Chem. Sci.* **2017**, *8* (12), 8279–8284.

(80) Iyaswamy, A.; Wang, X.; Krishnamoorthi, S.; Kaliamoorthy, V.; Sreenivasamurthy, S. G.; Kumar Durairajan, S. S.; Song, J.-X.; Tong, B. C.-k.; Zhu, Z.; Su, C.-F.; Liu, J.; Cheung, K.-H.; Lu, J.-H.; Tan, J.-Q.; Li, H. W.; Wong, M. S.; Li, M. Theranostic F-SLOH mitigates Alzheimer's disease pathology involving TFEB and ameliorates cognitive functions in Alzheimer's disease models. *Redox Biol.* **2022**, *51*, 102280.

(81) Gillis, E. P.; Eastman, K. J.; Hill, M. D.; Donnelly, D. J.; Meanwell, N. A. Applications of Fluorine in Medicinal Chemistry. *J. Med. Chem.* **2015**, *58* (21), 8315–8359.

(82) Li, Y.; Chen, C.; Xu, D.; Poon, C.-Y.; Ho, S.-L.; Zheng, R.; Liu, Q.; Song, G.; Li, H.-W.; Wong, M. S. Effective Theranostic Cyanine for Imaging of Amyloid Species in Vivo and Cognitive Improvements in Mouse Model. *ACS Omega* **2018**, *3* (6), 6812–6819.

(83) Wang, X.; Wang, C.; Chan, H.-N.; Ashok, I.; Krishnamoorthi, S. K.; Li, M.; Li, H.-W.; Wong, M. S. Amyloid- β oligomer targeted theranostic probes for in vivo NIR imaging and inhibition of self-aggregation and amyloid- β induced ROS generation. *Talanta* **2021**, *224*, 121830.

(84) Chen, C.; Wang, X.; Xu, D.; Zhang, H.; Chan, H.-N.; Zhan, Z.; Jia, S.; Song, Q.; Song, G.; Li, H.-W.; Wong, M. S. Multifunctional theranostic carbazole-based cyanine for real-time imaging of amyloid- β and therapeutic treatment of multiple pathologies in Alzheimer's disease. *J. Mater. Chem. B* **2023**, *11* (22), 4865–4873.

(85) Na, H. B.; Song, I. C.; Hyeon, T. Inorganic Nanoparticles for MRI Contrast Agents. *Adv. Mater.* **2009**, *21* (21), 2133–2148.

(86) Rogosnitzky, M.; Branch, S. Gadolinium-based contrast agent toxicity: a review of known and proposed mechanisms. *BioMetals* **2016**, *29* (3), 365–376.

(87) Martins, A. F.; Oliveira, A. C.; Morfin, J.-F.; Laurents, D. V.; Tóth, É.; Geraldès, C. F. G. C. Associating a negatively charged GdDOTA-derivative to the Pittsburgh compound B for targeting A β amyloid aggregates. *J. Biol. Inorg. Chem.* **2016**, *21* (1), 83–99.

(88) Wang, X.; Chan, H. N.; Desbois, N.; Gros, C. P.; Bolze, F.; Li, Y.; Li, H. W.; Wong, M. S. Multimodal Theranostic Cyanine-Conjugated Gadolinium(III) Complex for In Vivo Imaging of Amyloid- β in an Alzheimer's Disease Mouse Model. *ACS Appl. Mater. Interfaces* **2021**, *13* (16), 18525–18532.

(89) Tomizawa, I.; Nakagawa, H.; Sohma, Y.; Kanai, M.; Hori, Y.; Tomita, T. Photo-Oxygenation as a New Therapeutic Strategy for Neurodegenerative Proteinopathies by Enhancing the Clearance of Amyloid Proteins. *Front. Aging Neurosci.* **2022**, *14*, 945017.

(90) Wang, T.; Zhang, L.; Wang, J.; Feng, Y.; Xu, E.; Mao, X.; Liu, L. Evaluation of the photo-degradation of Alzheimer's amyloid fibrils with a label-free approach. *Chem. Commun.* **2018**, *54* (93), 13084–13087.

(91) Bondia, P.; Torra, J.; Tone, C. M.; Sawazaki, T.; del Valle, A.; Sot, B.; Nonell, S.; Kanai, M.; Sohma, Y.; Floris, C. Nanoscale View of Amyloid Photodynamic Damage. *J. Am. Chem. Soc.* **2020**, *142* (2), 922–930.

(92) Yang, J.; Wang, X.; Liu, J.; Chi, W.; Zhang, L.; Xiao, L.; Yan, J.-w. Near-Infrared Photooxygenation Theranostics Used for the Specific Mapping and Modulating of Amyloid- β Aggregation. *Anal. Chem.* **2022**, *94* (45), 15902–15907.

(93) Amdursky, N.; Erez, Y.; Huppert, D. Molecular Rotors: What Lies Behind the High Sensitivity of the Thioflavin-T Fluorescent Marker. *Acc. Chem. Res.* **2012**, *45* (9), 1548–1557.

(94) Rodríguez-Rodríguez, C.; Rimola, A.; Rodríguez-Santiago, L.; Ugliengo, P.; Alvarez-Larena, A.; Gutiérrez-de-Terán, H.; Sodupe, M.; González-Duarte, P. Crystal structure of thioflavin-T and its binding to amyloid fibrils: insights at the molecular level. *Chem. Commun.* **2010**, *46* (7), 1156–1158.

(95) Fu, W.; Yan, C.; Guo, Z.; Zhang, J.; Zhang, H.; Tian, H.; Zhu, W.-H. Rational Design of Near-Infrared Aggregation-Induced-Emission-Active Probes: In Situ Mapping of Amyloid- β Plaques with Ultra-sensitivity and High-Fidelity. *J. Am. Chem. Soc.* **2019**, *141* (7), 3171–3177.

(96) Nunes da Silva, R.; Costa, C. C.; Santos, M. J. G.; Alves, M. Q.; Braga, S. S.; Vieira, S. I.; Rocha, J.; Silva, A. M. S.; Guieu, S. Fluorescent Light-up Probe for the Detection of Protein Aggregates. *Chem. Asian J.* **2019**, *14* (6), 859–863.

(97) Sato, T.; Hotsumi, M.; Makabe, K.; Konno, H. Design, synthesis and evaluation of curcumin-based fluorescent probes to detect A β fibrils. *Bioorg. Med. Chem. Lett.* **2018**, *28* (22), 3520–3525.

(98) Yang, Y.; Li, S.; Zhang, Q.; Kuang, Y.; Qin, A.; Gao, M.; Li, F.; Tang, B. Z. An AIE-active theranostic probe for light-up detection of A β aggregates and protection of neuronal cells. *J. Mater. Chem. B* **2019**, *7* (15), 2434–2441.

(99) Li, H.; Wang, J.; Zhang, W.; Xia, Z.; Zhai, N.; Liu, G.; Wang, K.; Pan, J. Functional bioprobe for responsive imaging and inhibition of amyloid- β oligomer based on curcuminoid scaffold. *J. Lumin.* **2021**, *238*, 118218.

(100) Sun, L.; Cho, H.-J.; Sen, S.; Arango, A. S.; Huynh, T. T.; Huang, Y.; Bandara, N.; Rogers, B. E.; Tajkhorshid, E.; Mirica, L. M.

Amphiphilic Distyrylbenzene Derivatives as Potential Therapeutic and Imaging Agents for Soluble and Insoluble Amyloid β Aggregates in Alzheimer's Disease. *J. Am. Chem. Soc.* **2021**, *143* (27), 10462–10476.

(101) Sun, X.-y.; Liu, T.; Sun, J.; Wang, X.-j. Synthesis and application of coumarin fluorescence probes. *RSC Adv.* **2020**, *10* (18), 10826–10847.

(102) Chen, X.; Li, Y.; Kang, J.; Ye, T.; Yang, Z.; Liu, Z.; Liu, Q.; Zhao, Y.; Liu, G.; Pan, J. Application of a novel coumarin-derivative near-infrared fluorescence probe to amyloid- β imaging and inhibition in Alzheimer's disease. *J. Lumin.* **2023**, *256*, 119661.

(103) Zhang, T.; Chen, X.; Yuan, C.; Pang, X.; Shangguan, P.; Liu, Y.; Han, L.; Sun, J.; Lam, J. W. Y.; Liu, Y.; Wang, J.; Shi, B.; Zhong Tang, B. Near-Infrared Aggregation-Induced Emission Luminogens for In Vivo Theranostics of Alzheimer's Disease. *Angew. Chem., Int. Ed.* **2023**, *62* (2), No. e202211550.